DYNAMIC PROCESSES IN COMPLEX POLYMERIC SYSTEMS

by

Hengxi Yang

A dissertation submitted in partial fulfillment
of the requirements for the degree of
Doctor of Philosophy
(Physics)
in the University of Michigan
2014

Doctoral Committee:

Professor Peter F. Green, Co-Chair
Associate Professor Robert Deegan, Co-Chair
Professor Cagliyan Kurdak
Professor Leonard M. Sander
Assistant Professor Anish Tuteja

To my parents and grandparents

ACKNOWLEDGMENTS

I owe my thank-you to many people throughout my many years of study in graduate school. By no means could I have completed my study, research and this dissertation without their selfless support and generous help.

First of all, I would like to give my sincere gratitude to my advisor, Professor Peter F. Green. As a physics student fascinated by the beauty and mystery of polymer science but with merely any knowledge or training in the field, Professor Green led me into the polymer world with his kind and warm support, encouragement and endless patience. Throughout my Ph.D. years, I am always given the freedom to pursue the science I am interested in, and at the same time, always feel comfortable to simply walk into his office asking for guidance and support. Professor Green also creates a group environment in which every group member feels motivated, encouraged and supported, and treats one another like family.

I would also like to thank Professor Cagliyan Kurdak for his kind support when I decided to do research outside the Department of Physics. When I felt confused and worried about the preliminary exam, his words and smile calmed me down and he kindly helped me set up the entire committee and volunteered to be one of the committee members. My appreciation also goes to Professor Robert Deegan and Professor Leonard M. Sander for their support being my committee member and their precious time spent getting to know my research. I should also thank Professor Anish Tuteja for his excellent teaching of the course *Polymer Physics* that truly was of great help to my research.

Among all my colleagues within the Green Group, former and current, I especially thank Dr. Hyunjoon Oh, who trained and taught me every single thing he knew and learned about polymer physics, especially about the technique of broadband dielectric spectroscopy (BDS), with incredible patience and attention to details. Being a student with a ton of

questions, he never turned me away even when he had his own business and two kids to take care of; whenever I needed a favor, he was always available to help like a big brother.

I must also thank my colleagues, Dr. Emmanouil Glynos and Dr. Carl McIntyre, for their generous help on all sorts of problems I encountered in polymer science and their patience towards all my silly questions. I also thank Dr. Chelsea Chen and Dr. Jenny Kim for their help with the experiments and discussion, and all the warm encouragement when I panicked before my conference presentations.

I would like to send my gratefulness to the rest of the Green Group members, including Bradley Frieberg, Bingyuan Huang, Jojo Amonoo, Peter Chung, Junnan Zhao, Anton Li, Dr. Aaron Tan, Kyle Johnson and Ban Dong. They are the reason why every day in the lab has been enjoyable and memorable, in spite of the bad samples and frustrating results. I also thank the former group member and undergraduate student Ga Ram Jun, who was always there to lend a hand and never complained about the tedious lab work.

Apart from the faculty and colleagues at the University of Michigan, I also thank Professor Anatoli Serghei (Université Claude Bernard Lyon 1) for the helpful discussion about the measurement and analysis using BDS, and thank Professor J. Ross Macdonald (emeritus, University of North Carolina) for the advice on the impedance spectroscopy data fitting using the software LEVM.

I would also like to thank the staff members of the Department of Materials Science and Engineering, especially Keith McIntyre, Lisa Moran, Shelley Fellers, Jeanette Johnson and Georgia Knope; they never said no to me whenever I had a technical or administrative request, even when it was not their responsibility. I also thank Christina Zigulis, the graduate coordinator of the Department of Physics, for her administrative guidance and support over the years.

Finally, I would like to express my deepest gratitude to my parents, Weihong Yang and Ping Liu, as well as my grandparents, Yanbing Liu and Zhengsheng Liu, for their forever love and understanding. It has been a great amount of power and strength for me knowing that they would always be caring and supportive, unconditionally, on the other side of the globe but simply a phone call or an email away. This dissertation is thereby dedicated to them with my wholehearted gratefulness. 感謝你們!

TABLE OF CONTENTS

LIST OF FIGURES

LIST OF TABLES

LIST OF APPENDICES

ABSTRACT

In general, the physical properties of polymers intimately depend on the morphology. In this dissertation we investigated the role of morphology on dynamic processes that occur in complex systems possessing appreciably different morphologies: (1) diblock copolymer/homopolymer blends; (2) miscible blends of linear chain polymers; (3) semicrystalline polymer.

(i) A-*b*-B diblock copolymer chains form micelles of A-type coronas and B-type cores, in an A-type host. We investigated the segmental dynamics of polyisoprene (PI) chains in polystyrene-*b*-polyisoprene (PS-*b*-PI) melt as well as PS-*b*-PI/polystyrene (PS) blends. PS-*b*-PI forms micellar structures of varying geometries within PS hosts of different molecular weight. The glass transition temperatures and dynamics of PI were more strongly influenced by the local geometry than by the dimensions of confinement. The behavior is rationalized in terms of the notion of free volume.

(ii) The segmental dynamics of poly(vinyl methyl ether) (PVME) chains in miscible blends of PVME/PS were investigated. These blends are known to be locally compositional heterogeneous. We showed, for the first time, the temperature dependence of the heterogeneity by measuring their dynamics: the PS and PVME chains are mixed more homogeneously at high temperatures, whereas at low temperatures the behavior is indicative of PVME chains relaxing in two distinctly local compositions.

(iii) The effect of morphology of a hole-conducting semicrystalline polymer was studied. We showed that the out-of-plane hole transport in conjugated polymer films, poly(3-hexylthiophene) (P3HT), is very sensitive to the morphology of the polymer. Impedance spectroscopy conducted the measurement, which simultaneously extracted the dc conductivity, mobility and carrier density. The out-of-plane carrier mobility of P3HT

increases with increasing thickness from 100 nm to ~700 nm, meanwhile the dc conductivity and the carrier density decrease dramatically with thickness in the same range. Such dramatic trends are due to the substrate induced orientation of the crystalline domains in P3HT; unlike the inorganic scenarios, in conjugated polymers the carrier mobility and density are no longer intrinsic properties and can be strongly influenced by the surrounding environment.

The studies of these systems provide new insights into the role of morphology on diverse dynamic processes that occur in polymers.

CHAPTER 1
INTRODUCTION AND BACKGROUND

1.1 Overview

1.1.1 Polymer physics: achievements and challenges

Although many polymeric materials, such as wool, silk and natural rubber, have been used by the human beings over hundreds of years, they were not much considered as scientific subjects until the early twentieth century. In 1920, Staudinger carried out the "macromolecular hypothesis" [1]; at that time, organic chemists were still enjoying their success in determining the structures of ordinary-sized molecules, while physicist, on the other hand, were fascinated by their incredible atomic and electronic findings within a molecule. It was not until a decade later before polymer science, both synthesis and fundamental theory, began to develop rapidly. In less than a century, human beings can no longer live in a world without synthetic polymer, such as all types of plastics, adhesives and synthetic oils.

The foundation of polymer physics was gradually established following the synthesis development of macromolecules, pioneered by Kuhn, Flory, Huggins, Stockmayer, Zimm, Rouse, et al. Later, by the 1980s, the main principles of modern polymer physics were developed, with the work of Edwards, de Gennes, and others [2]. Given the fact that Staudinger's macromolecular hypothesis was not even widely accepted until 1930s, it is no doubt that polymer science has made remarkable progress over the past century.

In spite of the great success of polymer science, including polymer physics, over the past 100 years, the understanding of polymer physics is still on a rather basic and

fundamental level, especially when it is compared to the achievements and knowledge in the physics of inorganics.

Compared to the inorganics, polymer systems involve much richer and more complicated interactions, due to the abundance of the chemical structures. Every different polymer has its own unique set of chemical and physical properties; understanding the profound and often subtle properties across many different polymers is difficult.

The complexity of ordered and disordered morphologies also play a significant role in understanding the polymer systems. For many complex polymeric systems such as films, blends, copolymers, nanocomposites, semicrystalline polymers and polymeric devices, which have shown promising properties and potentials in industrial applications over the recent decades, due to the lack of long-range ordering in the systems, the structures and interactions between polymer chains are complicated and require very expensive simulation studies; in some situations, these simulations have unavoidable limits and can be inconclusive.

Moreover, there are often greater limitations of characterization techniques for polymeric materials. Partly due to the nature of disorder in polymeric systems, the characterization techniques in polymer science are still mostly macroscopic, such as differential scanning calorimetry (DSC), rheology, dynamic mechanical analysis (DMA), etc. Many spectroscopic measurements, e.g. X-ray diffraction (XRD), neutron scattering, often have much lower intensity due to the disorder and suffer from much complicated analysis compared to the inorganics. Local measurements, on the other hand, including atomic force microscopy (AFM) and transmission electron microscopy (TEM), usually experience greater limitations compared to measuring hard, inorganic materials, which still call for further development.

Finally, the mysteries of certain fundamental concepts remain to be the holy grail of polymer physics. In spite of the development of many important and useful theories in the past decades, certain debates remain over basic concepts in polymer physics, such as the glass transition temperature (T_g), the dynamic relaxations of polymer chains and their temperature dependence. Many of these concepts were introduced initially from industry as macroscopic properties, whose definitions, characterizations or relation with local properties are not clear on the nanoscale.

Many questions remain unanswered in polymer physics. Some of the questions are more fundamental, such as the relationship between the T_g values measured by different techniques, between the dynamic T_g (measured by monitoring the dynamics of the polymer chains) and the calorimetric T_g (measured by locating the temperature at which the heat capacity shifts), or between the dynamic T_gs measured mechanically (e.g. rheology and dynamic mechanical analysis (DMA)) or electrically (e.g. broadband dielectric spectroscopy (BDS)) [3]. On the other hand, some other problems are associated with polymer chains in more complex systems, for instance, how the chain dynamics may be affected under confinement or by controlling the local microscopic environment around polymer chains. In addition, the linking between the macroscopic properties and microscopic observables as well as physical quantities is yet to be fully established.

1.1.2 Introduction of this work

One of the most important topics in science is the structure/property relationship. It is emphasized in both scientific research and industrial development, because such a relationship helps one predict the properties of a polymer system from certain structure, as well as deduce the structure of a polymer system from measurable macroscopic properties. Among all properties that are measured and understood, e.g. mechanical, electrical, thermal, optical, dynamic, etc., the dynamic properties are one of the most fundamental and microscopic and most closely related to the corresponding structure. Therefore, it is vital to investigate the dynamics of polymers in polymer physics.

In this study, we are particularly interested in understanding how local, nanoscopic environmental variations may affect the dynamics of the polymer chains, as well as the T_g of the local polymer domains. This is especially important in many complex systems with great industrial potentials, since local chain dynamics and morphologies, without even changing the chemical structures or composition of the components in the polymer systems, can be a critical factor responsible for the more macroscopic mechanical, electrical and optical properties (Chapter 2). New phenomena discovered in various complex systems regarding local effects and behaviors on chain dynamics and T_gs also contribute to our knowledge on nanoscopic interactions between polymers and local compositions and morphologies (Chapter 3), which would eventually help disclose the more fundamental mechanism of polymer dynamics on the nanoscale.

Measuring the dynamics of polymers can be challenging. In our work, we capture the dynamic properties of polymer chains using the technique of broadband dielectric spectroscopy (BDS) (see Section 1.3.1 for detailed information). The technique measures relaxations of polymer chains, segments and functional groups through monitoring the energy loss of polymer chains under ac voltage with controlled frequency. In an amorphous system, the intensity of the energy loss is proportional to the dipole moment of the monomer, so nonpolar or very weakly polar monomers are essentially invisible to BDS. This phenomenon is important since BDS may then be used to selectively measure a small category of polymers among complex polymer systems. Such an idea was applied to understand polymer chains in confined geometries (Chapter 2) and miscible blends (Chapter 3).

Apart from the dynamics, charge transport properties may also be examined to understand morphologies in polymeric systems. The technique of BDS measures the complex impedances of materials under ac frequency; when the material is somewhat electrically conducting, the technique, now known as impedance spectroscopy (IS), can be used to measure transport properties. Popular in electrochemistry in understanding reactions in complex solutions, IS is sensitive to all sorts of movements of charges, therefore it is an ideal tool for charge transport characterization. For the last part of our work (Chapter 4), we are able to apply the technique to measuring dc conductivity, mobility and charge carrier density of the out-of-plane thin films of poly(3-hexylthiophene) (P3HT), a benchmark organic semiconducting material that has shown promising application in organic solar cells. The out-of-plane charge transport properties of P3HT films provide information about the substrate induced orientation of the crystallized domains in the films.

Before we move on to the individual projects, in the next section (Section 1.2), some general background information regarding the polymer systems studied in this work is provided, including the diblock copolymer melt and copolymer/homopolymer blend (Section 1.2.1 and Chapter 2), miscible polymer/polymer blend (Section 1.2.2 and Chapter 3) and conjugated polymer thin film and organic solar cells (Section 1.2.3 and Chapter 4). The scope of work is also briefly discussed for each project.

In Section 1.3, the major techniques used in this work are discussed. Broadband dielectric spectroscopy (BDS) is explained in details (Section 1.3.1) while other techniques, i.e. differential scanning calorimetry (DSC), spectroscopic ellipsometry, dynamics secondary

ion mass spectroscopy (DSIMS), atomic force microscopy (AFM) and scanning transmission electron microscopy (STEM), used for the characterization of T_g and morphologies are also mentioned (Section 1.3.2).

1.2 The polymer systems discussed in this work

1.2.1 Diblock copolymer melt and copolymer/homopolymer blend

When the ends of two polymer chains are joined together, the two chains form a block copolymer, with each polymer chain known as a block. It is called "diblock copolymer" when the molecule contains two chains (blocks) combined together. These two polymers tend not to mix (due to their rather low entropy of mixing) when they are free chains, but in block copolymers they are forced to bond together within a molecule. However, in order to minimize the free energy, the block copolymer melt self-organizes into remarkable nanoscale structures, depending on the degree of polymerization ratio between the two blocks. Such a phenomenon offers the option to combine the properties of two distinct polymers together to generate new behaviors. For example, when a rubbery block is combined with a plastic block to form a block copolymer, the copolymer melt may possess both plastic and elastic properties; this material is known as thermoplastic elastomer.

Apart from the broad industrial application of block copolymers due to their ability of combining different physical properties of distinct polymers, block copolymers have shown great potential in nanotechnological applications, as they form nanoscopic phase-separated structures that may be easily tailored by controlling the molecules of the block copolymers. Diblock copolymer melt is the most studied copolymer system, whose structures with respect to different molecular ratio of the two blocks are shown in Figure 1.1 [4]. Specifically, when the two blocks are similar in length, the copolymer melt forms a lamellar structure under equilibrium; with increasing the volume percentage of one of the blocks, the structure of the melt evolves from lamellar to bicontiuous, cylindrical and spherical, respectively, to maintain the minimum overall free energy.

Furthermore, when diblock copolymer A-*b*-B is dissolved in a selective solvent (good solvent for one of the blocks but precipitant for the other), local aggregates of A-*b*-B known as micelles would form when the concentration of the copolymer is greater than a threshold (i.e. the critical micelle concentration, or cmc) [5]. The basic picture stays true when A-*b*-B is

mixed with homopolymer A instead, rather than small molecule solvents, with polymer A being the majority component. However, in such a blend of copolymer A-*b*-B and homopolymer A host, depending on the relative chain lengths of the A-block in A-*b*-B and the host, the entropic interactions between the copolymer and host play a vital role in determining the micellar structure in the blend [6-8]. Our group has also shown that, in thin films, the micelle size changes systematically as a function of the degree of polymerization of the homopolymer host [9]. Some more detailed discussion can be found in Chapter 2.

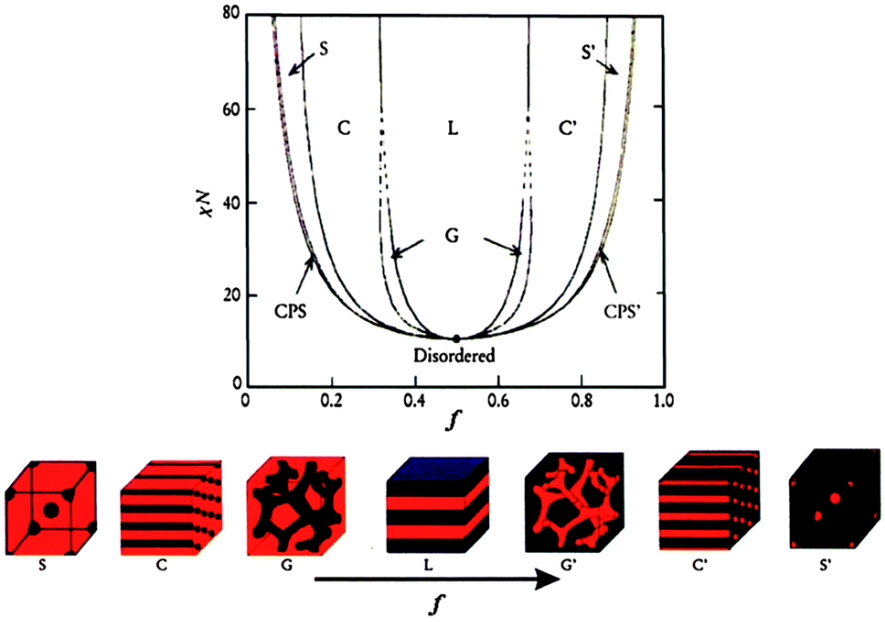

Figure 1.1 Typical phase diagram of a diblock copolymer A-*b*-B, taken from [4] with permission, where *f* denotes the volume ratio between blocks A and B. χ and *N* are the Flory-Huggins parameter and the degree of polymerization of A-*b*-B, respectively. *L* = lamellae, G and G' = bicontinuous gyroids, C and C' = hexagonally packed cylinders, S and S' = body-centered-cubic spheres.

In our work shown in Chapter 2, we utilized the rich nanostructures in the blends of polystyrene-*b*-polyisoprene (PS-*b*-PI) and homopolymer polystyrene (PS) and studied the segmental dynamics of polyisoprene (PI)-block confined in and tethered to the rigid PS/PI interfaces with different geometries.

1.2.2 Heterogeneous polymer/polymer blend

Unlike small molecules, the entropy of mixing in a binary polymer/polymer blend is comparably small due to their large molecules. This implies that it is very common for two polymers to be immiscible. However, there are certain pairs of polymers that do appear miscible, in a certain range of temperatures and compositions, usually due to their similar chemical structures and attractive interactions (including hydrogen bonding) between the monomers. In miscible polymer blends, the polymer chains of different components mix on the nanoscopic level.

One major and useful criterion for miscible polymer blends is that, while the components in the blend possess their own distinct dynamics and T_g in their pure melts, they share the same dynamics and T_g in the miscible blend, suggesting that all polymer chains experience the same environment in the blend. In contrast, for a system in which the chains do not mix on the nanoscale, multiple T_gs are observed; a typical example would be a diblock copolymer melt, in which the two blocks form their own local domains. Miscible polymer blends fit this criterion: a single T_g is always observed, using either spectroscopic or calorimetric techniques.

However, for the past decades, multiple experiments suggest that certain miscible blends are very different from molecularly homogeneous melts [10]. All the characterization techniques, such as differential scanning calorimetry (DSC), nuclear magnetic resonance (NMR) spectroscopy, small angle neutron scattering (SANS) and broadband dielectric spectroscopy (BDS) show a very broad signal regarding the system T_g (e.g. ref [11-13]). Moreover, tracer diffusion measurements [14-15] discovered that different components in the blend have different diffusion coefficients, which implies that they experience different local environments.

Two families of theories, the self-concentration theories and the concentration fluctuation theories [10], have been established in the past two decades. Unfortunately, due to the lack of contrast in very local (nanometers in length) regions and the fact that the polymer chains are not phase separated, very little experimental evidence has been obtained.

In our work (Chapter 3), we discuss the morphology of the blends of polystyrene (PS) and poly(vinyl methyl ether) (PVME) on the nanometer scale, through measurements of the local segmental dynamics of the polymer chains; this provided further evidence on the nature of heterogeneity in polymer/polymer blends.

1.2.3 Conjugated polymer film and organic solar cells

Organic semiconducting polymers, over the past decade, have shown significant potential in the research and industry of organic photovoltaics (OPVs). Compared to the inorganic photovoltaics, OPVs are superior over the inorganic counterpart in terms of their flexibility (soft-materials), low manufacturing cost (solvent-based casting at ambient pressure) and potentially cheap materials (abundance of common organic elements compared to limited resources of expensive elements in nature). However, the development of OPV devices also suffers from severe obstacles: (1) the lack of long-range ordering in polymers results in the low carrier mobility, usually orders of magnitude lower than that of the inorganic counterparts; (2) the electron-hole pairs (excitons) generated by light do not dissociate immediately as in inorganic materials, which requires much more sophisticated device structures (e.g. bulk heterojunction (BHJ)); (3) in BHJ devices, the complicated nature of the p-type conjugated polymer and the mixture with corresponding n-type material is very sensitive to the processing procedure.

Here, we are interested in a most commonly studied conjugated polymer, the regioregular poly(3-hexylthiophene) (P3HT) [16], a semicrystalline polymer with a low T_g. Although there are plenty of articles studying its properties and performance over the years, its morphology and performance at various processing conditions are far from being fully understood. Furthermore, more knowledge on the morphologies and their relationship with the performance of P3HT-contained OPV systems would considerably help with the understanding of the mechanism of OPVs, such as optimizing the processing condition as well as the effect of crystallization on device performance As materials scientists, we are particularly interested in understanding the charge transport properties in P3HT and their relationship with its morphology; this may help answer the question of how high-performance device should be prepared.

In our work (Chapter 4), we focused on the charge carrier transport properties in the out-of-plane direction, using impedance spectroscopy (IS). The thickness dependence of these properties has been studied. With the help of conductive atomic force microscopy (AFM), we exhibited the different P3HT morphologies and their effect on the transport properties.

1.3 The techniques

1.3.1 Broadband dielectric spectroscopy (BDS)

BDS is one of the most powerful and versatile techniques to measure the dynamics of polymers, bulk or thin film. The fundamental physical concepts and setup may date back to the 1940s, but it was not applied to the study of polymer dynamics until the 1980s. Since then, BDS has been proven to be one of the most important characterization methods in the dynamic study of polymer science, and has been creatively applied to local and nanoscale measurements in recent years.

For the details of the technique of BDS, one may refer to the book *Broadband Dielectric Spectroscopy* by Kremer and Schönhals [17] (on measuring polymeric systems), as well as *Impedance Spectroscopy: Theory, Experiment, and Applications* by Barsoukov and Macdonald [18] (with a much broader background). Additionally, Novocontrol Technologies, GmbH also provides a few theoretical and technical notes regarding the fundamentals and the application of the technique [19]. Here, only the most critical concepts of the technique are discussed.

1.3.1.1 The fundamentals

When measuring polymers, due to their very low conductivity, it is the complex permittivity, ε^*, that is measured across the material. This complex permittivity is a function of frequency, i.e. $\varepsilon^* = \varepsilon^*(\omega)$; depending on the frequency range, the frequency dependence comes from different mechanisms, from high frequency to low frequency being electronic, atomic, orientational (dipolar) and interfacial (ionic) polarization. A schematic diagram is shown in Figure 1.2. The first two polarizations happen at very high frequencies, which are not our interest. The ionic polarization, occurring at the lowest frequencies, is related to the geometries of the interfaces of the domains in the sample, where space charge effect takes place, causing macroscopic dipoles. The orientational polarization is responsible for the alignment of dipolar molecules under external electric field; this is the signal we are interested in, reflecting the dynamics of the polymer chains. Common frequency range for BDS is between 0.1 Hz and 1 MHz.

The complex permittivity is plotted in two separate quantities, the real part, ε', and the imaginary part, ε'', with $\varepsilon^*(\omega) = \varepsilon'(\omega) - i\varepsilon''(\omega)$ (note the *minus* sign). Here, ε' represents the energy storage and ε'' represents the energy loss, analogous to the Young's modulus in

mechanical characterizations. When the frequency of the external ac frequency matches the intrinsic frequency (i.e. the reciprocal of the relaxation time) of the polymer chains, a maximum occurs in the energy loss spectrum, $\varepsilon''(\omega)$; correspondingly, $\varepsilon'(\omega)$ undergoes a step-like change at the same frequency. An ideal case may be derived analytically; $\varepsilon^*(\omega)$ in this case is known as the Debye relaxation:

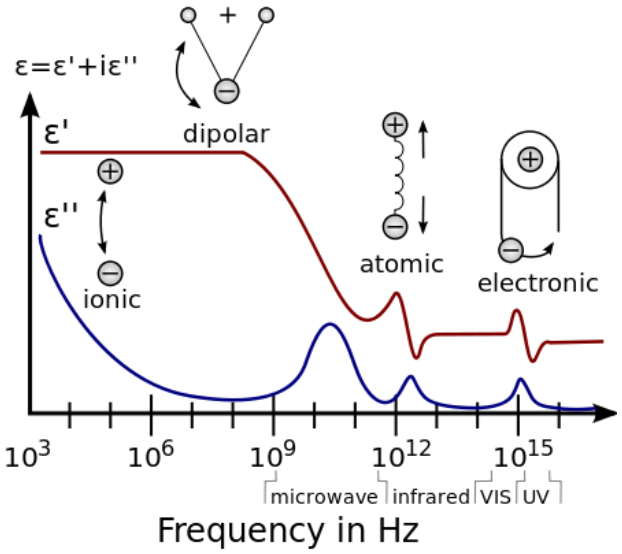

Figure 1.2 Schematic diagram of the complex permittivity spectrum vs. frequency, showing the several levels of processes. Image reprinted from Wikipedia.

$$\varepsilon^*(\omega) = \varepsilon_\infty + \frac{\varepsilon_S - \varepsilon_\infty}{1 + i\omega\tau} = \varepsilon_\infty + \frac{\Delta\varepsilon}{1 + i\omega\tau}$$

where ε_∞ and ε_S stand for the permittivity at high frequency limit and the static permittivity, respectively, with $\Delta\varepsilon$ the relaxation intensity, ω the angular frequency and τ the relaxation time. Most relaxations measured in actual materials, however, exhibit a more complex relaxation and may not be fitted using the Debye equation. To be specific, relaxations are often measured to be broadened and, unlike the symmetric Debye relaxation, appear somewhat asymmetric. These profiles cannot be reconciled theoretically, and are usually analyzed by empirical equations, such as the so-called Havriliak-Negami (HN) equation:

$$\varepsilon^*(\omega) = \varepsilon_\infty + \frac{\Delta\varepsilon}{(1 + (i\omega\tau_{HN})^\beta)^\gamma},$$

in which β and γ are empirical parameters, $0 < \beta, \gamma \leq 1$ and $0 < \beta\gamma \leq 1$; β represents the broadening of the relaxation and γ represents the level of asymmetry of the relaxation. The HN equation reduces to Debye equation when $\beta, \gamma = 1$. The equation is known as Cole-Cole equation when $\gamma = 1$ and $\beta \neq 1$; it becomes Cole-Davidson equation when $\beta = 1$ and $\gamma \neq 1$. In HN relation, the relaxation time is given by

$$\tau = \tau_{HN} \sin^{-1/\beta}\frac{\beta\pi}{2 + 2\gamma} \sin^{1/\beta}\frac{\beta\gamma\pi}{2 + 2\gamma}.$$

Practically, it is common to analyze the data using simply the imaginary part of the permittivity, $\varepsilon''(\omega)$, and extract the value of τ at every temperature.

1.3.1.2 Vogel-Fulcher-Tammann (VFT) equation and the extraction of T_g

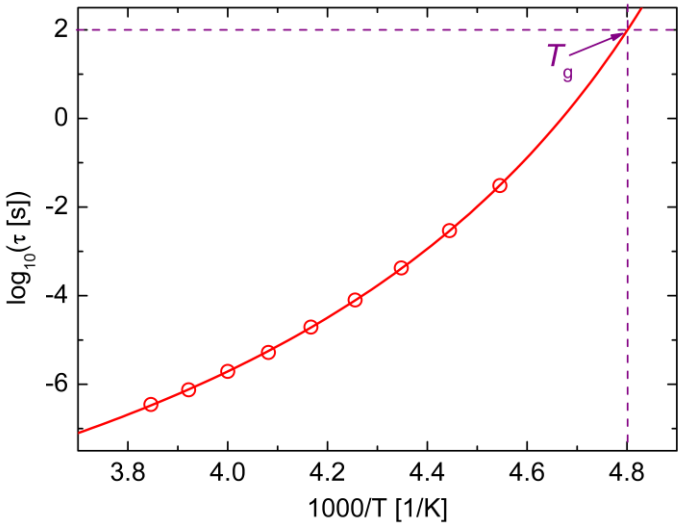

Figure 1.3 An example of VFT fitting and determination of T_g.

Unlike the most common temperature dependence, Arrhenius relation, in condensed matter systems, the typical temperature dependence of a polymer relaxation exhibits a more

complicated relation. At high temperatures (higher than T_g), it follows an empirical relation known as the Vogel-Fulcher-Tammann (VFT) equation

$$\tau = \tau_0 \exp\frac{DT_0}{T - T_0}, \text{ or } \log\frac{1}{\tau} = A - \frac{B}{T - T_\infty}.$$

T_0 and T_∞ are called the Vogel temperature. The physical understanding of this relation is still controversial and remains unclear.

In BDS measurements, data points of segmental relaxation time τ analyzed at every temperature T measured are fitted using the VFT equation. The temperature at which τ = 100 s is conventionally taken as the T_g of the polymer. An example is shown in Figure 1.3.

For secondary, local relaxations in polymer systems, instead of following the VFT relation, the relaxation exhibits the Arrhenius relation.

1.3.1.3 Conductivity signals in BDS measurements

Conductivity of the polymer system has a significant impact on the permittivity, and the ac conductivity is given by $\sigma^*(\omega) = i\omega\varepsilon_0\varepsilon^*(\omega)$, with $\varepsilon_0 = 8.854 \times 10^{-12}$ F/m being the vacuum permittivity. For $\varepsilon''(\omega)$ only, the conductivity effect, ideally, would appear as an additional term written as $\sigma_0/\varepsilon_0\omega$, with σ_0 being the (electronic) dc conductivity. However, in certain real cases, the following form is applied to take into consideration of the effect of conductivity:

$$\varepsilon^* = -ia\frac{\sigma_0}{\varepsilon_0\omega^S} + \varepsilon_{\mathrm{HN}}^*, \text{ therefore, } \varepsilon'' = a\frac{\sigma_0}{\varepsilon_0\omega^S} + \varepsilon_{\mathrm{HN}}'',$$

where $S \leq 1$ and a are empirical parameters.

We may easily tell that such a conductivity effect is very strong at low frequencies; it is inverse proportional to the angular frequency ω. When ε'' vs. ω is shown in a log-log plot, this conductivity effect appears as a line with slope $-S$. As a result, even for a weakly conductive material, this term may be so strong that all other dielectric relaxation signals are completely submerged in the low-temperature conductivity slope. This is when the BDS technique fails to measure the relaxations of polymer chains.

On the other hand, in a conductive material (not limited to polymers), the same technique may be used to directly characterize the conductive properties. The only difference

is that this time, $\sigma^*(\omega)$, instead of $\varepsilon^*(\omega)$, is plotted. It is known in various fields as impedance spectroscopy (IS).

1.3.2 Other techniques

Apart from the BDS technique, other techniques were applied in our work. These include the traditional differential scanning calorimetry (DSC) for T_g measurement, spectroscopic ellipsometry for thickness measurements, dynamic secondary ion mass spectroscopy (DSIMS) for depth profiles of various elements, atomic force microscopy (AFM) for surface measurements, and scanning transmission electron microscopy (STEM) for nanoscopic morphologies of the samples, for both bulk and thin films. A brief introduction of these techniques is provided here; some detailed information is included in the Experimental Section of the individual projects.

1.3.2.1 Differential scanning calorimetry (DSC)

DSC, as one of the most commonly used technique, measures the structural transition processes (glass transition, crystallization and melting) in polymer systems by monitoring the heat transfer as the temperature of the sample changes. In the amorphous polymer system studied in our projects, no crystallization and melting transitions exist. For glass transition on the other hand, the heat capacity of the sample changes as when the system goes from glassy state to rubbery state; this shows on the raw data as a step-like change. A midpoint of the step is taken to be the T_g of the polymer.

A typical DSC measurement determines the glass transition often by ramping through a temperature range at a constant ramping rate. It is important to note that the glass transition itself is not exactly a phase transition, but rather a phenomenological transition process. The glass transition indicates the temperature below which the measured system fails to be under equilibrium. In other words, T_g can be taken as the temperature at which the time used for measurement is equal to the typical time for the polymer system to reach equilibrium. Therefore, in DSC measurements, the value of T_g extracted is a function of the temperature ramping rate. Practically, if not stated otherwise, 10 °C/min is used; this is the ramping rate we used in our studies.

1.3.2.2 Spectroscopic ellipsometry

Spectroscopic ellipsometry, or simply ellipsometry, is a useful optical technique that obtains the dielectric properties of thin films. It is a powerful tool that characterizes the composition, roughness, crystallization, etc. in thin films. In this work, ellipsometry is essentially applied to obtain the thickness of polymer thin films, through established fitting methods. Ellipsometry also measures the T_g of thin film polymers, by monitoring their film thickness as a function of temperature.

Ellipsometry can also be used to obtain film thickness and other information, e.g. optical anisotropy, of conjugated polymers such as P3HT (see Chapter 4 for more details). Due to the strong light absorption within the visible wavelengths of these polymers, such experiments have to be performed by an ellipsometer with its light source extending to the infrared range.

1.3.2.3 Dynamic secondary ion mass spectroscopy (DSIMS)

DSIMS measures the composition of solid surfaces and thin films, by sputtering the surface of the sample using focused primary ion beam and collecting and analyzing the ejected secondary ions. The mass/charge ratios of these secondary ions are collected using a mass spectrometer to determine the type of ions ejected out of the sputtered material. The numbers of ions counted are then plotted against the depth of the sample (often a thin film), therefore the composition depth profile is obtained. However, due to the low resolution of the sputtering and ion ejection process, this technique does not provide quantitative information about the relative compositions among different elements, and it is typical that the resolution of the depth profile is no less than ~15 nm.

In our experiments DSIMS is used to provide information about the distribution of certain polymer chains or nanoparticles in polymer blends, copolymers or nanocomposites. An element unique to the target polymer or nanoparticle is used to indicate the depth profile of the component. In order to separate the thin film from the open environment (i.e. air), a sacrificial layer of deuterated PS (if the thin film is hydrogenated) or hydrogenated PS (if the thin film is deuterated), floated from deionized water, is applied on top of the thin film.

1.3.2.4 Atomic force microscopy (AFM)

AFM is traditionally used to measure the topography of surfaces, by means of detecting the van der Waals interaction between the sample surface and the AFM tip. AFM

is a common and reliable technique to determine the thickness of a polymer thin film by measuring the topography of a step between the film and the substrate.

In contact mode, AFM tip may also serve as an electrode. A so-called conductive AFM measurement may be performed by applying a voltage across a conductive thin film, between the AFM tip and the conductive substrate. Local current is measured, whose value depends on the location of the AFM tip. In such a way, a current map can be drawn, which, instead of a topography map that only provides information about the surface of the material, can reveal the structures underneath the surface. This technique is developed and applied in our group to measure the morphologies of P3HT thin films (see Chapter 4 for more details).

1.3.2.5 Scanning transmission electron microscopy (STEM)

STEM, compared to the conventional TEM, focuses the electron beam into a narrow spot which is scanned over the sample in a raster. The advantage of STEM is that it is able to measure local structures with very high resolutions (sub nanometer). For polymers, compared to the inorganic materials, the signal and contrast of the images are usually much lower due to the disorder and the much smaller difference among the atoms; at the same time, the energy of the electron beam is also limited as higher energy has a tendency to damage the material and its morphology.

In certain systems, the contrast of the STEM images may be enhanced by staining the sample in a vapor containing large atoms, e.g. iodine (I_2) and osmium tetroxide (OsO_4), depending on the system. For example, OsO_4 was used to stain the PI chains in the polymer blends of PS-*b*-PI and PS (see Section 2.2 for detailed information).

STEM only measures samples no more than a few hundred nanometers thick. To examine the morphology of bulk material, a slice of bulk sample, usually less than 150 nm thick, is prepared. In order for such a thin slice to hold together, the bulk sample is first embedded in epoxy before being sliced using a diamond knife. It is worth emphasizing that such a delicate preparation technique only applies to materials with relatively high T_g.

CHAPTER 2

SEGMENTAL DYNAMICS OF CHAINS TETHERED AT INTERFACES OF VARYING CURVATURES

This chapter is based on the following published article (with permission from the American Chemical Society):

- **H. Yang**, X.C. Chen, G.R. Jun and P.F. Green. Segmental dynamics of chains tethered at interfaces of varying curvatures. *Macromolecules*, 2013, *46* (12), 5036-5043.

2.1 Introduction

Polymer chains tethered at interfaces possess unique properties that render them to be of interest for a diverse range of technological applications. Pioneering research into structures and properties of chains end-tethered onto surfaces was performed by Alexander [20] and by de Gennes [21], using scaling theory, and later by others that include Semenov, Milner, Witten, and Cates [22-24]. Polymer chains are tethered to planar surfaces to create brush layers in order to control wetting properties and steric stabilization of colloidal particles in paints, as well as other functional uses such as membranes for antifouling and stimuli-responsive surfaces, and as functional switches for protein molecules [25-26].

Another class of tethered molecules involves star-shaped macromolecules [27]. This class of molecules, by virtue of molecular geometry, exhibits unusual wetting, dynamics and other physical properties, such as aging and glass transition behavior, compared to their linear chain analogues [28-31]. Of particular interest in this part of the work is the segmental

dynamics of chains tethered to interfaces of varying geometries. While theory and simulations have revealed significant information about the formation and dynamics of polymer brushes tethered to planar surfaces [20-24, 32-34], little is understood about chains tethered to surfaces of varying curvatures. Recently, work on the structure of tethered chains on curved surfaces became of interest; much of this is driven primarily by the need to control the organization of spherical nanoparticles, onto which chains are end-tethered, within block copolymer and homopolymer hosts [35], and block copolymer micelles [6-7, 36]. Research has been performed to understand the structure of brushes grafted onto concave surfaces, of porous structures [37-43]. However, while simulations, using self-consistent field theory (SCFT) or Monte Carlo, have examined the structure and dynamics of polymer chains tethered to such surfaces [37-38, 44-45], difficulties associated with controlling the geometry of the surfaces and the chain grafting densities lead to findings that are generally inconclusive. Nevertheless, there are obvious differences between the dynamics of chains tethered to planar versus curved surfaces. The dynamics of each tethered chain on a planar surface are hindered by neighboring chains and become more cooperative with increasingly high tethering densities. If the surface becomes concave it is tantamount to decreasing the effective grafting density; a convex implies the opposite.

One strategy that would enable a study of the dynamics of chains tethered to surfaces of varying curvatures, and hence geometries, is to exploit the structure of A-*b*-B diblock copolymers, well-known to possess morphologies of lamellar, bicontinuous, hexagonal and body centered cubic symmetries [46-47]. A-*b*-B copolymer chains mixed with homopolymer, A or B, chains as a minor component, tend to form micellar structures of different geometrical shapes. For the purposes of this study, our basic strategy was to choose an A-*b*-B copolymer such that the glass transition temperature, T_g, of one component is considerably higher than the other. In doing so the segmental dynamics of the low-T_g component is measured in the environment of the "frozen" high-T_g component of varying local curvatures. Surprisingly, little work has been done about the dynamics of the tethered chains in these systems [43, 48-49]. We note, on the other hand, that significant research has been conducted by researchers, including Adachi and Kotaka, Kremer, Roland, Watanabe, and their co-workers [50-58] on polyisoprene (PI) dynamics, and by Ngai, Colmenero, Roland, Watanabe et al. on segmental dynamics in its blends and block copolymers [59-62].

Here we specifically report the results of a study of the segmental dynamics of the PI segments in blends composed of 20 wt% polystyrene-*b*-polyisoprene (PS-*b*-PI) in polystyrene (PS) hosts of varying molecular weights. The PS-*b*-PI copolymer chains aggregate into tethered structures, micelles and multilayered onion-like structures. Broadband dielectric spectroscopy (BDS) was used to study the local PI dynamics and to determine the local T_gs of the PI-component. Additionally, modulated differential scanning calorimetry (MDSC) was used to measure the local T_gs of the PI-component within the samples. BDS measures the energy loss contribution, $\varepsilon''(\omega)$, the complex permittivity, associated with the alignment of dipoles in the polymer chains when an ac electric field is applied; the loss reflects the dynamics of the polymer chains. The BDS experiments yield clear, unambiguous information about the segmental dynamics of the PI component of the diblock because the dipole moment of the PS chains is negligible in comparison to that of PI in the temperature range of interest, even at low PI concentrations in the blends [48-49]. Through appropriate modulation of the parameters, the MDSC experiments were used to measure the local T_g of the PI domains in the samples.

We observed significant variations in segmental dynamics due to interface curvature/geometry that have not previously been reported. At the lowest temperatures, the PI segmental dynamics within the micelles were fastest, orders of magnitude faster than those in the layered onion-like structures; i.e. $\tau_{micelle} \ll \tau_{onion}$, where tmicelle represents the average segmental relaxation time of PI in the micelle and tonion is associated with relaxations in the onion-like structures. The PI dynamics within the layered onion-like structures were fast compared to those in the neat diblock copolymer lamellar and gyroid phases; $\tau_{lam} \sim \tau_{gyroid} \gg \tau_{onion}$. At high temperatures, the PI relaxation times were comparable, regardless of the local environment. The differences between the segmental relaxation rates in these different systems are consistent with trends in the local PI component T_gs. This behavior may reflect the frustration of packing of chain segments at the interfaces of varying curvatures, unique to each system, engendered by the requirement to maintain a constant segmental density throughout.

2.2 Experimental Section

The segmental dynamics of the PI component of neat PS-*b*-PI and of blends of PS-*b*-PI and PS homopolymer were investigated using BDS. MDSC was used to determine the T_g of the components of this blend. The morphologies of these samples were determined using scanning transmission electron microscopy (STEM) with a high-angle annular dark field (HADF) detector. Two PS-*b*-PI copolymers and a PI homopolymer, purchased from Polymer Source, and PS homopolymers of varying molecular weights (purchased from Pressure Chemical) were used in this study.

For one of the copolymers the molecular weights of the two blocks, PS and PI, were 65,000 and 26,000 g/mol, respectively; the components of the other were of molecular weight 42,000 and 26,500 g/mol, for the PS and PI components, respectively. They are denoted as PS(65k)-*b*-PI(26k) and PS(42k)-*b*-PI(26.5k) from now on. The PI homopolymer was of molecular weight 25,000 g/mol, designated as PI-25k. PS homopolymers of five different molecular weights were used: 13,000, 49,000, 152,000, 590,000 and 1,600,000 g/mol; these homopolymers are hereafter referred to as PS-13k, PS-49k, PS-152k, PS-590k, and PS-1600k, respectively.

A series of samples were fabricated for BDS measurements (Novocontrol Technologies, GmbH) using the following procedures. Copolymer/homopolymer blends, each composed of 20 wt% of PS-*b*-PI and a PS homopolymer were dissolved in toluene. The toluene was then allowed to evaporate from each solution and the remaining material was annealed under vacuum at a temperature of 60 °C in vacuum (< 100 mTorr) for 24 h; they were then annealed at 120 °C for 48 h and subsequently allowed to cool to room temperature. The domain structures and mesophases were stable at or below 120 °C after the annealing. Each mixture (as well as the pure PS-*b*-PI diblock) was then sandwiched between two brass plates, 10 mm in diameter, which served as electrodes (top and bottom) for the BDS measurements. The BDS measurement protocol first involved heating the sample at 120 °C to ensure that the polymer wets both electrodes and to ensure sample thickness uniformity. The samples in our experiments were typically in the thickness range of 100-200 μm. After annealing, each sample was cooled down to 170 K at a ramping rate of 3 °C/min. The full BDS measurement, with the ac voltage frequency spanning from 0.1 Hz to 1 MHz, was then performed throughout the temperature range from 170 to 310 K; measurements were performed at 5 K intervals.

Because of the low fraction of the PI component in the blends (less than 10 wt% of the total), the absolute intensities of the PI relaxation peaks in ε'' spectra were weak. Since the background noise is frequency-dependent, but temperature-independent, then instead of plotting ε'' as a function of frequency for various temperatures (frequency sweep), ε'' is plotted as a function of the temperature measured for various frequencies (temperature sweep). Both types of experiments yield the same temperature dependence of the dynamics.

The MDSC measurements were performed on samples prepared the same way as described above for the BDS measurements. Samples of the mixtures and of the neat copolymer, each of approximately ~5 mg in weight, were each sealed in a Tzero DSC pan and tested using a TA Instruments DSC Q200, equipped with a liquid nitrogen cooling system (LNCS). Each sample was kept at 120 °C for 20 min, and then cooled at 3 °C/min to −120 °C. After each sample reached equilibrium at a specified temperature, it was measured with modulation temperature amplitude of 1.5 °C and modulation period of 60 s and ramped at 3 °C/min up to 0 °C.

The STEM images were made of microtomed cross sections, ~120 nm in thickness, from bulk samples embedded in epoxy. Microtoming was performed at room temperature using a Reichert Ultracut-E ultramicrotome equipped with a diamond knife. In order to create sufficient contrast to enable the PS and PI components to be discerned using STEM, the samples were stained by exposing them to osmium tetroxide (OsO_4) vapor for 30 min.

We conclude this section by noting that the copolymer is highly phase segregated throughout the temperature range of interest (~150-310 K) in our experiments; the Flory-Huggins interaction parameter $\chi = -0.07 + 63/T$ [63], and the total degree of polymerization $N = N_{PS} + N_{PI} = 625 + 310 = 935$. Moreover, since the T_g of PS is ~373 K, the PI chains are able to undergo relaxation processes in an environment anchored to, and confined by, the rigid PS phase.

2.3 Results and Discussion

It is known that bulk PI chains undergo three basic relaxation processes: normal mode relaxations (end-to-end dynamics of the chains), segmental (α-) relaxations and secondary (β-) relaxations [50-51, 57, 64]. The α-relaxations measured in our experiments show that the anchoring of PI chains to the rigid PS/PI interface strongly suppresses the normal mode

relaxations of PI; the β-relaxation intensities are low. The segmental relaxations of the PI components are plotted in Figure 2.1 for copolymer chains under different interfacial curvature and geometrical environments. It is evident from all these data that the relaxation times are comparable at high temperatures, whereas at lower temperatures the differences are significant.

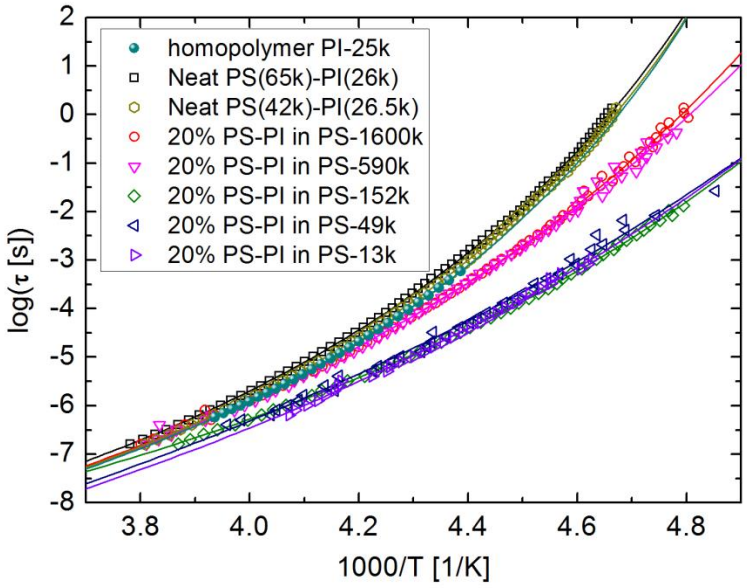

Figure 2.1 Segmental relaxation time vs. inverse temperature (1000/*T*), of homopolymer PI-25k, and of the PI-block in two neat copolymers, PS(65k)-*b*-PI(26k) and PS(42k)-*b*-PI(26.5k), as well as the blends of 20 wt% PS-*b*-PI and 80 wt% PS host of various molecular weights. The solid curves are the VFT fitting of the data of each sample, respectively.

We begin by discussing the dynamics of the pure diblock copolymers in order to establish a basis for our subsequent discussion of the behavior of the tethered mesophases (onion-like and micelles) in the PS host environments. The magnitudes of the segmental relaxations, and the temperature dependencies, of the PI component in the gyroid τ_{gyroid} (for diblock PS(65k)-*b*-PI(26k)) and the lamellar τ_{lam} (for diblock PS(42k)-*b*-PI(26.5k)) phases are almost identical for all temperatures; $\tau_{gyroid} \sim \tau_{lam}$. The margin of experimental error is smaller

than the data symbols. The temperature dependencies of these data are well described using the Vogel-Fulcher-Tammann (VFT) equation

$$\log\left(\frac{1}{\tau}\right) = A - \frac{B}{T - T_\infty}$$

using the very similar fitting parameters of A, B, and T_∞. The T_gs of the PI component, in all systems, were estimated as the temperature at which the segmental relaxation time $\tau = 100$ s; this is a reasonable assessment of the T_g and has been universally applied. This procedure generally provides reasonable estimates of T_g determined using other techniques. Note that since T_g is not a true thermodynamic phase transition, but in fact exhibits a weak, nearly logarithmic dependence on cooling rates, this protocol is not unreasonable. With this estimate the T_g of the PI component in both phases are 208.5 ± 0.5 °C; see Table 2.1.

Table 2.1 The T_gs of the PI component in each system studied, extrapolated from the dynamics measured by BDS.

Sample	T_g [K]
neat diblock PS(65k)-*b*-PI(26k) neat diblock PS(42k)-*b*-PI(26.5k) homopolymer PI-25k	208.5 ± 0.5
20 wt% PS(65k)-*b*-PI(26k) in PS-1600k	201.7
20 wt% PS(65k)-*b*-PI(26k) in PS-590k	200.8
20 wt% PS(65k)-*b*-PI(26k) in PS-152k	192.8
20 wt% PS(65k)-*b*-PI(26k) in PS-49k	191.3
20 wt% PS(65k)-*b*-PI(26k) in PS-13k	192.1

It is important to compare these relaxations with the segmental relaxation times τ_{homo} of PI homopolymer chains of the same molecular weight. The data in Figure 2.1 reveal that these rates were slower by nearly a factor of 2, throughout a wide temperature range, i.e. $\tau_{lam} \sim \tau_{gyroid} \sim 2\tau_{homo}$. The homopolymer T_g was, within experimental error, identical to T_gs of the

PI components in the copolymer phases, using the same protocol. Faster homopolymer chain dynamics are expected because in the copolymers the dynamics of certain PI segments are connected to the "immobile" PS phases with higher T_g. Since the dynamics of the segments closer to the tethered ends would be suppressed in comparison to segments at the chain ends, the average dynamics of the segments that compose the tethered PI components would be slower; hence, $\tau_{lam} \sim \tau_{gyroid} \sim \tau_{homo}$. Simulations [65] reveal that for the lamellar phase of an A-*b*-B diblock copolymer in which the dynamics of component A is faster than those of the component B, the dynamics of the A-block close to the A/B junction are slower than those of the homopolymer A, of the same degree of polymerization. Additionally, experiments performed on polystyrene-*b*-poly(dimethylsiloxane) (PS-*b*-PDMS), in which PS has a T_g over 200 K higher than that of PDMS, reveal that the PDMS block segmental dynamics are slower than those of pure PDMS [48-49].

The tethered points lie within an interfacial region of finite width δL. Within this region the junctions necessarily undergo local displacements due to a local gradient in the glass transition from that of PS to the PI phases. This local gradient in T_g is temperature dependent because the interfacial width is temperature dependent; it scales as $\delta L_{PS/PI} \propto \chi^{-1/2}$ [66]. The temperature dependence is weak. The mobility of the tethered points would be the reason that the segmental dynamics of the PI components in the ordered phases are not significantly different from those of the homopolymers. We also note that while the gyroid phase is characterized by both concave and convex surfaces, its behavior should not be very different from that of the lamellar phase, since any potential effects of fluctuations in local "packing" would have a counterbalancing effect based on these differences in concave and convex local curvature throughout the entire sample.

Having addressed the behavior of the pure systems, the role of geometry/confinement and interfacial curvature on the segmental dynamics is now examined in the blends, where the copolymers comprise the minor component and form localized mesophases within the PS homopolymer hosts. The copolymers form different ordered structures in an effort to minimize the unfavorable PS/PI interactions. In these systems we found that when $P \gg N$, where P is the degree of polymerization of the PS host, the copolymers form the "onion-like" structures and for $P \sim N$ or smaller, cylindrical micelles are formed [6-7, 67]. Note that the PI segments are necessarily confined on concave surfaces that shield them from the PS homopolymer phase.

The micelles are composed of an inner core of PI and outer corona chains of PS in a PS host environment in order to minimize the unfavorable PS/PI interactions. The copolymer chains must assume non-optimal conformations in order to form the micelles. The sizes of the micelles are determined by the relative values of P and N_{PS}. When the host chains are comparable to or short compared to the PS-block in the corona, they intermix with the corona chains ("wet-brush" scenario). As a result, the chains in the corona stretch and the chains of the PI-block are compressed in order to maintain a constant monomer density; this leads to small micelle cores [6-7, 9, 68-69]. Hence the micelle sizes increase with increasing P. The geometries of the micelles are dictated, in part by the asymmetry of the size of the block components and the molecular weight of the PS host chains. This is the reason why cylindrical micelles are formed. We note that in the specific cases of thin films, the formation of cylindrical micelles is suppressed.

For the blends containing very long host chains, $P \gg N$, experience a completely different situation. Since the translational entropy gain of the homopolymers is appreciably less than the conformational entropic penalty, the intermixing with the PS corona is reduced considerably ("dry-brush" scenario) [6-7, 9]. The onion-like structure formation enables a decrease of interfacial free energy cost of the PS and PI enthalpic interactions, relative to micelle formation [67]. STEM images and schematic of all the morphologies (gyroid, onion-like structure and micelles) are shown in Figure 2.2.

The temperature dependencies of the PI α-relaxations, for the PS-*b*-PI diblock copolymers in all the PS hosts of varying P (P = 15400, 8650, 5670, 1640, 470 and 125, for all the host molecular weights studied), plotted in Figure 2.1, reveal that the relaxation rates, and their temperature dependencies fall in two different categories. For the cases where P = 15400, 8650, and 5670 (i.e. $P \gg N$), where the copolymers form onion-like mesophases, the rates and temperature dependencies are comparable. For P = 1640, 470 and 125, the rates and their temperature dependencies were comparable, though not identical; cylindrical micelles are formed in these samples. While the lengths of the cylindrical micelles increase with increasing P (from >150 nm for P = 1640 to ~45 nm for P = 125), the magnitude of the α-relaxations and their temperature dependencies remain the same. As mentioned above, the magnitude and temperature dependencies of the PI segmental dynamics fall in distinct categories; each category is associated with a very different geometrical environment. As

long as the geometry of the micelle remains constant, the dynamics are approximately independent of the host chain length and the size of the micelle or layered structure.

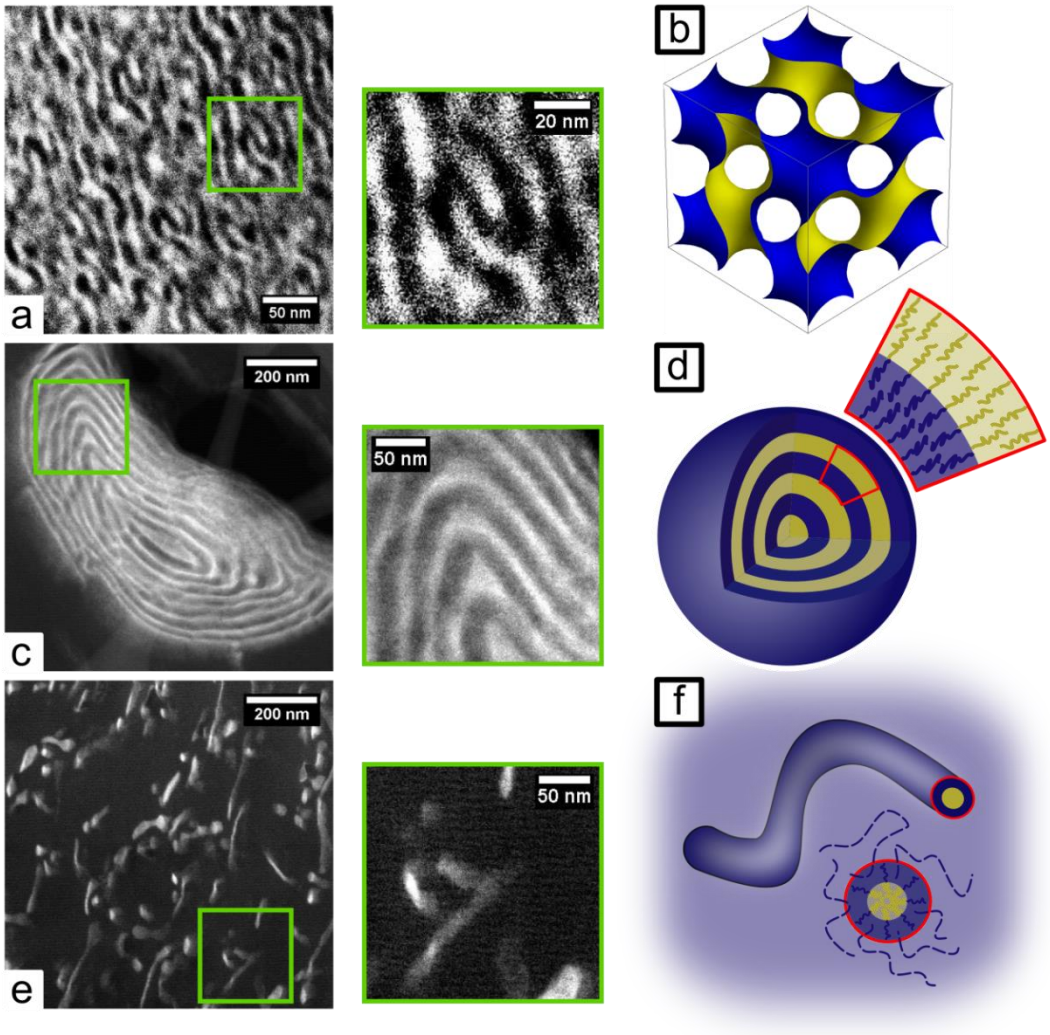

Figure 2.2 The cross-sectional STEM images ((a), (c) and (e), with a certain part zoomed in for each image) as well as the corresponding schematic diagrams ((b), (d) and (f)) of the bulk samples of neat PS(65k)-*b*-PI(26k) ((a) and (b), double gyroid), 20 wt% PS(65k)-*b*-PI(26k) in PS-1600k ((c) and (d), "onion-like") and 20 wt% PS(65k)-*b*-PI(26k) in PS-152k ((e) and (f), cylindrical micelle). These domain structures and mesophases are stable at or below 120 °C after the annealing.

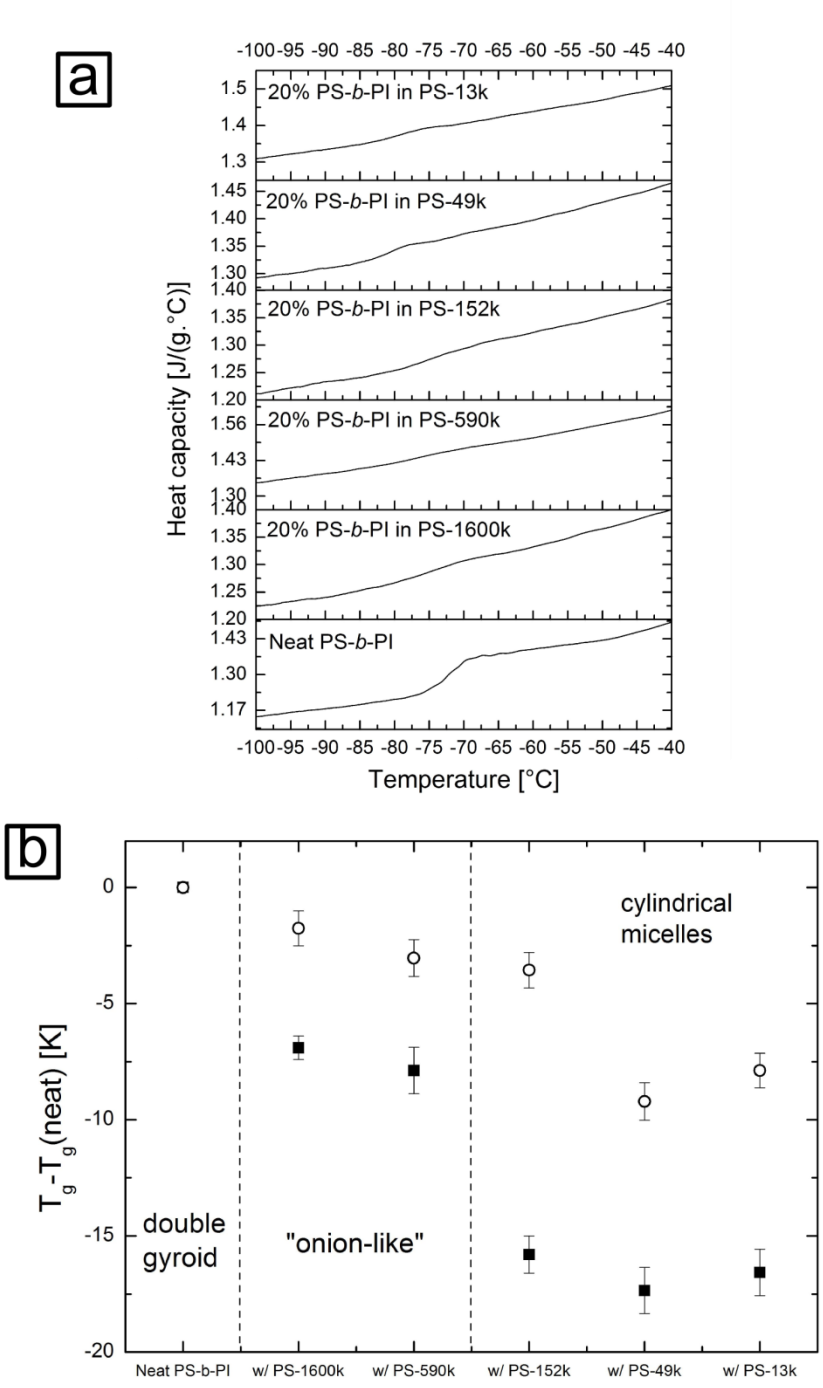

Figure 2.3 (a) Heat capacity of all the systems vs. temperature, measured using MDSC. (b) T_g of all the systems relative to that of the neat PS(65k)-*b*-PI(26k), from the BDS (filled squares) and MDSC (open circles) measurement, the latter of which was calculated from the results plotted in (a).

The T_gs of the PI components in the samples are tabulated in Table 1; the trends in the T_g of the local PI are consistent with trends in the segmental relaxation rates. The PI-block in the blends containing the layered onion-like structures possessed local T_gs ~ 201 K; these T_gs are smaller than those of the pure copolymers and the homopolymer. This difference in T_gs would be consistent with the faster dynamics. In the case of the micellar structures the local PI T_gs were lower (192 K). These rates are also consistent with the faster dynamics exhibited by the PI chain segments. Clearly, relative magnitudes of the T_gs estimated using the VFT relationship are consistent with the differences between the magnitudes of the PS segmental dynamics in the different environments.

Before discussing the observations further, MDSC measurements of each sample were performed to independently determine the T_gs of the PI components in the materials. The MDSC data representing the heat capacity vs. temperature behavior are plotted in Figure 2.3a for all the samples. A comparison of these values of T_gs with those estimated from the VFT fits are plotted in Figure 2.3b. While the T_gs determined using MDSC are higher, the dependencies on PS composition are consistent. In this regard these MDSC measurements corroborate the results of the BDS measurements.

It is clear from the foregoing that systems with similar structures share similar dynamics and similar local T_gs. A natural question however is whether the length scale of confinement in these systems could be used to reconcile the differences between the dynamics. Currently it is understood that in amorphous systems, apart from reasons such as attractive or repulsive polymer-"walls" interactions, structural effects including packing and conformational changes, or local density variations, faster dynamics exhibited by polymer chains under confinement are associated with the fact that the length scale of confinement is comparable to the size of the cooperatively rearranging region (CRR); the CRR is usually no greater than a few nanometers [70-72]. However, this explanation is not appropriate for the systems discussed here. In the structures shown in Figure 2.2, the length of confinement in the double gyroid is ~7 nm, whereas those in the onion-like structures and cylindrical micelles are both 10-15 nm. Hence no correlations between the dynamics and the length scale of confinement have been observed.

We plotted the dielectric strengths $\Delta\varepsilon$ of the α-relaxations for the neat copolymer PS(65k)-b-PI(26k) and for all the blends, in Figure 2.4. $\Delta\varepsilon$ was calculated by extracting, from the plot of ε'' vs. temperature at a certain frequency, the difference between the values of ε''

at the maximum and the background (at low temperatures far away from the location of the maximum). These data indicate that the $\Delta\varepsilon$ associated with each blend is approximately 20% of intensity of the neat copolymer, indicating that the dielectric strengths scale with the weight fraction of the PI chains in the blends. We note, moreover, that these intensities are temperature independent, within experimental error (data not shown here). In short the PI segments in each system contribute proportionally to the response throughout the temperature range of interest.

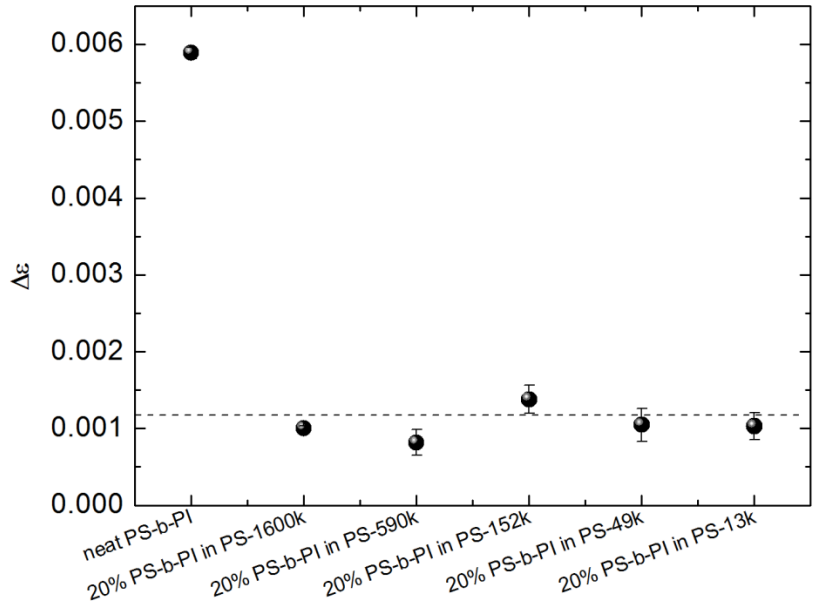

Figure 2.4 The dielectric strength $\Delta\varepsilon$ of the α-relaxation of the PI domains in the neat copolymer PS(65k)-b-PI(26k) and its blends with various PS hosts. The dashed line indicates 20% of the intensity of the neat copolymer, where the intensity scales with the weight fraction of the PI chains. The error bars were calculated from the fluctuation of $\Delta\varepsilon$ against the measured temperatures.

In light of the differences in the magnitudes of the dynamics in these different material systems, it is worthwhile to understand whether insights into this behavior may be gleaned from dynamic fragility. The fragility is defined as

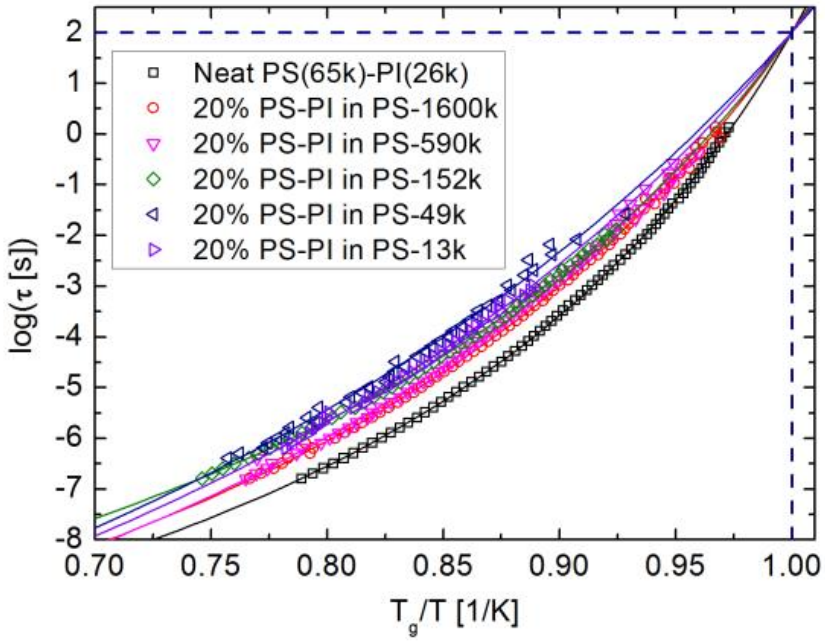

Figure 2.5 The segmental relaxation time vs. T_g/T, of the PI-block in neat PS(65k)-*b*-PI(26k), as well as the blends of 20 wt% PS(65k)-*b*-PI(26k) and 80 wt% PS-1600k, PS-590k, PS-152k, PS-49k and PS-13k, respectively. The solid curves are the VFT fitting of the data of each sample, whose slope at $T_g/T = 1$ and $\log \tau = 2$ equals the value of the fragility *m*.

$$m = \frac{\mathrm{d}[\log \tau]}{\mathrm{d}(T_g/T)}\Big|_{T=T_g}$$

The value of m implies the deviation of the temperature dependence from the Arrhenius behavior, and how rapidly the dynamics decrease as the temperature approaches T_g. Increasing values of m may be interpreted as an increase in the configurational entropy of the system; in network glasses the values of m increase as the directional covalent bonding network structure of the glass (e.g. SiO_2 and GeO_2) becomes "depolymerized" with the replacement of covalent bonds with ionic bonds. The fragility is also used as a measure of the intermolecular cooperativity in the dynamics; larger values of m are associated with increasing cooperativity of the dynamics [70, 73]. The relaxation time vs. T_g/T data are plotted in Figure 2.5. The values of m were determined from the slopes of the lines at T_g/T

= 1, where T_g is defined as the temperature where log τ = 2. The *m* may also be readily calculated from the VFT parameters *A*, *B*, and T_∞, whose values are tabulated in Table 2.2. The fragilities, reported in Table 2, suggest qualitatively that as the T_g of PI-block decreases, the fragility decreases. This trend is consistent with the reported effect on the dynamics of systems under confinement [70, 74-78]. Note that the fragility, apart from the abovementioned definition, may also be quantified using B/T_∞; larger values of B/T_∞ are associated with lower fragility. It has been pointed out by Angell and coworkers that these two definitions are related; the two fragilities show the same qualitative trends for our systems. Fragility has been reported to be sensitive to the temperature dependence of the size of the CRR close to T_g [77], but its fundamental relation with the structure remains unclear.

Table 2.2 The VFT parameters *A*, *B* and T_∞, as well as the calculated fragility value *m* of the PI component in each system studied, calculated from the BDS data.

Sample	*A*	*B* [K]	T_∞ [K]	Fragility *m*
neat diblock PS(65k)-*b*-PI(26k)	12.87	573.0	170.1	103.6
20 wt% PS(65k)-*b*-PI(26k) in PS-1600k	13.69	751.3	153.9	66.1
20 wt% PS(65k)-*b*-PI(26k) in PS-590k	14.29	854.0	148.3	62.4
20 wt% PS(65k)-*b*-PI(26k) in PS-152k	12.78	663.1	148.0	63.5
20 wt% PS(65k)-*b*-PI(26k) in PS-49k	15.43	1122	126.9	51.8
20 wt% PS(65k)-*b*-PI(26k) in PS-13k	14.85	967.3	134.7	56.4

Because the chains reside in different local structural environments in the systems, then it is anticipated that the distribution of relaxation times might be different [63]. To this end we compared the widths of the BDS data; see Figure 2.6. The peaks are normalized at a frequency of 9.75 kHz and plotted as a function of $T - T_{max}$, where T is the experimental temperature and T_{max} denotes the temperature where the maximum of ε'' is located at 9.75

kHz. Note here that this comparison, plotting the peaks as a function of temperature, has been done by others in the literature [79-80], instead of a frequency-sweep experiment. The width of the peak representing neat PS-*b*-PI (gyroid) appears to be the smallest, and that of the blend with PS-152k (cylindrical micelle) is the greatest. This observation of the broadening is consistent with that observed by others and suggests that the heterogeneity of the dynamics associated with the PI domains of the blends. The heterogeneity is most prominent in the cylindrical micellar structures.

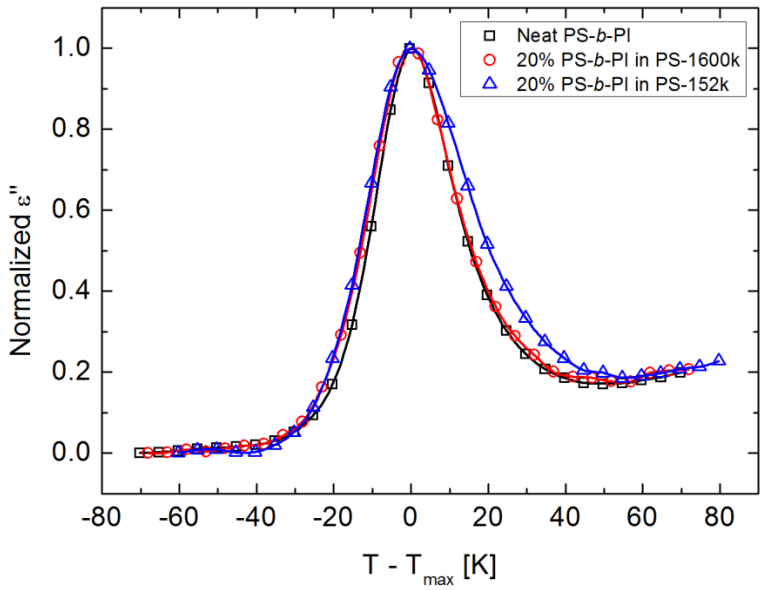

Figure 2.6 The normalized ε'', at a frequency of 9.75 kHz, is plotted as a function of the difference between the experimentally measured temperature and the temperature T_{max}, denotes the location of the maximum of ε'' for the PI-block in: neat PS(65k)-*b*-PI(26k); blend of 20 wt% PS(65k)-*b*-PI(26k)/ 80wt.% PS(1600k); 20 wt% PS(65k)-*b*-PI(26k)/ 80 wt.% PS(152k).

The aforementioned clearly indicates that the local geometrical environment influences the local free volume, as evidenced by the dependence of the local T_g on the geometry. The geometry, in this regard, largely dictates the magnitude and temperature dependence of the segmental dynamics. In light of this we now comment on experiments that bear an important relation to our experiments. Valle-Carrandi et al. studied the PDMS

dynamics of PDMS homopolymer chains confined within a microphase separated, asymmetric, diblock copolymer of PS-*b*-PDMS [49]. Through control of the volume fraction of PDMS, they prepared samples of three morphologies: lamellar, cylindrical and spherical. They showed that the PDMS dynamics were faster in the cylindrical and spherical nanophases than in the lamellar phases. Differential scanning calorimetry (DSC) measurements of the local PDMS T_gs are consistent with these trends in the dynamics. They suggested that the dramatic changes in dynamics was due to the poor packing of the PDMS segments, associated with the frustration of segmental organization and conformations at the interfaces of varying curvature. While this system is quantitatively different from the system we examined, the results are qualitatively consistent with our findings with regard to the role of geometrical confinement on the segmental dynamics.

2.4 Conclusion

It has been carefully demonstrated that the local curvature of the environment in which the copolymer chains are confined has a significant impact on the segmental dynamics of the low-T_g component of PI. The segmental α-relaxation rates are similar in the neat copolymers and are slightly slower than those of the homopolymer PI, $2\tau_{homo} \sim \tau_{lam} \sim \tau_{gyroid}$, under moderate temperatures above the T_g of PI. These results are consistent with simulations and experiments of others. However the segmental relaxation rates of the PI components in the layered onion-like and micelle structures are considerably faster: $\tau_{lam} \sim \tau_{gyroid} \sim 2\tau_{homo} \gg \tau_{onion} \gg \tau_{micelle}$. These results indicate that systems with similar nanostructures exhibit similar magnitudes and temperature dependences in their segmental relaxation rates and possess the same local T_gs. The relaxation rates in Figure 1 manifest information about the local "packing" of chain segments that accommodate the local changes in curvature of the morphology necessary to maintain a constant segmental density throughout. Notably, the local T_gs of the PI components manifest the differences in the local packing. Because the VFT, or equivalently the Williams-Landel-Ferry (WLF), parameters are dependent on free volume, the temperature dependencies of the α-relaxation rates would reflect the differences in local free volume unique to the morphology of each class of samples. The morphology, due largely to the "frozen" high-T_g PS component, would exhibit a different behavior of

local specific volume vs. temperature, relation associated with the local curvature of the interfaces.

CHAPTER 3

ROLE OF SPATIAL COMPOSITIONAL HETEROGENEITY ON COMPONENT DYNAMICS IN MISCIBLE POLYMER/POLYMER BLENDS

This chapter is based on the following published article (with permission from the American Chemical Society):

- **H. Yang** and P.F. Green. Role of spatial compositional heterogeneity on component dynamics in miscible bulk and thin film polymer/polymer blends. *Macromolecules*, 2013, *46* (23), 9390-9395.

3.1 Introduction

While much is known about the structure and properties of miscible polymer/polymer blends, there remain a number of lingering questions regarding their dynamics, which are known to have a complicated connection to composition and structure [10-11, 13, 59-61, 79, 81-89]. It is now well understood that in a miscible A/B blend the mixing between the A and B monomers is not random; there is a higher than random probability that the nearest neighbor of a given monomer is an identical monomer, so the local effective composition, φ_{eff}, is different from the average blend composition [10, 81, 89-91]. This difference is due to two effects, namely chain connectivity [81, 90-91] and thermally driven density and concentration fluctuations [81, 89]. This heterogeneity in the composition, believed to be on the order of nanometers in spatial dimension, is responsible for local variations in the glass transition of the blend and manifested in the behavior of the dynamics of the A and B

components. The magnitudes of the segmental relaxations in the blend, of the individual components, can differ by orders of magnitude [14, 83, 92]. The temperature dependencies of the translational diffusion coefficients of the individual components in the blend each are well described by the Vogel-Fulcher-Tammann (VFT) equation, with fitting constants similar to those of their pure homopolymer environments [10-11, 13, 59, 79, 81-83]. Each component has been shown to experience its distinct glass transition temperature, T_g, locally [10, 12, 81, 90]. Each component resides in a distinct local compositional environment and therefore possesses a distinct friction factor ζ. It is important to recall that the longest relaxation time τ is proportional to ζ, and the tracer diffusion coefficient scales as $1/\zeta$ [93], so it is not surprising that whereas in the case of homopolymers the dynamics are known to obey the time-temperature superposition principle (TTSP); TTSP fails to describe the dynamics of miscible blends. The average T_g of a miscible blend, as measured using differential scanning calorimetry (DSC), exhibits a broad transition, occurring over a much wider temperature range, compared to that of its individual components. This is due to spatial compositional heterogeneity; the broadening is particularly significant when the T_gs of the components differ by tens of degrees [11, 13, 61, 79, 81-82].

Studies of blends in which there exists a large disparity between the T_gs of the components suggest that at sufficiently low temperatures where the higher-T_g components becomes glassy the lower-T_g component undergoes relaxations within this glassy confined environment. The temperature dependence of the segmental dynamics in this sufficiently lower temperature regime is Arrhenius; the dynamics of poly(vinyl methyl ether) (PVME)/polystyrene (PS) blends are illustrative of this behavior [11, 81-83, 91, 94]. The dimensions of these glassy confining domains are believed to be on the order of nanometers [95].

While chain connectivity and thermally driven concentration fluctuations are responsible for compositional heterogeneities both in bulk and thin films, interfaces in thin films also strongly influence the local blend composition and indeed the phase stability. Near a free surface the component with lower surface energy preferentially adsorbs to the surface, in excess of its bulk concentration. The same is true at a substrate when one component has a preferential interaction. Both effects locally distort the compositional profile, even far from the critical temperature. We recently showed [96], using X-ray photon correlation spectroscopy (XPCS), that PVME chains at the free surface of thin film PVME/PS blends

relax at faster rates than those located in the interior of the film. These PVME chains, moreover, exhibit dynamics that manifest the local surface composition.

Here we report the results of a study of the dynamics of the PVME component in bulk and thin film PVME/deuterated PS (dPS) mixtures in the single-phase region of the phase diagram. Our results are interpreted based on the notion that the dynamics of the individual components in a miscible blend manifest the local compositional environment they each experience. We show that the segmental relaxations in the bulk, denoted by the maxima in the dielectric response, as measured by broadband dielectric spectroscopy (BDS), exhibit VFT-like temperature dependence at high temperatures, manifesting the fact that the chains move within the same average environment. This would be the well-known α-relaxation. However, with decreasing temperature T there is evidence, based on the dominant relaxations of PVME chains, where the relaxations occur in two distinct local compositional environments. One relaxation process, which we suggest occurs in an environment rich in PS, exhibits a much stronger temperature dependence. This relaxation process "freezes" in a temperature range comparable to the T_g of the blend, measured using DSC; we denote this as the α_0-process. The second process, which persists at lower temperatures and becomes Arrhenius at sufficiently low temperatures, is associated with PVME chains relaxing within the confines of glassy dPS domains; this latter relaxation (the Arrhenius regime) has been identified by others as the α′-process. We also examined thin film PVME/PS blends confined between aluminum (Al) substrates, where the PVME chains preferentially segregate to the polymer/substrate interface to form a PVME-rich layer. We observed the emergence of an additional relaxation process, α_{int}, associated with these chains at the interface. It is apparent from this study that the dominant segmental dynamics in these miscible blends manifest the behavior of chains residing in distinct local compositional environments.

3.2 Experimental Section

The dynamics of both 100 nm thin film and bulk blends of PVME and dPS (both purchased from Polymer Source), containing different amounts (5, 25, 35 wt%) of PVME, were studied using BDS; these blends are hereafter denoted as the 5%, 25% and 35% blends. PVME, with number-average molecular weight M_n = 24.4 kg/mol and polydispersity index (PDI) of 1.08,

was refrigerated with desiccants prior to use. Two different dPS were used in this study: one with M_n = 3.8 kg/mol and PDI = 1.05 was used for the thin film samples, and the other with M_n = 4 kg/mol and PDI = 1.5 was used for the bulk samples; they are designated as dPS3.8 and dPS4, respectively. The T_gs of dPS3.8, dPS4, and PVME were determined to be 352, 353, and 248 K, respectively. The T_gs of the 5%, 25%, and 35% blends, measured by DSC, are 326, 294, and 281 K, respectively.

Bulk PVME/dPS4 mixtures, a few milligrams in weight, were first dissolved in toluene, then dried, and subsequently annealed at 340 K for 48 h. This temperature is much lower than the lower critical solution temperature (LCST) of the mixture [97-98], so the two components in the blend remained miscible throughout the preparation and subsequent measurement using BDS. The materials were then sandwiched between two brass plates of 1 cm in diameter; the two plates were used as electrodes in the experiment. In order to maintain a specific separation between the brass plates, especially at high temperatures when the viscosity of the blend becomes low, silica spacers of 50 μm in diameter were placed between the electrodes. Because of probable exposure to air during transfer, the samples were annealed once again in the BDS cryostat under nitrogen (N_2) atmosphere at 340 K for 10 h; this ensured that moisture, potentially absorbed during the sample transfer, was removed. The removal of moisture was further confirmed by the absence of the BDS signal associated with the moisture [79]. After *in situ* N_2 annealing, BDS measurements were performed in a frequency range from 0.1 Hz to 1 MHz at temperatures between 250 and 325 K with a step increase of 1 K, throughout which the relaxation(s) of PVME segments in the blend were active. BDS experiments were also performed on the neat PVME sample. This sample was annealed at 343 K for 3 h and then cooled down to 152 K prior to the measurement. The BDS measurements were conducted throughout the temperature range from 152 to 297 K.

Thin films of the PVME/dPS3.8 blends were prepared and confined between two Al electrodes using a thin film sample preparation procedure for BDS, described elsewhere [99]. Briefly, Al electrode strips, 0.5-0.8 mm in width and ~100 nm thick, were evaporated onto glass substrates (1 cm × 1 cm × 1 mm). Prior to evaporation, the substrates were thoroughly cleaned using glass detergent and acetone in the ultrasonic cleaner. Toluene solutions of the PVME/dPS3.8 blends were spincoated onto the cleaned Al substrate to fabricate 100 nm thick films. A spectroscopic ellipsometer (SE; J.A. Woollam) was used to determine the film

thicknesses. Samples were then vacuum-dried overnight at room temperature and subsequently annealed at a temperature of 340 K for 48 h. Al counter electrodes were deposited on top of the thin films. Because of the probable exposure to air, samples were annealed once more in the BDS cryostat under N_2 atmosphere at 340 K for 10 h to remove the absorbed water during the sample transfer. The ac voltages applied to the films during our experiments were chosen to be 0.3 V for 100 nm films. The other experimental parameters and procedures were the same as those for studying the bulk samples.

The depth profile of PVME throughout the film, and in particular at the Al/polymer interface, was determined using dynamic secondary ion mass spectroscopy (DSIMS). While the blends that were examined using BDS were sandwiched between two Al electrodes, the sample prepared for DSIMS analysis was spincoated on an Al substrate, exposing the other surface. This was necessary so that the depth profile of hydrogen (H) at the Al/polymer interface, due to the PVME, could be determined by DSIMS. The details are as follows. Thin films of the PVME/dPS3.8 blend, with thickness 105 nm, were spincoated on the Al-deposited silicon (Si) substrates and annealed at 340 K for 48 h. A sacrificial hydrogenated PS (hPS) layer was then placed on each film in order to perform the DSIMS measurements, ensuring a constant etch rate. This hPS layer (purchased from Pressure Chemical, M_n = 143.4 kg/mol, PDI = 1.06) was of thickness 50 nm; it was first floated onto hot deionized water which is known as a nonsolvent for PVME above 308 K [100]. The sacrificial layer hPS film was then promptly placed on the thin film blend for DSIMS analysis. The DSIMS experiments were performed, using a Physical Electronics 6650 Quadrupole instrument, by Dr. Tom Mates of the University of California at Santa Barbara. A Cs^+ primary ion beam (6 keV and 50 nA) was used to sputter the samples with a 350 μm × 450 μm raster area, and negative secondary ions of H, deuterium (D), carbon (C), Al, and Si were monitored from the center 15% of the crater area. Independent data from thickness measurements, using SE, were used to convert the sputtering time axis to the appropriate depth scale.

3.3 Results and Discussion

Much is known about the dynamics of the bulk blends of PVME/PS [11, 81-83, 91, 94]. We show typical plots of the dependencies of the imaginary part of the permittivity ε'' on the frequency of the applied ac voltage for PVME/dPS4 blends and for pure PVME in Figure

3.1. Broader segmental α-relaxations were observed in the blends, compared to the homopolymer, as expected. The α-relaxations in pure PVME are characterized by comparatively narrow peaks, with intensities that are temperature independent, whereas the peaks representing the blend relaxations are broad and decrease significantly with decreasing temperature [11, 59, 81-82, 94]. It is customary to fit the ε'' vs. frequency profiles (typically determined from a "frequency sweep" experiment) using one or a sum of Havriliak-Negami functions, from which the characteristic relaxation time τ ($\tau = 1/2\pi f$) associated with the maximum may be identified as the segmental relaxation time of the blend, for that temperature.

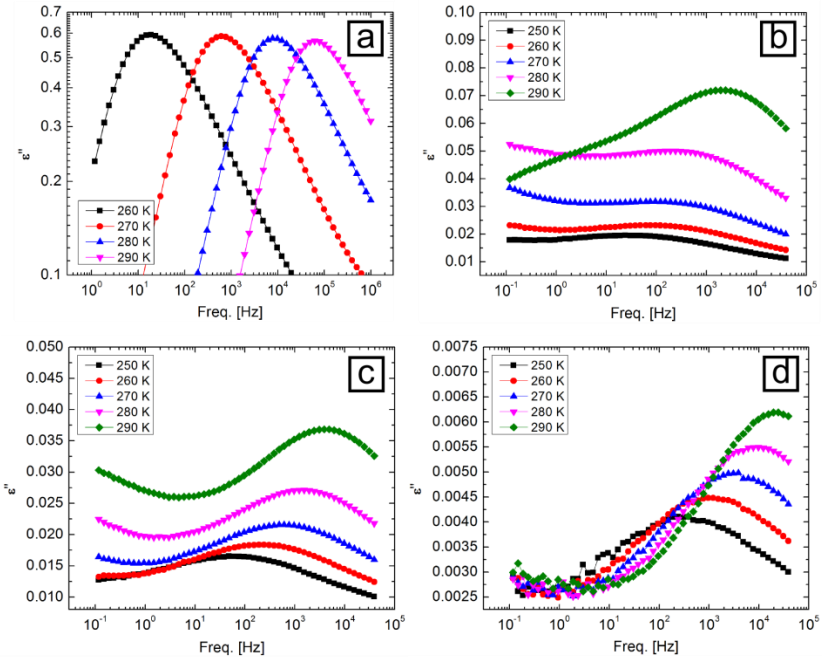

Figure 3.1 Raw BDS data of ε'' vs. the frequency of the applied ac voltage, at selected temperatures, for various bulk systems are plotted here: (a) pure PVME, and PVME/dPS4 blends, with weight fractions (a) 35/65, (b) 25/75 and (c) 5/95.

The results of this analysis, plotted in Figure 3.2 as the inverse relaxation time, or relaxation rate, $1/\tau$ versus $1/T$, show that in the case of pure PVME the temperature dependence of the α-relaxation is well described by the VFT relation, as is well-known for

any pure homopolymer. With regard to the blends, however, the temperature dependencies of the relaxations deviate from the VFT relation as the temperature decreases. At a sufficiently low temperature, particularly evident in the 35% and 25% blends, the temperature dependences become Arrhenius. Such a deviation in blends has been discussed previously [11, 81, 94]; this low-temperature Arrhenius relaxation is identified as the "α′-relaxation" by some researchers. It is believed that the α′-relaxation is indicative of the PVME-rich domains undergoing relaxations within the confines of the glassy dPS-rich domains. However, in the case of the 5% blend, only the α′-relaxation is observed. It is worth emphasizing here that the VFT behavior is quite evident at higher frequencies and temperatures [81]. We have not shown these high-temeprature and high-frequency data here because they are well-known, and this is not the main point of our work.

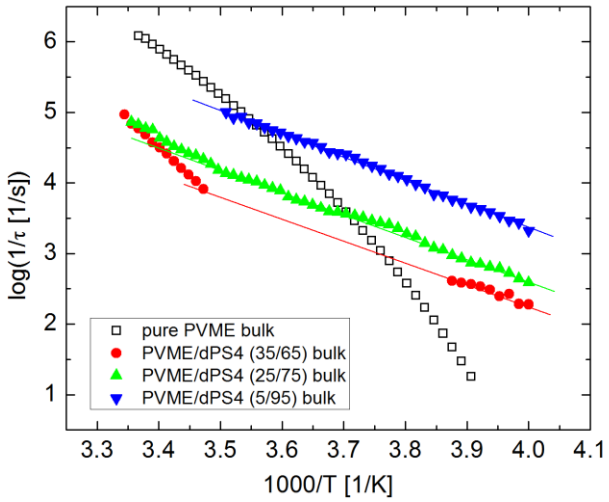

Figure 3.2 The temperature dependencies of the segmental relaxation times, τ, of PVME chains, in pure bulk PVME and in bulk blends of PVME/dPS4 are plotted here. These values of τ were extracted by fitting the curves that are plotted in Figure 3.1. The solid lines serve as eye guides indicating the α′-relaxation for the corresponding data sets. Our data are in agreement with the data reported previously in the literature.

Having discussed the frequency-sweep experiments and analysis, we note that an alternative representation of all our data would be with the use of a contour plot, where the

abscissa and ordinate are $1000/T$ and $\log(1/\tau)$, respectively; the values of $\log(\varepsilon'')$ are represented as contours of different colors. This contour plot is effectively a 3D plot of ε'' vs. T and $1/\tau$. It is noteworthy that the contour curves are sensitive to even weak relaxations, which are otherwise difficult to identify using a conventional 2D plot, i.e. "frequency sweep" at a given temperature or "temperature sweep" at a given frequency. Our analysis of the BDS data in this work will be based primarily on the contour plots, which provide significantly more insights into the connection between structure and dynamics of blends.

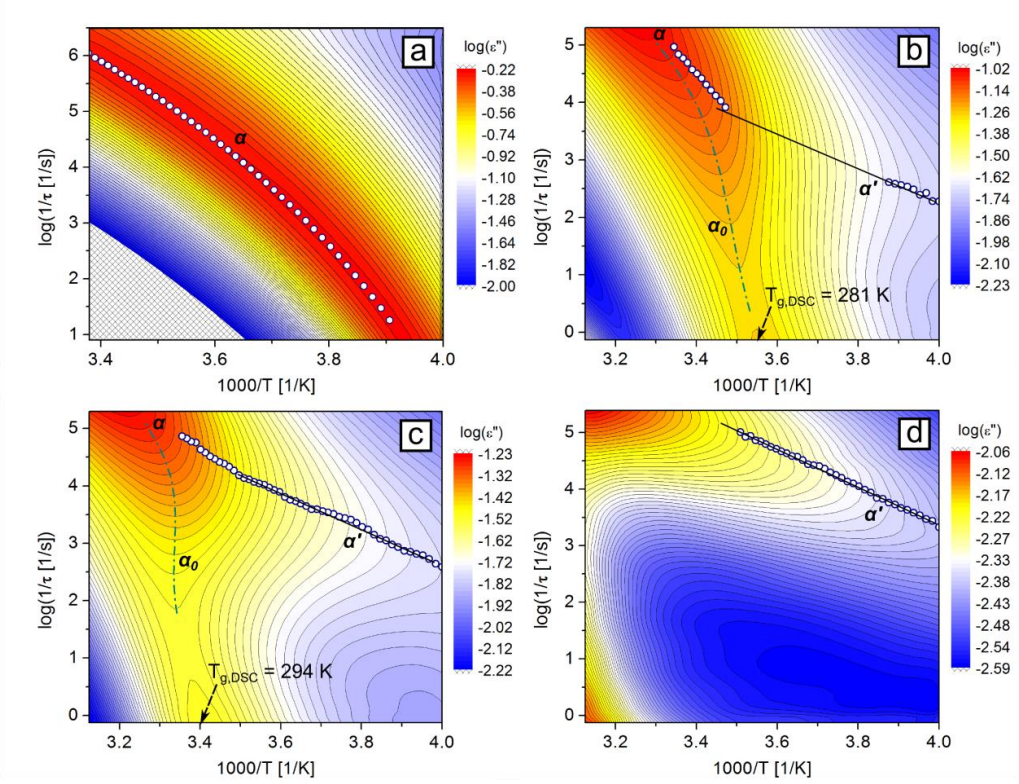

Figure 3.3 Raw BDS data (same data set as in Figure 3.1 of $\log(\varepsilon'')$ vs. the angular frequency of the applied ac voltage, $1/\tau$, and inverse temperature, $1000/T$, shown in a 3D contour plot, of the same systems as in Figure 3.2 are shown here for bulk samples. (a) PVME; (b)PVME/dPS4 (35/65) blend; (c) PVME/dPS4 (25/75) blend and (d) PVME/dPS4 (5/95) blend. The open circles are replotted from Figure 3.2. The solid lines in parts (b), (c) and (d) are guides to the eye and represent the α′-relaxation. The dash-dotted curves in (b) and (c) are also guides to the eye and represent the extra relaxation that does not appear in Figure 3.1. $T_{g,DSC}$ identifies the T_g of the blend measured using DSC.

The BDS data of PVME/dPS blends are now plotted as contour plots in Figure 3.3. Note here that the data in Figure 3.2 are overlaid on these plots and are represented by the open circles. The contours on these plots are substantially different for each composition. Note, nevertheless, that the relaxation processes shown in Figure 3.1 are observable in these plots. The breadths and temperature dependencies of the intensities are evident from the contour plots. A single α-relaxation (VFT temperature dependence) is represented in Figure 3.3a for the pure PVME sample. This will not be discussed further. Two relaxation processes, at temperatures below the high temperature α-process, are evident in Figures 3.3a and b, for the 35% and 25% blends, respectively. The faster relaxation process is characterized by a weaker temperature dependence than the VFT behavior and at sufficiently low temperatures becomes Arrhenius. The low-temperature Arrhenius temperature dependence has been identified at the α′-process, as described earlier. It is associated with the relaxation of PVME chains in PVME-rich domains confined by glassy dPS domains.

The second relaxation process, evident in the 35% and 25% blends, and labeled α_0 in the plots, is represented by the dash-dotted curves (guides to the eye) in Figures 3.3b and c, respectively. This α_0-relaxation process exhibits a much stronger dependence on temperature. The effect is more significant in the 25% than the 35% sample. We note that this relaxation is not due to impurities such as moisture; its strength and temperature dependence remain constant regardless of the length of annealing. This new α_0-relaxation is associated with the PVME chains relaxing in an environment of a different local composition from the former α′-process which persists at lower temperatures; the composition is richer in PS. Our data suggest that it "freezes" at a temperature in the vicinity of the blend T_g, measured using DSC, T_g(DSC). In light of the "freezing" of the local domains at a temperature close to this T_g, it may be surmised that the α_0-relaxation is associated with domains in the blend whose local PVME compositions are comparable to that of the average bulk value. It is noteworthy that for the blend containing only 5% PVME (Figure 3.3d) only the α′-relaxations are evident; this is consistent with the notion that the amount of PVME available in the blend is insufficient for the signal from the α_0-relaxation to be observable in the contour plot. We note here that the existence of these different dominant relaxation processes with very different temperature dependencies, and the compositional heterogeneities necessary for their existence, is an indication of the change in structure of the blend with decreasing temperature.

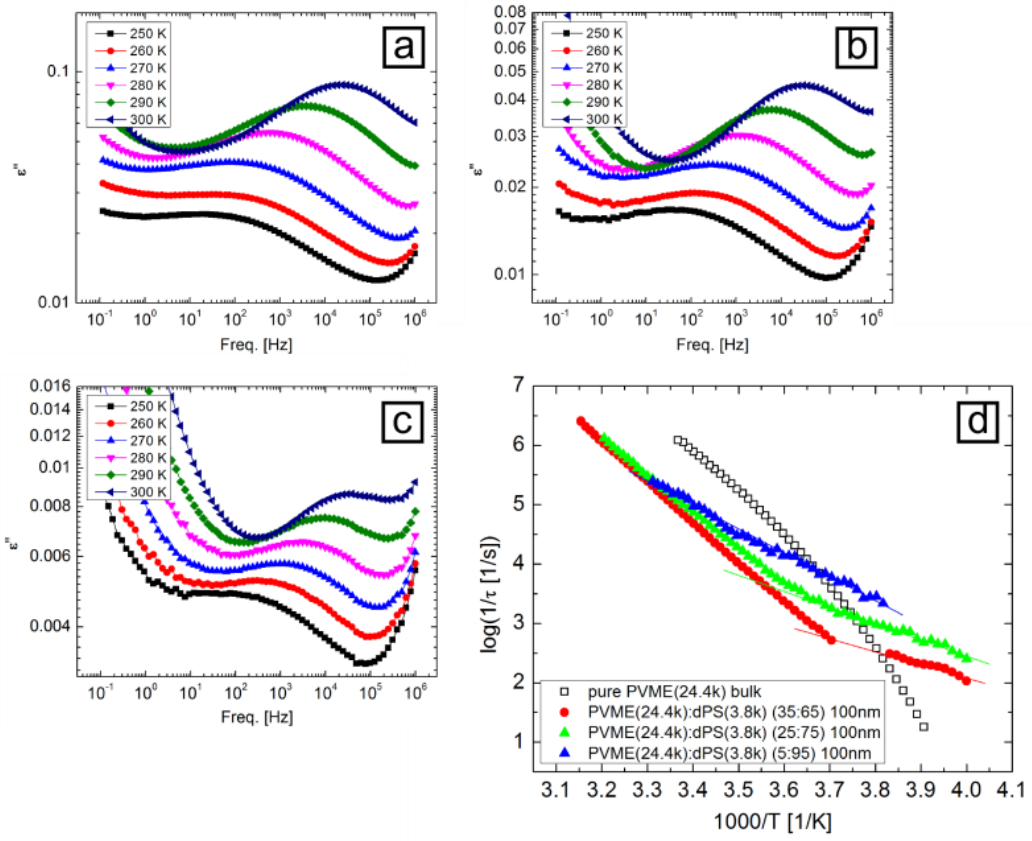

Figure 3.4 The conventional plots of ε'' vs. the frequency of the applied ac voltage for thin film PVME/dPS3.8 blends of thickness h=100 nm are shown in parts a, b and c. The segmental relaxation times, τ, extracted from these curves are plotted in part d, where the solid lines serve as eye guides indicating the α′-relaxation for the corresponding data sets.

Thus far, it should be evident that the contour plot provides more details about relaxation processes than a single frequency- or temperature-sweep analysis for polymer/polymer blends, in which dominant relaxation processes associated with distributions of relaxations occur. For the case of a homopolymer, the information that the contour plot provides about relaxation processes is identical to that from a frequency- or temperature-sweep experiment. A case in point is the contour analysis of neat PVME; this analysis provides the same information as the frequency-sweep analysis (Figure 3.3a). For a miscible polymer blend, such as PVME/PS, multiple local relaxations occur in proximity, and some of their distributions are convoluted, forming broad profiles. All the experimental

measurements were conducted at temperatures below the T_g of pure PS. The dynamics of the PVME chains in the mixtures are orders of magnitude faster than those of the PS component, due to their significantly lower T_g and lower friction factor. The ε'' intensities are strongly temperature dependent (Figure 3.3) because the dielectric response is strongly dependent on the local dynamics of the blend. At high temperatures, the dielectric response is strong because PVME and PS chains are all mobile, whereas the magnitude of the response diminishes as the local blend dynamics decrease with decreasing T and eventually vanishes when $T = T_g$(local). Therefore, the domains with lower T_g(local), or equivalently higher local PVME concentration, would have a higher intensity at a given T.

In other words, due to concentration fluctuations at a given T, the contributions to the dielectric response would come from all relaxations, with local regions of different T_gs throughout the sample. Consequently, in a frequency-sweep analysis at a certain T, a convolution of all such responses would favor those with faster dynamics and lower T_g(local) due to their higher intensities. Therefore, regardless of the relative intensities, the slower relaxation(s), if strongly temperature dependent, may be completely submerged in the low-frequency "tail" of the faster relaxation in the frequency-sweep plot such as those shown in Figure 3.1. Indeed, the contour plots shown in this study provide additional, more complete, information about relaxations in the blends than a single frequency or temperature-sweep analysis.

We now direct our attention to the thin film PVME/dPS blends. Data from the frequency-sweep experiments of the 100 nm thin films, containing 35%, 25% and 5% PVME, of blends of PVME/dPS3.8, are shown in Figures 3.4a-c; the temperature dependencies of the relaxation times are plotted in Figure 3.4d. The contour plots of the same data sets are shown in Figure 3.5; the curves from Figure 3.4d are overlaid. It is also observed in these films that the relaxation curves are broad and their intensities decrease dramatically with decreasing temperature. Notably, a new relaxation process, α_{int}, emerges. The curves drawn to represent α_0 and α_{int} in Figure 3.5 are guides to the eye. A quantitative analysis may not be performed at this time due to their low intensities and strong convolution with the strong signal of the α-relaxation. The α_{int}-relaxation is present in the 35%, 25%, and most likely also (considering its weak signal) in the 5% blends. This relaxation exhibits similar dynamics and temperature dependence regardless of PVME concentration, although its intensity is much stronger in the 35% and 25% blends than in the

5% blend. In contrast, the intensity of α_0-relaxation in the 35% blend is strong and its temperature dependence is also strong, compared to the 25% blend. There is no evidence of this relaxation in the 5% blend. Both α_0 and α_{int} processes merge with the α-relaxation at high temperatures, as suggested by the data, as expected.

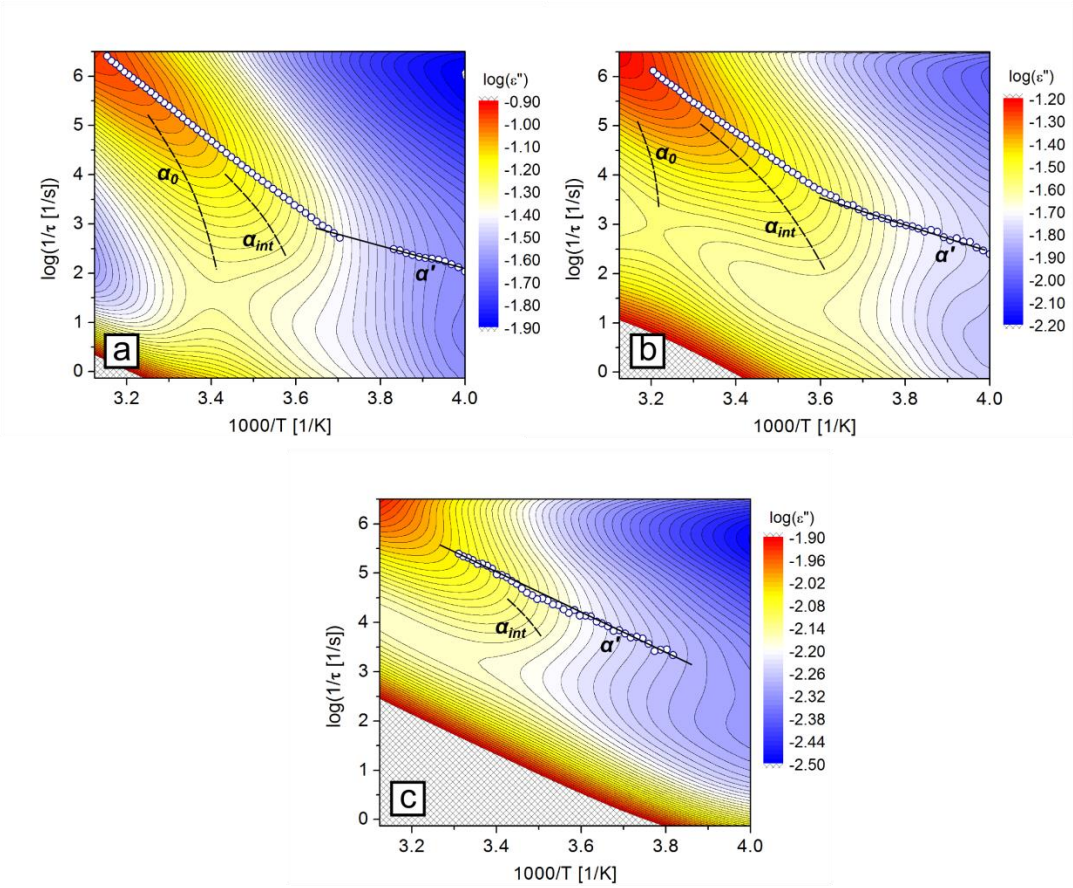

Figure 3.5 The contour plots of the 100 nm thin film blends of PVME/dPS3.8, with weight fractions (a) 35/65, (b) 25/75 and (c) 5/95. The open circles are reprinted from Figure 4d; its α' part is eye-guided by the solid line. The relaxations α_{int} and α_0 represented by the dashed curves are guides to the eye.

In these thin film mixtures, the PVME chains are distributed within the interior and at the interfaces. The appearance of the α_{int}-relaxations would be associated with the

presence, due to preferential segregation, of PVME to the Al interfaces, from the blend [96, 101-102]. The DSIMS profile in Figure 3.6, for a 100 nm thick PVME/dPS3.8 mixture, reveals the preferential segregation of PVME. The free energy of the system is minimized with the interfacial segregation of PVME, and the extent of segregation depends, in part, on the polymer/substrate interactions relative to the entropic and enthalpic interactions in the interior. We note that as the overall weight fraction of PVME increases in the film from 25% to 35%, the amount of PVME interfacial segregation increases; this increase is manifested in an increase in the intensity of α_{int}. This interfacial layer necessarily has a high concentration of PVME, consistent with the faster dynamics, compared to PVME chains responsible for the α_0-relaxations within the interior of the film. When the overall composition of PVME is low, PVME chains segregate preferentially at the polymer/Al interfaces, and there is minimal PVME in the film interior; under these conditions the intensity associated with α_{int} is comparatively larger. Our observations based on the BDS data are entirely consistent with compositional analysis of the thin film blend system.

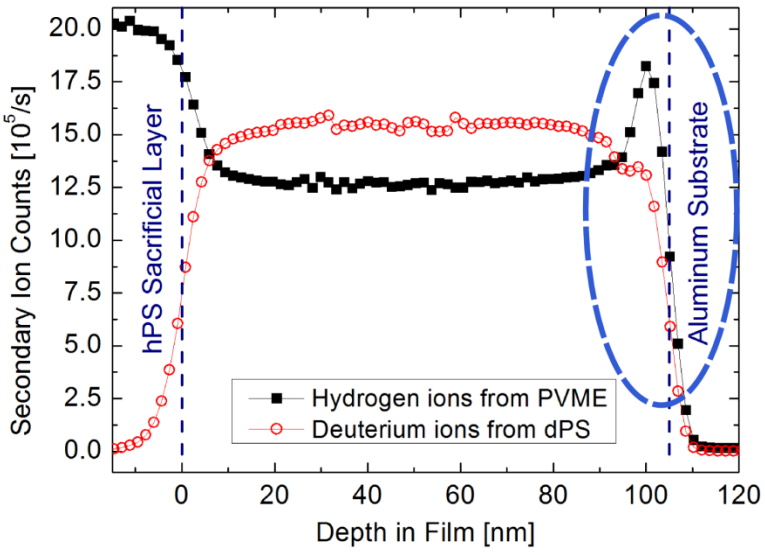

Figure 3.6 The depth profiles of PVME (indicated by hydrogen) and dPS3.8 (indicated by deuterium) in the 105 nm blend of the 25% blend of PVME/dPS3.8, measured by DSIMS. The profiles show a segregated PVME-rich layer at the Al/polymer interface. The dashed circle highlights the interfacial segregation.

In light of the foregoing observations, we propose the following picture for the structure and dynamics of the blends. The composition is heterogeneous, varying spatially and temporally. The composition fluctuates locally from values of φ_{self} to φ_{eff}, where $\varphi_{eff} = \varphi_{self} + \varphi_{fluc}$, and φ_{fluc} is due to contributions from concentration and density fluctuations. At high temperatures where the dynamics of the phases are rapid and the PVME chains sample the same average environment over the appropriate time scales, the behavior is VFT-like. However, with decreasing temperature, the strong fluctuations lead to distinctly different domains, characterized by locally different average compositions, and two dominant relaxation processes are evident. Domains with sufficiently low concentrations of PVME undergo a glass transition along with PS chains and exhibit a temperature dependence that is strong compared to VFT behavior (the α_0-process). The disappearance of this α_0-process at approximately the Tg measured by DSC of the blend (T_g(DSC), identified in Figures 3.3b and c) is associated with the formation of glassy PVME/PS domains. PVME chains within domains, at larger concentrations, responsible for the other dominant relaxation process, exhibit Arrhenius temperature-dependent relaxations within the confines of glassy PS phases, at sufficiently lower T; this is the α'-relaxation. In thin films, the PVME chains segregate to the Al interfaces and form a separate phase; the emergence of the α_{int}-relaxation process is a manifestation of this phenomenon.

3.4 Conclusion

We demonstrated that the dynamics of the PVME component of miscible polymer blends of PVME and PS manifest the existence of spatially and temporally compositional heterogeneous environments. At high temperatures, where the chains experience the same average compositional environment, the temperature dependence of the PVME component dynamics is VFT-like (α-process). At lower temperatures the dominant relaxations of the PVME component manifest the existence of PVME chains in relaxing two local environments whose average compositions are very different. One relaxation process is associated with PVME chains in an environment of higher PS concentration (the minimum PVME local concentration is set by φ_{self}); this process, which we denote as the α_0-process, exhibits a strong dependence on temperature than the α-process. This region of PVME/PS chains evidently undergoes a glass transition in the vicinity of the T_g measured by DSC of

the blend. The other dominant relaxation process exhibits a weaker dependence on temperature than the α-relaxation, and at sufficiently low temperatures its temperature dependence becomes Arrhenius (α′-relaxation). In thin films confined between "walls," onto which the PVME chains preferentially segregate, a new relaxation process, α_{int}-process, emerges. The relative intensities of the α_0- and α_{int}-relaxation peaks are indicative of the extent of interfacial segregation.

It would be fascinating for a series of computer simulations to be developed to understand this process in mixtures with such a heterogeneous structure with populations of chains relaxing in different compositional environments at different temperatures. Such simulations would provide much more quantitative study and new insight into the unusual temperature dependencies reported here.

CHAPTER 4

OUT-OF-PLANE CHARGE TRANSPORT IN CONJUGATED POLYMER THIN FILMS

This chapter is based on the following published article (with permission from the American Chemical Society):

- **H. Yang**, E. Glynos, B. Huang and P.F. Green. Out-of-plane carrier transport in conjugated polymer thin films: role of morphology. *Journal of Physical Chemistry C*, 2013, *117* (19), 9590-9597.

4.1 Introduction

Transport processes in conjugated polymers are of significant interest due largely to organic electronic applications [103-104] that include polymer light-emitting diodes and organic solar cells [16, 105-108]. While established techniques such as the time-of-flight (ToF) [109-111], space-charge limited current (SCLC) [112-115], and the method of charge extraction by linearly increasing voltage (CELIV) [116-118] have extensively been applied to measure the carrier mobility, μ, in conjugated polymer thin films in the out-of-plane direction, information regarding carrier densities n and conductivities σ_{dc} are not accessible from these measurements. Moreover, while numerous investigations of carrier transport have been investigated in conjugated polymer thin films, particularly in poly(3-hexylthiophene) (P3HT), the vast majority of studies have investigated the in-plane mobilities only, using field effect transistor configurations [119-121]. There nevertheless remain unanswered questions, such as the role of morphology and film thickness on carrier transport [120-121].

The technique of impedance (dielectric) spectroscopy (IS), a well-established and powerful method for measuring the electrical properties of condensed matter [18], can provide information about n and σ_{dc}, which are otherwise difficult to obtain simultaneously in conjugated polymers, particularly in the out-of-plane direction. Although much work has been reported on conductive thin films of ionomers and ionic liquids [122-124], studies on conjugated polymer thin films are rare. The experimental challenges have been the low carrier densities and, more specifically to IS measurements, electrode polarization effects that pose challenges for appropriate assessment of the experimental data. In this work we show how IS may be used to determine the out-of-plane μ, σ_{dc} and n simultaneously in a neat P3HT film. The IS, ToF, and CELIV results reveal that the hole mobilities increase by an order of magnitude with increasing film thickness, over a range of thicknesses from h = 100 to 700 nm; beyond this thickness, μ becomes constant. This thickness dependence of mobility is due to the fact that the substrate induces a high degree of order into the organization of the chains; with increasing distance away from the substrate the extent of order decreases, as discussed in a recent paper from our group [125]. It is noteworthy, in this work, that n and σ_{dc} do not track the mobilities; instead, n and σ_{dc} exhibit significant decreases over the same thickness range before becoming constant for h > 700 nm. These trends in μ, n and σ_{dc} reconciled in terms of changes in the crystal orientation and structural anisotropy with increasing film thickness in this system.

A primary physical quantity measured using IS is the complex ac conductivity $\sigma^*(\omega) = \sigma'(\omega) + i\sigma''(\omega)$, where σ' and σ'' are the real and imaginary parts of the complex conductivity, i is the imaginary unit, and ω is the angular frequency of the ac voltage applied across the film. It is well understood, theoretically, that the σ' spectrum has two primary contributions: one associated with the long-range carrier dynamics and the other associated with the short-range local dynamics [124, 126-128]. The σ' spectra for P3HT of four thicknesses (24.9 μm, 4.4 μm, 550 nm, and 95.5 nm) are shown in Figure 4.1a. The plateau regime, associated with the long-range carrier dynamics, and the higher-frequency increase, due to the short-range local dynamics, are clearly apparent in the data for the thickest film, h = 24.9 μm. However, σ' decreases dramatically with decreasing frequency in the low-frequency regime (Figure 4.1a); this is due to the so-called "electrode polarization" effect [17-18, 124], associated with the accumulation of charges at the electrodes, which opposes the field that drives the charges across the film. At low frequencies, the charge carriers travel across the entire film and

accumulate at the electrodes, creating a gradient of charge across the film; this accumulation continues until the gradient completely cancels the external electric field, which drives the charge carriers toward the electrodes. When this process stabilizes, the separation of positive and negative charges leads effectively to the formation of a macroscopic dipole; this gives rise to an additional polarization. The onset of the electrode polarization, determined by the time required for the charge carriers to travel across the entire film, has been shown to be a function of the film thickness [124].

For sufficiently thick films, where the onset of the electrode polarization is many orders of magnitude away from the high-frequency limit of the conductivity plateau, the value of the σ' in the plateau regime is typically identified to be the dc conductivity, σ_{dc} [122-124, 126-127, 129-130]. However, for thinner films, the electrode polarization extends to higher frequencies, closer to the high-frequency increase of the bulk regime. Consequently, the plateau in the spectrum becomes narrower and less distinct, such as the h = 95.5 nm one whose data are plotted in Figure 4.1a; in sufficiently thin films, this plateau would eventually disappear. Subsequently, because the responses of the different regimes are strongly coupled in sufficiently thin films, it is impossible to extract σ_{dc} via inspection of the data. This has been one of the challenges with the application of this technique to measure transport processes in thin conjugated polymer films. So clearly the development of the reliable analysis of the entire spectrum, which enables the conductivities and carrier mobilities to be reliably extracted, is essential in order to study carrier transport in conjugated polymer films using IS. This would also make it possible to study out-of-plane carrier transport in films in the thickness range of 100-200 nm, thicknesses that are mainly used in organic-based devices, such as solar cells.

In this work, we show how the electrode polarization and the bulk regime may be analyzed using an equivalent circuit model to enable extraction of information about σ_{dc}, μ, and n. Measurements of μ, using ToF and CELIV measurements, are in excellent agreement with values extracted using IS. Both σ_{dc} and n are shown to decrease appreciably with increasing h. The thickness-dependent trends in μ, σ_{dc}, and n are consistent with changes in the morphology of these films. Conductive atomic force microscopy (CAFM) provided corroborating information, showing an appreciable dependence of carrier transport on the morphology of P3HT.

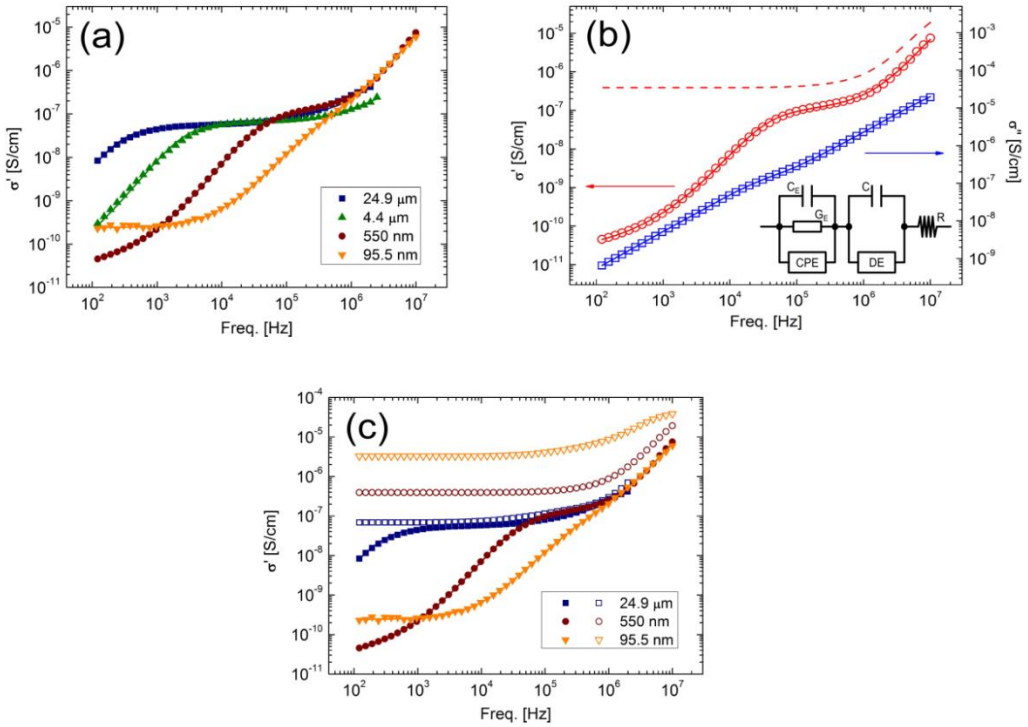

Figure 4.1 (a) The real part of σ' vs. the frequency of the applied ac voltage for P3HT films of thicknesses 24.9 μm, 4.4 μm, 550 nm and 95.5 nm, with the corresponding solid curves the fitted curves for each thickness. (b) σ' and σ'' spectra of the 550 nm P3HT film, with the corresponding solid curves indicating the fitted curves using the equivalent circuit shown in the inset. The dashed line shows the σ' curve of the P3HT layer only, excluding the effect of the electrodes. (c) The filled symbols are the measured σ' vs. the frequency of the applied ac voltage for P3HT films of thicknesses 24.9 μm, 550 nm and 95.5 nm, and the corresponding open symbols in the same shapes are the spectra after removing the electrode polarization.

4.2 Experimental Section

4.2.1 Sample Preparation

The 150 nm indium tin oxide (ITO)-coated glass substrates (Delta Technologies) were used as the substrates of the samples. The substrate was first sonicated in acetone and

isopropanol for 10 min each and ultraviolet cleaned for another 10 min. It was then immediately transferred into a glovebox under nitrogen atmosphere, where the rest of the fabrication was carried out. A ~60 nm layer of poly(3,4-ethylene dioxythiophene)/ poly(styrene sulfonate) (PEDOT:PSS; H.C. Starck Clevios PH500) was first spincoated on ITO, followed by annealing at 150 °C on a hot plate for 15 min. P3HT (~95% regioregularity, 50,000 g/mol, Rieke Metals, Inc.) was then spincoated or dropcast (if samples thicker than 1 μm were desired) on top and annealed afterward at 150 °C for 15 min before transferred to the deposition chamber to have the top electrode deposited. The top electrode, consisting of a 2 nm lithium fluoride (LiF, as a hole injection blocking layer for CELIV measurement) and aluminum (Al) further on top, was thermal evaporated through a shadow mask at 0.1 and 2 Å/s, respectively, at a typical pressure of ~10^{-7} torr. The Al electrode thickness for CELIV measurements is 100 nm, while that for ToF is 20 nm. The thickness of the spincoated films were obtained by ellipsometry measurement of the corresponding films prepared on roughened glass substrates, while the thicknesses of the dropcast films were measured using profilometry. The samples measured using all three techniques (IS, CELIV and ToF) share the same structure in order to have decent comparison of their results, although LiF layer is not required in IS measurement.

4.2.2 Impedance Spectroscopy (IS) measurement

The IS measurement was performed using a broadband dielectric spectrometer (BDS, Novocontrol Technologies GmbH) with a sharp brass tip (upper electrode of BDS) penetrating the film and conducting the bottom ITO and a supporting brass plate (lower electrode of BDS) conducting the top electrode of the sample through a piece of gold wire. The measurement was performed at 25 °C, with the application of an ac voltage of 0.05 V and frequency range spanning between 100 Hz and 10 MHz. No dc bias was applied to the films. Complex impedances were measured and the complex conductivity and permittivity may then be extracted for further analysis.

4.2.3 Time-of-Flight (ToF) Measurement

The ToF measurement setup is the same as in the literature [131]. A nitrogen laser (Newport VSL337, λ = 337.1 nm, intensity per pulse about 120 μJ, pulse width <4 ns) was incident through the semitransparent Al electrode to photoexcite the P3HT layer and

generate a sheet of charge carriers. A Sorensen XHR300 dc power supply was used to apply constant dc bias over devices. The current transients were then amplified by a FEMTO DLPCA-200 low noise current amplifier and recoreded by a Tektronix TDS 3052C digital oscilloscope. The measurement was conducted in the air. For data analysis, the transit time t_{tr} was estimated from the intersection point at which the two asymptotes to the log-log plot (pre- and post-knee) cross. The mobility μ is determined by $\mu = h^2/Vt_{tr}$, where h is the thickness of the neat P3HT film and V is the applied voltage.

4.2.4 Charge Extraction by Linearly Increasing Voltage (CELIV) Measurement

The CELIV measurement setup is described as follows. A BK Precision 4075 function generator applied increasing voltage to the devices to extract current transients. The current transients were then amplified by the same amplifier and recorded by the same digital oscilloscope as the ToF measurement. The measurement was performed in a cryostat (Janis VPF100) which provides vacuum of approximately 1 mtorr and a wide temperature range. For data analysis, time t_{max} at which the current reaches maximum, displacement current $j(0)$ and the current difference Δj between maximum current and $j(0)$ were measured directly from the raw data. The mobility μ is then calculated by [117]

$$\mu = \frac{2h^2}{3At_{max}(1 + 0.36\Delta j/j(0))}$$

where h is the film thickness and A is the voltage ramping rate.

4.2.5 Conductive Atomic Force Microscopy (CAFM) Measurement

The structure of the samples for CAFM is the same as those for IS, CELIV, and ToF measurements, except that they do not have the top electrode. CAFM measurements were performed under ambient conditions using Asylum Research MFP-3D. A Pt/Ir5-coated contact-mode AFM probe (NanoWorld, CONTPt, spring constant 0.2 N/m) was used as the top contact for all measurements, tracking topography and dark current measurement simultaneously. Note that with regard to these AFM measurements, a hole-only device (measuring predominantly the hole current) is created due to the high work function of both the ITO/PEDOT:PSS bottom electrode and Pt/Ir5 conductive cantilever AFM tip where we could map the hole conduction network.

4.3 Model and Fitting Procedure

We resolve the coupling problem in the σ' spectra of the electrode polarization and the bulk regime by fitting the data using the appropriate equivalent circuit model based on the theoretical work developed in the literature [18, 132-134]. Shown in the inset of Figure 1b, it contains two circuit blocks and a resistor in series. The block representing the conductive film is composed of a distributed element (DE) and a capacitor C in parallel. Here, DE is defined by a Fourier transform of the Kohlrausch-Williams-Watts stretched exponential model, and the capacitor C accounts for the dielectric behavior of the conductive layer [133-134]. The contribution of the electrode layer, on the left-hand side of the conductive block, is modeled using a constant phase element (CPE), a capacitor (C_E) and a conductor (G_E) in parallel [18, 132]. As an equivalent circuit, a different appearance of the combination of circuit elements may serve the same purpose as long as they are electrically equivalent; in our analysis, the model described above is selected in such a way so that it can be analyzed and fitted, which is explained in the following paragraph. Lastly, a resistor R in series with the P3HT block and the electrode block is used here to represent the contact resistance of the electrode. The circuit we used may look slightly more complicated compared to some other models in the literature, as our model deals with the strong coupling between the bulk regime and the electrode polarization; the fundamental physical idea of the equivalent circuit remains unchanged.

With the equivalent circuit model described above, the data of σ' and σ'' versus ω collected from the IS measurements were analyzed using LEVM [135], a computer program developed by J. Ross Macdonald [18]. LEVM uses the so-called Complex Nonlinear Least Square method [136] to fit both real and imaginary parts of the complex physical quantities (impedance, admittance, modulus, and permittivity) at the same time. For our analysis using LEVM, the "Circuit O" model in the software was used and modified to accurately describe our aforementioned model. The impedances of the elements DE and CPE are given the following form in LEVM [18]:

$$Z^*_{DE} = R_{DE}\mathbf{F}\{\exp[-(t/\tau)^{\beta}]\},\ Z^*_{CPE} = (A(i\omega)^{\gamma})^{-1}$$

where R_{DE}, τ, A, and γ are fitting parameters, and $\mathbf{F}\{\}$ denotes the Fourier transform from time domain to frequency domain. The stretching parameter β is set to 1/3, which has been

reported to be the most appropriate fit that yields the best results [17]. Therefore, there are in total eight parameters (R_{DE}, τ, C, A, γ, C_E, G_E, and R) to fit in this model. Despite the large number of fitting parameters, it is important to emphasize that they may all be fitted consistently; they all have their unique physical meanings (as explained above) and may not be substituted by other parameters. It has been tested that the model was not able to fit the spectra with the absence of any one of the eight parameters.

The parameters extracted from the data of an h = 550 nm thick P3HT film are plotted in Figure 4.1b, where σ' and σ'' are shown together with the corresponding fitting curves. The agreement between the measured spectra and the calculated curves is excellent. Because it is the electrode block in the equivalent circuit that accounts for the electrode polarization, by removing the electrode block (and hence the electrode polarization) from the circuit, the conductivity spectrum of the P3HT layer may therefore be determined (cf. the dashed curve in Figure 4.1b and c). The value of the low-frequency plateau of this curve, computed from the raw data, denotes σ_{dc} of the P3HT layer.

Having determined σ_{dc}, the carrier density n and mobility μ of the film may be calculated. Methods of obtaining carrier concentration have been shown by applying dc bias to the sample (e.g. ref [137]), but they may not be implemented in our case, as only a small ac voltage, instead of dc bias, was applied. Klein et al. [122], on the other hand, developed a method to calculate μ based on the locations of the peaks in the spectra of the imaginary part of the permittivity (ε'') and the ratio $\varepsilon''/\varepsilon'$, where ε' is the real part of the permittivity. Their method, however, is not appropriate for P3HT films, because some of their assumptions are violated [122]. Therefore, we applied the model developed by Schütt and Gerdes [138-139] for singly charged materials here. In this model it is assumed that the electrode polarization, or space-charge effect, dominates the ε' response of the thin film. Hence, ε' may be written in the form of a Debye relaxation [138-139]

$$\varepsilon' = \varepsilon'_S\left(1 + \frac{\delta}{1 + (\omega\tau_D)^2}\right) \text{ with } \tau_D = \tau\delta, \text{ where } \delta = \frac{h}{\sqrt{D\tau}} \text{ and } \tau = \frac{\varepsilon'_S\varepsilon_0}{\sigma_{dc}}.$$

Here, ε'_S represents the real permittivity at low-frequency limit, d is the film thickness, D is the diffusion coefficient, and τ is called the electrical relaxation time. Recalling the Nernst-Einstein relation $D = \mu kT/e$, where μ, k, T, and e stand for charge carrier mobility, Boltzmann constant, temperature in Kelvin, and unit charge, respectively, and given X and

ω_X chosen in the electrode polarization region so that $\varepsilon'(\omega_X) = X\varepsilon'_S$ and $1 + (\omega_X\tau\delta)^2 \approx (\omega_X\tau\delta)^2$ (i.e. $\omega_X \gg (\tau\delta)^{-1}$), we obtain the charge carrier density n and mobility μ [138-139]

$$n = \left(\frac{\sigma_{dc}}{\sqrt{X-1}\varepsilon'_S\varepsilon_0\omega_X}\right)^4 \frac{\varepsilon'_S\varepsilon_0 kT}{e^2 d^2}, \quad \mu = \frac{\sigma_{dc}}{ne}.$$

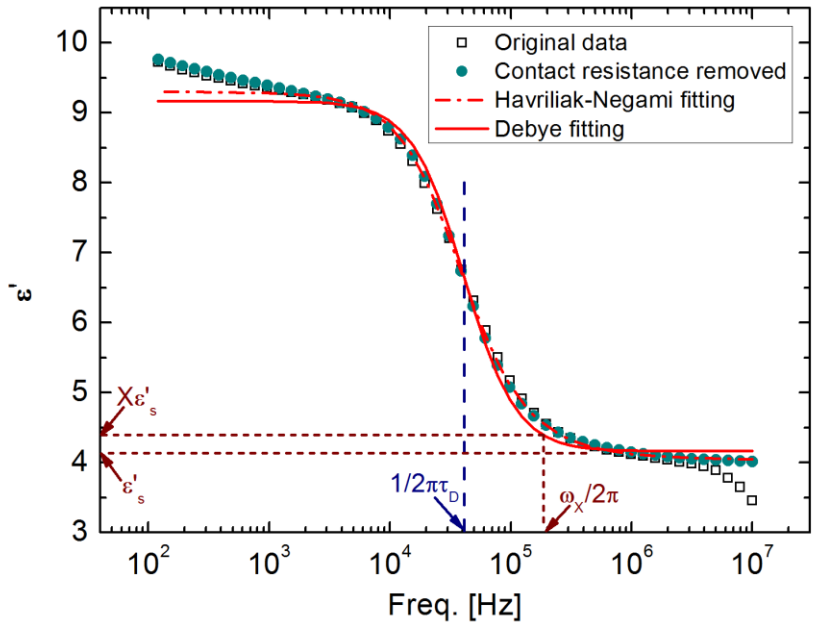

Figure 4.2 The frequency dependence of the real part of the permittivities and their fitting curves. Open squares represent the original measured data; having the contact resistance (element *R* in the inset of Figure 4.1a) removed after the equivalent circuit fitting, the data change to what is shown with the solid circles. The data can thus be fitted using the Havriliak-Negami (dash-dotted curve) or Debye (solid curve) function, and the charge carrier (hole) mobility may be further calculated using the Schütt-Gerdes model.

As of the measured data rather than the ideal case, the parameters used in the equation above were obtained following the analysis procedure below. Here we take the data of the 550 nm P3HT film as an example, whose data points and the fitting curves are shown in Figure 4.2. The original spectrum of ε', represented by the open squares, has a significant

decrease when approaching the high-frequency limit. This decrease results from the contact resistance represented by the resistor R in the equivalent circuit shown in the inset of Figure 4.1b. After fitting the spectrum, we are able to recover the entire spectrum without the influence from resistor R, showing with the solid circles, where the ε' drop at high frequencies is eliminated. The charge transport information lies in the step-like decrease in the ε' spectrum; this feature may always be fitted using the empirical Havriliak-Negami function (dash-dotted curve), but deviation may occur when fitted using the Debye function (solid curve), especially for thinner films. It is believed [138-139] that the deviation of the measured data from the Debye function is due to the roughness and pores at the conductive film/electrode interface, which violates the planar-interface assumption of the model. Hence, in spite of the deviation, Debye function was still applied to calculate ε'_S and τ_D ($=\tau\delta$). To ensure the validity of the assumption $1 + (\omega_X\tau\delta)^2 \approx (\omega_X\tau\delta)^2$, we may choose any value for ω_X as long as $\omega_X \gg \tau_D^{-1}$ holds and, thus, $X = \varepsilon'(\omega_X)/\varepsilon'_S$. At this point, we are able to reconcile $\sigma_{dc} = \varepsilon'_S\varepsilon_0/\tau$ with the one obtained directly from the conductivity spectrum, indicating that the fitting and the Schütt-Gerdes model applied here are self-consistent. The charge carrier density and mobility may then be determined from the equations above.

4.4 Results and Discussion

To establish the viability of this technique, the mobilities of P3HT films with various thicknesses h were measured and compared with those measured using the techniques of CELIV and ToF (Figures 4.3a and b). Figure 4.3a shows that for thick films (from $h \sim 700$ nm up to $h = 25$ μm) mobilities measured using the three techniques are in excellent agreement; the hole mobilities in the P3HT thick films remain constant, within experimental error, at $\sim 8.0 \times 10^{-4}$ cm^2/V·s for all thicknesses. IS measurements of thin films reveal that the hole mobility in P3HT thin films increases with increasing h and saturates for $h > 700$ nm, which is in excellent agreement with the CELIV studies (Figure 3b).

IS is a straightforward and powerful technique to measure the out-of-plane σ_{dc} of conjugated polymer films. Its primary advantage over ToF and CELIV is that σ_{dc} and n, apart from μ, may also be obtained. The thickness dependence of σ_{dc} and n of the P3HT films is plotted in Figures 4.3c and d. Interestingly, while out-of-plane μ increased with increasing h, before reaching a plateau for h > 700 nm, σ_{dc} and n exhibited the opposite trend. This is the

first time, to the best of our knowledge, that the thickness dependence of the out-of-plane σ_{dc} and n were measured in P3HT films.

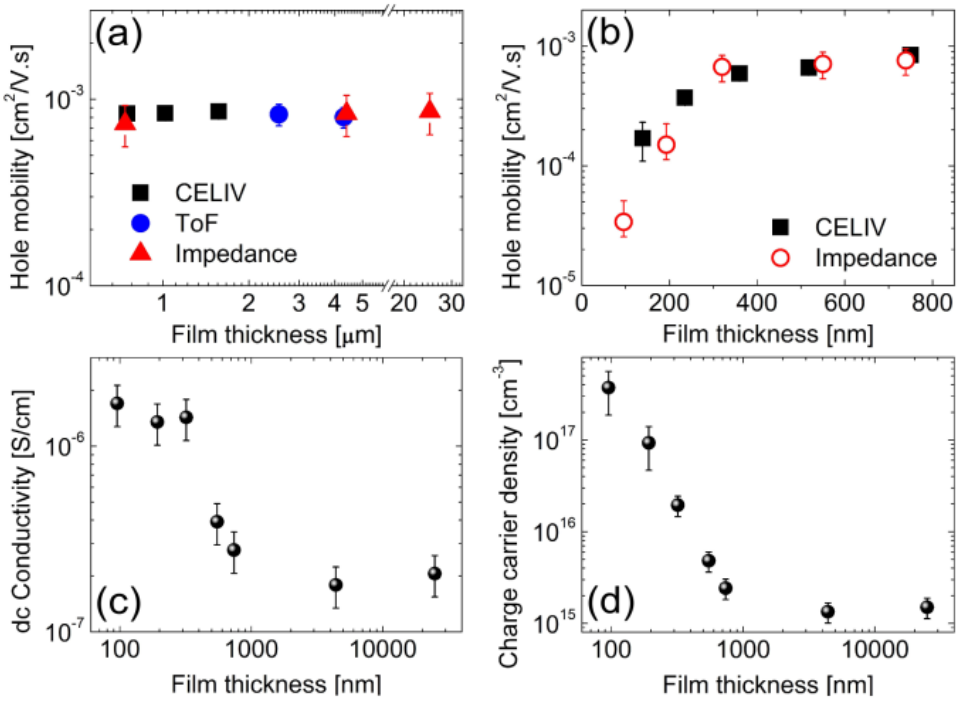

Figure 4.3 Hole mobilities of (a) thick and (b) thin films of P3HT measured using CELIV, ToF and IS, as well as the film thickness dependence of (c) the dc conductivity and (d) the charge carrier (hole) density of the P3HT films.

The increase of out-of-plane μ with increasing h is associated with the change in morphology with increasing distance from the substrate. As reported in the literature [140], there exists a substrate-induced orientation of the crystalline morphology, where an "edge-on" orientation exists at this substrate; this orientation favors slower out-of-plane μ [125]. Specifically, given such "edge-on" orientation, the backbones of this planar molecule form layers with the π-π coupling direction in a plane parallel to the substrate. As a result, transport along the in-plane direction is approximately 2 orders of magnitude faster than transport in the out-of-plane direction [16, 141-142]. With increasing distance away from the

substrate, the fraction of the effective "face-on" orientation, whose π-π coupling direction is normal to the substrate, increases, leading to an increased out-of-plane μ; for sufficiently thick films the structure becomes isotropic and μ exhibits a plateau, independent of the film thickness. With the decrease of the fraction of "edge-on" oriented crystals, reduction in the size of the crystals with increasing thickness and the formation of an isotropic morphology, the structural defect concentration increases; this very likely results in an enhancement in the charge trapping and relaxation and thus a decrease in n and, accordingly, σ_{dc}. Clearly, that μ follows the opposite trend to σ_{dc} and n with increasing film thickness is associated with holes in the morphological structures of these conjugated polymer films. We note that, in P3HT, electron transport is strongly affected by trapping due to the presence of molecular oxygen in the sample; in fact, ToF measurements show strong evidence of dispersion in the electron transport (but not hole transport), which is consistent with trapping of the electrons [143-144].

Having established the viability of the IS technique to measure carrier mobilities, conductivities and carrier densities in organics, we provide a further example of the role of the morphological structure of the film on carrier transport. To this end, hole mobility measurements were performed on samples prepared using solutions that had been aged for a month. Semicrystalline conjugated polymers exhibit a tendency to self-assemble while in concentrated solution, when the solution is left undisturbed (aged) for a period of time [141-142, 145-148]. Here P3HT chains, specifically known to exhibit π-π stacking in solution under these conditions, form fibrils that are micrometers in length [141, 145, 147]. Samples examined in the experiments discussed above were prepared using fresh solutions and do not possess this fibril structure.

Figure 4.4 shows the AFM deflection images of ~700 nm P3HT films that were spincoated from a one-month-old solution (Figure 4.4a) and from a freshly prepared solution of almost the same thickness (Figure 4.4c). Long fibrils, micrometers in length, are evident in the film prepared from the aged solution, whereas there is no evidence, as expected, of fibril formation in the film prepared in a freshly made solution. The existence of the fibrils is clear evidence of local self-organizational structure along a preferred direction; the polymer chains are π-π stacked along the longitudinal axes of the fibrils; a schematic of the fibril structure is shown in Figure 4.5a [141-142]. In addition, because in these submicrometer films it is reasonable to believe that the longitudinal axes of the fibrils are

oriented parallel to the substrate, the orientation of the P3HT crystalline phase is "edge-on." This was also confirmed in our laboratory from grazing-incidence X-ray diffraction (XRD) measurements (using a Bruker D8 analytical X-ray system in a grazing-incidence geometry) of these films. The data in Figure 4.5b reveal a significant increase, nearly twice, in the intensity corresponding to the (100) P3HT crystals "edge-on" orientation, for the samples with fibrils, compared to the one without fibrils.

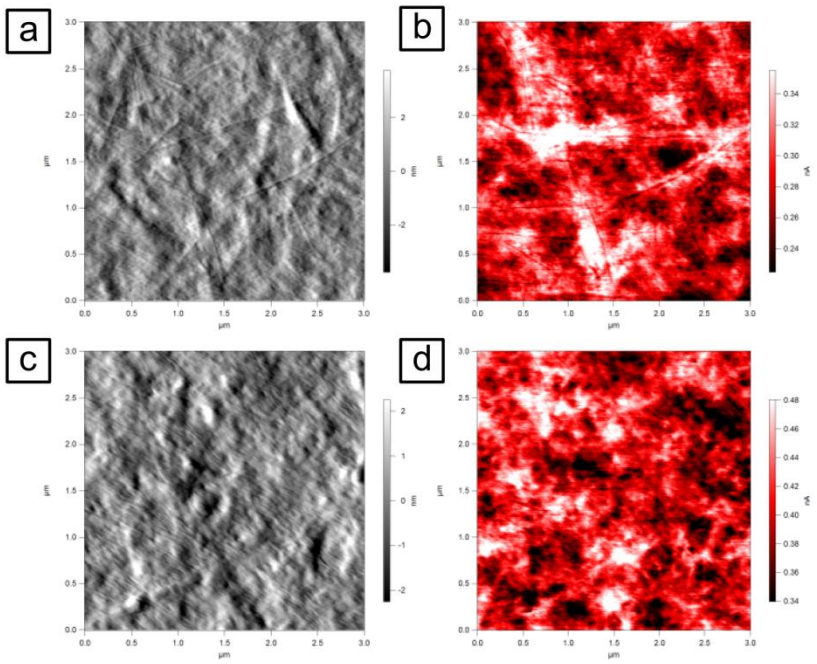

Figure 4.4 The 512px × 512px AFM images of a 5µm × 5µm square region of the ~700 nm P3HT film: (a) the deflection map and (b) the current intensity map of the film spincoated using one-month-old solution, and (c) the deflection map and (d) the current intensity map of the film spincoated using freshly-made solution.

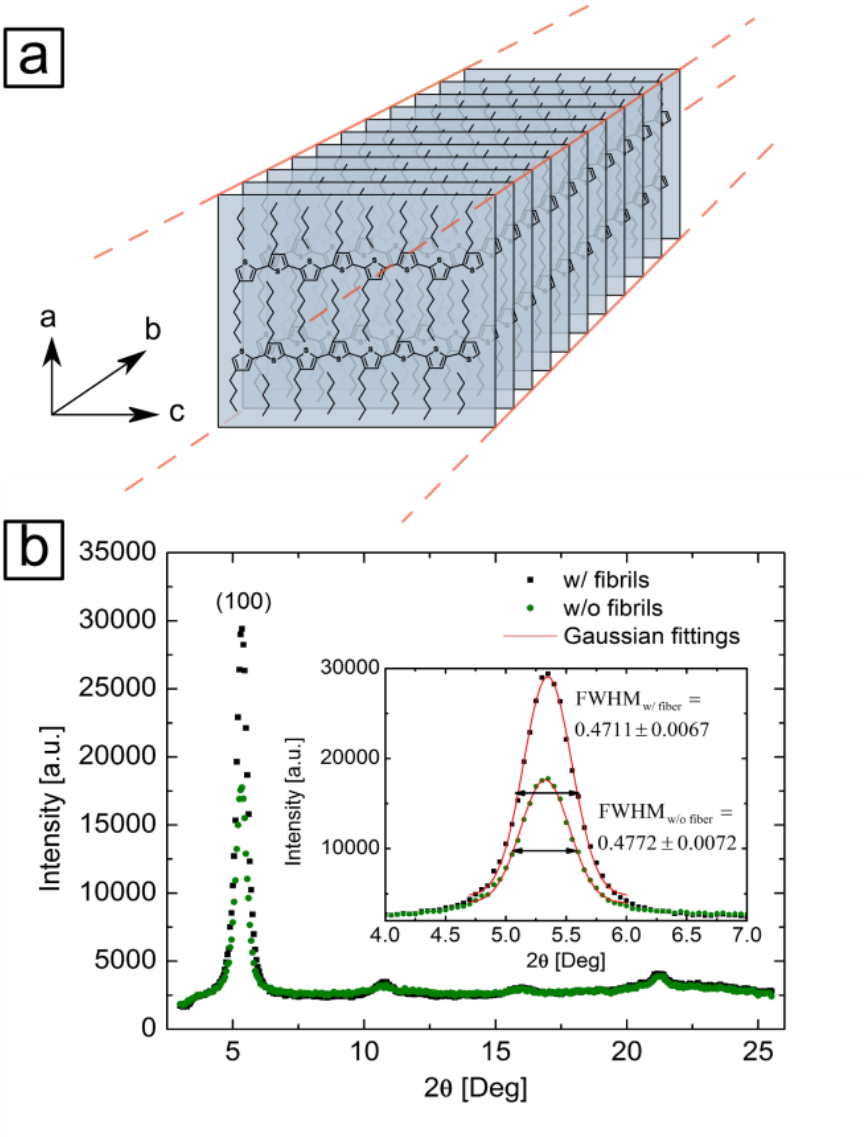

Figure 4.5 (a) Schematic diagram of the fibril structure, showing the π-π stacking along the longitudinal axis of the fibril. (b) The XRD spectrum of the ~700 nm P3HT films spincoated using the freshly-made solution and the one-month-old solution, respectively; the inset shows the zoomed-in (100) peaks of the two films, together with their Gaussian fitting and the full width half maximum (FWHM) values calculated.

The hole mobilities, measured using CELIV and IS, in the films with and without fibrils are different, reflecting differences between the morphologies of the films. A more

than 10% decrease of the out-of-plane mobility was measured in the samples containing fibrils (Figure 4.6a). These results seem to be contradictory to the ones reported in the literature [146-148], where higher hole mobilities were found for materials with fibrils; however, those measurements are either performed along the fibrils or across the bulk sample, indicating that it was the mobility along the fibrils that was measured. We show for the first time a decrease in hole mobility across the fibril, an opposite trend to what was found along the fibrils.

a

	Hole mobility [$cm^2/V.s$]	
	Freshly-made	1-month-old
ToF	8.4×10^{-4}	7.4×10^{-4}
Impedance	7.2×10^{-4}	6.4×10^{-4}

b

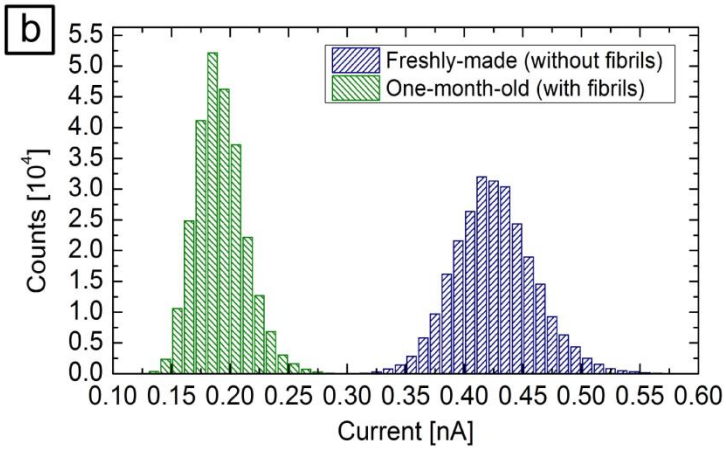

Figure 4.6 (a) The hole mobility results of the two films measured using both ToF and IS. (b) The histogram of the current intensity maps of the two films shown in Figure 4.4.

To further investigate the effect of the presence of fibrils on the conductivity of the films, conductive atomic force microscopy (CAFM) measurements were performed on our samples. CAFM has been proven to be a very powerful technique for a high-resolution

characterization of both the morphology and the local electric properties of the conductive films [149-151]. By applying a voltage bias (4.0 V in this case) between the AFM tip and the conductive substrate, dark current maps were collected for each film (shown in Figure 4.4b and d). It is clear from the dark current maps that a lower current intensity (darker area in the AFM image; see Figure 4.4b) along the center of the fibrils was observed. Furthermore, the histograms of the dark current (Figure 4.6b) indicate that the average current of the film containing fibrils is only half of that without fibrils.

The reason for the decrease in the mobility value may thus be discerned from the structures of the P3HT films. To begin with, the out-of-plane hole mobility of the "edge-on" orientation is slowest and, as mentioned earlier, 2 orders of magnitude lower than the "face-on" direction [16, 141-142]. The out-of-plane current intensity or mobility is an indication of the charges transported in the direction normal to the substrate and, hence, perpendicular to the fibrils [16, 141-142]. As a result, the charge carriers need to travel perpendicularly to the fibrils, with a lower mobility, and therefore overcome the energy barrier at the boundary between the fibrils and the surrounding domains; this process significantly decreases the measured mobility and leads to a lower current intensity. A quantitative and systematic study of the fibril formation mechanism and fibril-dependent electrical properties is under way and will be discussed in more details in future studies.

4.5 Conclusion

In this work we demonstrated how the out-of-plane carrier mobility, dc conductivity and carrier density in conjugated polymer thin films may be determined simultaneously with the use of impedance spectroscopy. We then showed how these charge transport properties are thickness-dependent and strongly dependent on the morphology of the film, controlled through processing. The carrier mobility increased with increasing film thickness and then reached a plateau, whereas the dc conductivity and the carrier density exhibited the opposite trend. The trends are associated with changes in the nanoscale morphology with film thickness [125, 152]. This behavior is in contrast to those in inorganic crystalline systems, which possess long-range structural order.

CHAPTER 5
CONCLUSION

There is no doubt that the secrets of the materials properties lie in their structures, and the establishment of the structure/property relationship is key to the understanding and improvement of the various materials and complex condensed matter systems. In terms of polymers in particular, it is especially crucial and important. On the one hand, new polymers have been synthesized and proven to have promising properties and there is therefore urgency to gain more knowledge on how they behave and interact in real applications, which often involving a rather complex system; on the other hand, fundamental scientific work, both experimental and theoretical, still needs to be done to understand basic, local interactions among monomers and how they are linked to macroscopic quantities.

In this dissertation, we have investigated several important complex systems, through which we discussed a variety of fundamental polymer physics problems. Understanding these problems may then provide means and ideas to further help with enhancing and tailoring specific properties in these complex systems.

In Chapter 2 the diblock copolymer and copolymer/homopolymer blend system is discussed. The influence of geometrical confinement on the segmental dynamics of the polyisoprene (PI) component of polystyrene-*b*-polyisoprene (PS-*b*-PI) diblock copolymers was investigated in mixtures of PS-*b*-PI copolymers, as the minor component, with PS homopolymers of varying degrees of polymerization P. When the degree of polymerization of the copolymers $N \ll P$, the copolymer chains self-organized into layered onion-like structures within the PS host. For lower values of P that are comparable to N, or smaller, the copolymers formed cylindrical micelles, with an inner core composed of PI and an outer corona of PS chains. Broadband dielectric spectroscopy (BDS) measurements reveal that at

temperatures approaching the local glass transition temperature (T_g) of PI in the mixtures, the relaxation times of the PI phase in the micelles $\tau_{micelle}$ were over an order of magnitude shorter than those in the layered onion-like mesostructures τ_{onion}. These segmental relaxation rates were compared with those of the PI homopolymer and of PI in pure copolymers possessing lamellar, τ_{lam}, and bicontinuous, gyroid, structures, τ_{gyroid}; they were found to be considerably faster. At temperatures close to the T_g of the PI component in each system, $\tau_{micelle}$ was over two orders of magnitude faster than τ_{lam}. The segmental relaxation times in the lamellar and the gyroid morphologies were comparable, $\tau_{lam} \sim \tau_{gyroid}$, but were systematically a factor of two slower than those of the pure PI homopolymer, $\tau_{homo} \sim 0.5\tau_{lam}$, throughout a wide temperature range. These trends in the magnitude of the relaxation rates are consistent with trends in the local T_g of the PI phase in each sample. We note that at high temperatures, the relaxation rates measured in all samples, regardless of morphology, were comparable. The differences between the segmental relaxation rates in these different systems may reflect different levels in the frustration of packing of chain segments at the interfaces of varying curvatures, in each system, engendered by the requirement to maintain a constant segmental density throughout.

In Chapter 3 the miscible polymer/polymer blend system is investigated. Polymer mixtures A/B in the single-phase regime of the phase diagram are compositionally heterogeneous due to the self-concentrations, ϕ_{self}, associated with monomer connectivity, of each component, as well to composition and density fluctuations. In this regard such a mixture is characterized by local regions, spatially and temporally, of composition varying from a lower value of ϕ_{self} to ϕ_{eff}, where ϕ_{eff} is due to ϕ_{self} and to the contributions associated with concentration and density fluctuations, i.e. $\phi_{eff} = \phi_{self}(T) + \phi_{fluc}(T, t)$. In this work we examined the component dynamics of poly(vinyl methyl ether) (PVME) chains in bulk and thin film blends of polystyrene (PS) and PVME, using broadband dielectric spectroscopy (BDS), and showed that the dominant relaxation processes are associated with PVME chains undergoing relaxations in two distinct compositional environments. At high temperatures the dynamics are Vogel-Fulcher-like, reflecting the fact that the chains experience the same average environment. However, with decreasing temperature there is evidence of a significantly stronger temperature dependent relaxation involving a population of PVME that "freezes." Additionally, there is evidence of another population of PVME, largely due to ϕ_{eff}, that undergoes relaxations, exhibiting an Arrhenius, temperature dependence within the

confines of glassy PS domains. In thin films of this blend, confined between aluminum (Al) surfaces, the PVME composition at the polymer/Al interfaces is higher than the bulk and the BDS measurements reveal the emergence of a new relaxation process associated with these chains. Our results, overall, confirm the notion that the dynamics of chains in A/B polymer blends manifest the influence of the local compositional environment.

In Chapter 4 conjugated polymer thin film is studied, and in contrast to the previous chapters, here we measured the conductive, rather than dielectric, properties of the films. We proposed an equivalent circuit fitting method to calculate the mobility of the conjugated polymer films of poly(3-hexylthiophene) (P3HT), using the technique of impedance spectroscopy (IS). Conjugated polymers have never been studied using IS, likely due to the challenge of decoupling the electrode polarization effect at low frequencies and the pronounced increase of ac conductivity at high frequencies, which invalidates the conventional means of analysis. Our method not only shows excellent agreement of the mobility with the ones measured with the widely used time-of-flight (ToF) (in thick films) and the technique of charge extraction in a linearly increasing voltage (CELIV) (in thick and thin films), but also provides dc conductivity σ_{dc} and charge carrier (hole) density n in P3HT thin films, which may not be achieved from ToF or CELIV. The IS data suggest that both σ_{dc} and n decrease significantly with increasing film thickness, in spite of the opposite thickness dependence in hole mobility. IS was then applied, together with CELIV, on P3HT films spincoated using aged solutions, in which P3HT fibrils were present. The mobility was measured to be lower in the films with fibrils than those without fibrils. This result agrees with the current intensity maps measured by conductive atomic force microscopy (CAFM), where the average current for the film with fibrils was observed to be only half of the one without fibrils.

Although the abovementioned systems are all somewhat different from each other, it is the structure/property relationship that brings them together. All systems show a clear sign that properties are significantly, and sometimes dramatically, linked to their structures. As has been discussed in Chapter 1, the importance of such a relationship is twofold. On the one hand, it serves as a guide showing us a way to improve the target properties, and why certain processing procedures enhance or compromise the device performance (e.g. the P3HT thin films, Chapter 4). On the other hand, for a system whose structure is difficult to determine using other means, measuring the properties may help estimate the structure (e.g.

the miscible polymer/polymer blends, Chapter 3). Moreover, understanding the structure/property relationship in certain complex systems may benefit other systems. For example, the tethered chains in Chapter 2 may be analogous to polymer brushes, therefore may provide more insights into understanding polymer brushes on non-planar surfaces.

Last but not the least, all these projects showed that the polymer chains and their interactions behave very differently on the nanoscale molecular level from what we are familiar with macroscopically, and as a result, their mesoscopic structures and properties are thus affected. I hope these results may contribute to understanding the local dynamics and their temperature dependence, which will continue to push forward the nanotechnologies and polymer science in general.

APPENDICES

A.1 Dielectric Spectrometer Guides

A.1.1 Sample loading guide

For bulk samples

1. Make sure the equipment is not running.
2. Disconnect all the wires from the head of the cryostat.
3. Clean everything using acetone and toluene: dielectric spectrometer cryostat, brass plates, tweezers, etc.
4. Calibrate the system if necessary (see the Calibration Guide).
5. Measure the thickness of the sample. If the sample is solid and its thickness cannot be measured directly (non-sheet-like), measure the two bare brass plates first using micrometer and measure again after sandwiching the sample between the brass plates. If the sample is liquid-like, "paste" the sample on one of the brass plate and put on two silica spacers (50-micron diameter), then put on the second brass plate. In a word, the thickness of the sample needs to be recorded.
6. Load the sandwiched sample in the laminar flow. Be very careful not to drop the cryostat. Rotate the top screw in the cryostat to lower (clockwise) or raise (counterclockwise) the top plate/electrode. DO NOT rotate the screw-like part right on top of the top plate/electrode. Load the sandwiched sample and center the sample. Try to tighten the top screw as much as possible.
7. Put the cryostat back in the equipment well and connect all the wires correctly (the large plug, three BNC cables (GEN, V1 and V2) as well as the small white cable for the thermocouple).

For thin film samples

1. Make sure the equipment is not running.
2. Disconnect all the wires from the head of the cryostat.
3. Clean everything using acetone and toluene: dielectric spectrometer cryostat, tweezers, the parts for thin film sample setup, razor blade, etc.
4. Calibrate the system if necessary (see the Calibration Guide).
5. Find the desired "cross" (spot #2 or #8) on the thin film sample.
6. Test the conduction of the top Al electrodes (3 stripes) using the multimeter and disconnect desired spot side from the rest, using a razor blade.
7. Unscrew to take out the plate, and mark the point where the top tip would touch when it is lowered, using a sharpie. Hold the sample onto the plate using the thin film setup pieces (you need to be gentle avoiding breaking the thin copper piece). Make sure the marked point is below the lower stripe, between the two "crosses." Tilt the plate towards all directions to ensure its tightness. Test the sample contact using the multimeter.
8. Reload the plate, together with the sample. Make sure the top tip is high enough so it does not accidentally scratch the film.
9. Carefully lower the tip by rotate the top screw clockwise. Stop when the tip is slightly above the film.
10. Hold the bottom "screw" (that is right above the tip and should NOT be rotated) with one hand to ensure its pointing position and lower the tip using the other hand, until the tip firmly touches the film, on top of the bottom Al electrode and the marked point. Tight the top screw as much as possible.
11. Test both contacts of the electrodes, as well as the isolation between the electrodes.
12. Put the cryostat back in the equipment well and connect all the wires correctly (the large plug, three BNC cables (GEN, V1 and V2) as well as the small white cable for the thermocouple).

A.1.2 Calibration guide

For bulk samples

1. Unload any samples in the cryostat. Clean the equipment using acetone and toluene.
2. Leave the circuit open (the top electrode not touching the bottom).
3. Turn on the WinDETA software, if it is not turned on.
4. Select *Analyzers* > *Options* (the first one) > *Configuration*…. In the dialog box, input Maximum of "1" seconds or "2" periods in the "Integration Time" section on the left.
5. Select *Analyzers* > *Options* (the first one) > *Calibrate All*. You are then asked to confirm if the circuit is open. This procedure takes about 25 min.
6. Put the brass plates that will be used (or the same type) in the cryostat. Lower the top electrode and contact the plates. In other words, make a short circuit with the bare brass plates sandwiched.
7. Select *Analyzers* > *Options* (the first one) > *Load Short Calibration*. You are then asked to create a short circuit before continuing. This procedure takes about 1~2 min.
8. After the Short Calibration is finished, a dialog box pops up asking to load the 100-ohm resistor. Replace the brass plates in the cryostat with the 100-ohm resistor, and click "OK." This procedure takes about 1~2 min.
9. After the above step is done, take out the 100-ohm resistor. The equipment is then ready to use.

For thin film samples

Same steps as the bulk sample from 1 to 5.

---

6. Switch the top electrode with the tip for thin film measurement. Lower the tip to make a contact with the bottom plate.
7. Start the Short Calibration same as the bulk sample.
8. After the Short Calibration is done and the dialog box pops up, switch the tip back to the original top flat electrode. Load the 100-ohm resistor, same as for the bulk sample, and start the 100-ohm Calibration.
9. After the above step is done, take out the 100-ohm resistor. Switch the top electrode with the tip. The equipment is then ready to use.

A.1.3 Quick start and test measurement guide

1. Start the WinDETA software, if it is not turned on.
2. Select *Temp. Controller* > *Initialize from WinDETA*. A little tick should show up before the words and the information should show up in the top-left "status" window.
3. In the "status" window, "P" means the current value and "S" is the set value. Make sure the P-value for Sample Temperature is around room temperature. If it shows "INF," the thermocouple wire is not connected. Connect it.
4. Take a look at the equipment tower. The "VACUUM" switch at the bottom should be at "1." The A4 LED light should be on, meaning the current nitrogen flow pressure (Dewar Pressure) is below 12 mbar.
5. The A5 LED light may be on or not, which indicates if the current temperature is above the Start Temperature (safety temperature upper limit) or not. If the software is not previously turned on, the Start Temperature is set to 0 degC, which is below the room temperature, then the A5 LED light should be on. Go to *Temp. Controller* > *Safety Limits*, change the Start Temperature to 300 degC. Check the A5 LED light again, it should be off now.
6. To do a test measurement, select *File* > *Set File Names*…, and then create a file name in the desired file folder. The file extension is ".eps." Notice that you are not able to tell that you have set a file name. If there was an old file written, the old file name would still be there, before you start the measurement.
7. Go to *Measurement* > *Sample Specification*… to input the info and initial data of the sample. In the dialog box, the top section is the sample description, followed by the sample diameter (mm) and the sample thickness (mm). Input the sample diameter and thickness.
8. The ac voltage needs to be selected too. Go to *Analyzers* > *Options* (the first one) > *Configuration*…, and input the desired voltage on the right-hand side. For bulk samples, 1.5 V is used. For thin film samples, the voltage needs to be calculated based on the case that the electric field in the film should be no greater than 100 kV/m.
9. Go to *Measurement* > *List Order*…. Make sure the order is "frequency" and then "time."
10. Go to *Measurement* > *Value Lists* > *Frequency*…. Click "Clear" on the right to clear the frequency list. Click "List" and "OK" to input a list. Delete the high frequency

numbers down to 4 MHz, as well as the last one: 0.1 Hz. Click "OK" to save and exit.

11. You may check all your settings by selecting *Measurement* > *Show Definitions*. A text file will be opened with all the info included.
12. After making sure that all the settings are fine, start the test run by selecting *Measurement* > *Start Single Sweep*. If the file name selected already exists, or the measurement is running a second time without setting a new file name, the software would ask if you would like to overwrite the previous data. The points are shown instantly in the bottom-right window called "online." The measurement is done automatically after all the frequency points are gone through.
13. You may also select *Measurement* > *Start* instead. In this case, the measurement keeps going through all the frequency points and repeats itself after every cycle. It never ends until the measurement is terminated by selecting *Measurement* > *Stop*, or until the liquid nitrogen in the dewar runs out.

A.1.4 Quick troubleshooting

Sometimes when you try to start a measurement, error message pops up (showing in red in the upper right "message" window) or error message dialog box shows up. In most cases these are due to some "trivial" mistakes. Check if any of the following happens:

1. The plug or the wires are not connected, or connected wrong.
2. The nitrogen tank is almost empty.
3. The Start Temperature is not set at above the current temperature.
4. The bottom plate in the cryostat touches the frame.

A.2 Algorithms and Tips for Dielectric Spectroscopy Data Analysis

A.2.1 2D plotting and fitting of the dielectric spectroscopy data of PVME/PS

As the BDS measurement captures dielectric data for temperatures with a fixed interval (usually 1 K), whereas the eventual figure, showing the temperature dependences of the relaxations, is plotted with its abscissa being the inverse temperature ($1000/T$ to be exact), the discrete matrix of the imaginary permittivity (ε'') for all frequencies and

temperatures measured is required to be fitted two-dimensionally. It is performed using the following algorithm (the actual coding is written in Mathematica):

---

1. Generate data list containing all the data points to be fitted, such as {temperature(i), frequency(i), ε''(i)}; this step may be done through nested loops.
2. Fit the data using 2D polynomial fitting, i.e. for x and y being temperature and log(frequency), respectively, $\varepsilon'' = \sum_{i,j=0}^{i,j=n-1} a_{ij} x^i y^j$. The polynomial order n is often chosen to be a relatively high number (e.g. 30) in order to fit the data properly. With a good fit, the choice of n should not matter. To have a better resolution of the weaker data at low temperatures and low frequencies, log(ε'') should be plotted instead of ε''. In Mathematica, this can be achieved using the **FindFit** function. Hereafter the fitted function is denoted as $g(x, y)$, with $x = T$ and $y = \log(\omega)$; here, ω is the angular frequency, i.e. $\omega = 2\pi f$.
3. With $g(x, y)$, permittivity results given any temperature and frequency within the measurement range can be generated. To convert the function to plot $1000/T$ rather than T, write $h(x, y) = g(1000/x, y)$. Imaginary permittivity matrix may then be generated using $h(x, y)$ at will.

Having had the 2D function fitted, the function $h(x, y)$ may then be visualized using a contour plot. The curvatures of the contours reflect the relaxations (peaks in 1D) in the measured frequency and temperature range. In such a case, the intrinsic frequency (i.e. the reciprocal of the relaxation time) can no longer be determined using the conventional method. At this time, although not ideal, the temperature dependence of the relaxation can be extracted by the following procedure.

---

1. Firstly, the two axes in the contour plot need to be normalized to become dimensionless. Assuming the ranges of the original axes are $[x_{min}, x_{max}]$ and $[y_{min}, y_{max}]$, the new ranges (x' and y') after the normalization are then $[0, L]$ for both axes: $x' = \frac{x - x_{min}}{x_{max} - x_{min}} L$ and $y' = \frac{y - y_{min}}{y_{max} - y_{min}} L$. Alternatively, the original axes may be kept, but we assume that the total ranges of the two axes (with different units), $x_{max} - x_{min}$ and $y_{max} - y_{min}$, respectively, share the same dimensionless length.

2. The temperature dependence of the relaxation is then found by calculating a series of points on the contour map, the collection of which forms the entire relaxation curve. The points are calculated one by one, with the latter based on the position of the former.
3. Pick a starting frequency ($\log(\omega)$ to be exact), say y_0, to be the point with highest frequency value. Then, find value x_0 so that $h(x, y_0)$ reaches maximum when $x = x_0$. (x_0, y_0) is the starting point. The subscript "0" can be considered as a step index n; at this moment $n = 0$.
4. Now we look for the next point (x_{n+1}, y_{n+1}), which should have greater x-value and smaller y-value than the previous point. The angle between vector $(x_{n+1}-x_n, y_{n+1}-y_n)$ and $1000/T$ axis is denoted as θ. We define a dimensionless step length, which equals $\ell_x = (x_{max} - x_{min})/1000$ on the $1000/T$ axis, and $\ell_y = (y_{max} - y_{min})/1000$ on the $\log(\omega)$ axis; in general, we have $x_{n+1} = x_n + \ell_x \cos\theta$, and $y_{n+1} = y_n - \ell_y \sin\theta$. Calculate $h(x_{n+1}, y_{n+1})$ for all the θ values between 0° and 90°, and the θ value resulting in the highest $h(x_{n+1}, y_{n+1})$ is the one for the next point.
5. Repeat Step 4, until $x_{max} - x_n < \ell_x$ or $y_n - y_{min} < \ell_y$. Then the assembly of all the points should represent the relaxation.
6. For scenarios with multiple relaxations, different starting points should be used to obtain the temperature dependence of different relaxations.

A.2.2 Tips for dielectric spectroscopy data analysis

The raw data, if suffering from strong measurement error, may be treated using one of the two ways. (1) Because the error is often very weakly dependent on temperature, the data, instead of conventionally plotted against the ac frequency applied, can be plotted against the sample temperature. It is very likely that the noisy spectra would disappear (e.g. Chapter 2). It does not apply to heterogeneous miscible blends (Chapter 3), as the two plots would provide very different results. (2) If at a certain temperature the spectrum of imaginary permittivity in the measured frequency window is not affected by any of the relaxations but only exhibit the background noise, this background is often subtracted from spectra at other temperatures to minimize the noise. However, such a treatment, although very useful in many occasions, may change the shape of the relaxation peak slightly; so one

should be more cautious, for instance, when trying to compare the widths of the relaxation peaks after such adjustments.

When it comes to a full measurement that spans a wide range of frequencies and temperatures, it is best to generate a matrix first before further analysis. 2D contour plot can then be plotted (Chapter 3 and Section A.2.1) which serves as a general picture. The best way to smoothen and/or fit the peaks in the data, either 1D or 2D, is to fit the data/matrix using a high-order polynomial.

A.3 List of Publications

[1] **H. Yang** and P.F. Green. Role of spatial compositional heterogeneity on component dynamics in miscible bulk and thin film polymer/polymer blends. *Macromolecules*, 2013, *46* (23), 9390-9395.

[2] **H. Yang**, X.C. Chen, G.R. Jun and P.F. Green. Segmental dynamics of chains tethered at interfaces of varying curvatures. *Macromolecules*, 2013, *46* (12), 5036-5043.

[3] **H. Yang**, E. Glynos, B. Huang and P.F. Green. Out-of-plane carrier transport in conjugated polymer thin films: role of morphology. *Journal of Physical Chemistry C*, 2013, *117* (19), 9590-9597.

[4] E.C. McIntyre, **H. Yang** and P.F. Green. The electrorheology of suspensions containing interfacially active constituents. *ACS Applied Materials and Interfaces*, 2013, *5* (18), 8925-8931.

[5] J. Kim, **H. Yang** and P.F. Green. Tailoring the refractive indices of thin film polymer metallic nanoparticle nanocomposites. *Langmuir*, 2012, *28* (25), 9735-9741.

[6] X.C. Chen, **H. Yang** and P.F. Green. Micellar formation and organization in thin film polymer blends. *Macromolecules*, 2012, *45* (9), 3993-4000.

[7] A. Querejeta-Fernández, J.C. Hernández-Garrido, **H. Yang**, Y. Zhou, A. Varela, M. Parras, J.J. Calvino-Gámez, J.M. González-Calbet, P.F. Green and N.A. Kotov. Unknown aspects of self-assembly of PbS microscale superstructures. *ACS Nano*, 2012, *6* (5), 3800-3812.

[8] E.C. McIntyre, **H. Yang** and P.F. Green. Electrorheology of polystyrene filler/polyhedral silsesquioxane suspensions. *ACS Applied Materials and Interfaces*, 2012, *4* (4), 2148-2153.

[9] X.C. Chen, **H. Yang** and P.F. Green. Tethered-polymer structures in thin film polymer melts. *Macromolecules*, 2011, *44* (14), 5758-5763.

[10] B. Huang, E. Glynos, B. Frieberg, **H. Yang** and P.F. Green. Effect of thickness-dependent microstructure on the out-of-plane hole mobility in poly(3-hexylthiophene) films. *ACS Applied Materials and Interfaces*, 2012, *4* (10), 5204-5210.

[11] A.J. Gross, G.-S. Hwang, B. Huang, **H. Yang**, N. Ghafouri, H. Kim, R.L. Peterson, C. Uher, M. Kaviany and K. Najafi. Multistage planar thermoelectric microcoolers. *Microelectromechanical Systems*, 2011, *20* (5), 1201-1210.

REFERENCES

(1) Mülhaupt, R., Hermann staudinger and the origin of macromolecular chemistry. *Angewandte Chemie International Edition.* **2004**, *43* (9), 1054-1063.

(2) Rubinstein, M.; Colby, R. H., *Polymer physics*. Oxford University Press: Oxford ; New York, 2003; p xi, 440 p.

(3) Donth, E.-J., *The glass transition : Relaxation dynamics in liquids and disordered materials*. Springer: Berlin ; New York, 2001; p xvii, 418 p.

(4) Bates, F. S.; Fredrickson, G. H., Block copolymers - designer soft materials. *Phys. Today.* **1999**, *52* (2), 32-38.

(5) Leibler, L.; Orland, H.; Wheeler, J. C., Theory of critical micelle concentration for solutions of block co-polymers. *J. Chem. Phys.* **1983**, *79* (7), 3550-3557.

(6) Leibler, L., Emulsifying effects of block copolymers in incompatible polymer blends. *Makromolekulare Chemie-Macromolecular Symposia.* **1988**, *16*, 1-17.

(7) Leibler, L., Block copolymers at interfaces. *Physica A.* **1991**, *172* (1-2), 258-268.

(8) Shull, K. R.; Winey, K. I.; Thomas, E. L.; Kramer, E. J., Segregation of block copolymer micelles to surfaces and interfaces. *Macromolecules.* **1991**, *24* (10), 2748-2751.

(9) Chen, X. C.; Yang, H. X.; Green, P. F., Tethered-polymer structures in thin film polymer melts. *Macromolecules.* **2011**, *44* (14), 5758-5763.

(10) Watanabe, H.; Urakawa, O., Component dynamics in miscible polymer blends: A review of recent findings. *Korea-Aust. Rheol. J.* **2009**, *21* (4), 235-244.

(11) Cendoya, I.; Alegria, A.; Alberdi, J. M.; Colmenero, J.; Grimm, H.; Richter, D.; Frick, B., Effect of blending on the pvme dynamics. A dielectric, nmr, and qens investigation. *Macromolecules.* **1999**, *32* (12), 4065-4078.

(12) Besancon, B. M.; Soles, C. L.; Green, P. F., Glass transition of miscible binary polymer-polymer thin films. *Phys. Rev. Lett.* **2006**, *97* (5), 057801.

(13) Chung, G. C.; Kornfield, J. A.; Smith, S. D., Compositional dependence of segmental dynamics in a miscible polymer blend. *Macromolecules.* **1994**, *27* (20), 5729-5741.

(14) Composto, R. J.; Kramer, E. J.; White, D. M., Mutual diffusion in the miscible polymer blend polystyrene poly(xylenyl ether). *Macromolecules.* **1988**, *21* (8), 2580-2588.

(15) Composto, R. J.; Kramer, E. J.; White, D. M., Reptation in polymer blends. *Polymer.* **1990**, *31* (12), 2320-2328.

(16) Sirringhaus, H.; Brown, P. J.; Friend, R. H.; Nielsen, M. M.; Bechgaard, K.; Langeveld-Voss, B. M. W.; Spiering, A. J. H.; Janssen, R. A. J.; Meijer, E. W.; Herwig, P.; de Leeuw, D. M., Two-dimensional charge transport in self-organized, high-mobility conjugated polymers. *Nature.* **1999**, *401* (6754), 685-688.

(17) Kremer, F.; Schonhals, A., *Broadband dielectric spectroscopy*. Springer-Verlag: Berlin Heidelberg, 2003.

(18) Barsoukov, E.; Macdonald, J. R., *Impedance spectroscopy: Theory, experiment, and applications, 2nd edition*. Wiley-Interscience: Oxford, 2005.

(19) Application notes can be found from Novocontrol Technologies website: http://www.novocontrol.de/html/info_app_notes.html, including "Dielectric spectroscopy on the dynamics of amorphous polymeric systems" by A. Schonhals, and "Phenomenological and molecular theories of dielectric and electrical relaxation of materials" by G. Williams and D.K. Thomas.

(20) Alexander, S., Adsorption of chain molecules with a polar head a-scaling description. *Journal de Physique.* **1977**, *38* (8), 983-987.

(21) de Gennes, P. G., Conformations of polymers attached to an interface. *Macromolecules.* **1980**, *13* (5), 1069-1075.

(22) Milner, S. T., Polymer brushes. *Science.* **1991**, *251* (4996), 905-914.

(23) Milner, S. T.; Witten, T. A.; Cates, M. E., A parabolic density profile for grafted polymers. *Europhys. Lett.* **1988**, *5* (5), 413-418.

(24) Semenov, A. N., Contribution to the theory of microphase layering in block-copolymer melts. *Zhurnal Eksperimentalnoi Teor. Fiz.* **1985**, *88* (4), 1242-1256.

(25) Koylu, D.; Carter, K. R., Stimuli-responsive surfaces utilizing cleavable polymer brush layers. *Macromolecules.* **2009**, *42* (22), 8655-8660.

(26) Lin, N. H.; Kim, M. M.; Lewis, G. T.; Cohen, Y., Polymer surface nano-structuring of reverse osmosis membranes for fouling resistance and improved flux performance. *J. Mater. Chem.* **2010**, *20* (22), 4642-4652.

(27) Daoud, M.; Cotton, J. P., Star shaped polymers - a model for the conformation and its concentration-dependence. *Journal de Physique.* **1982**, *43* (3), 531-538.

(28) Glynos, E.; Frieberg, B.; Oh, H.; Liu, M.; Gidley, D. W.; Green, P. F., Role of molecular architecture on the vitrification of polymer thin films. *Phys. Rev. Lett.* **2011**, *106* (12), 128301.

(29) Glynos, E.; Frieberg, B.; Green, P. F., Wetting of a multiarm star-shaped molecule. *Phys. Rev. Lett.* **2011**, *107* (11), 118303.

(30) Frieberg, B.; Glynos, E.; Sakellariou, G.; Green, P. F., Physical aging of star-shaped macromolecules. *ACS Macro Lett.* **2012**, *1* (5), 636-640.

(31) Frieberg, B.; Glynos, E.; Green, P. F., Structural relaxations of thin polymer films. *Phys. Rev. Lett.* **2012**, *108* (26), 268304.

(32) Ball, R. C.; Marko, J. F.; Milner, S. T.; Witten, T. A., Polymers grafted to a convex surface. *Macromolecules.* **1991**, *24* (3), 693-703.

(33) Giannelis, E. P.; Krishnamoorti, R.; Manias, E., Polymer-silicate nanocomposites: Model systems for confined polymers and polymer brushes. *Polymers in Confined Environments.* **1999**, *138*, 107-147.

(34) Pastorino, C.; Binder, K.; Kreer, T.; Muller, M., Static and dynamic properties of the interface between a polymer brush and a melt of identical chains. *J. Chem. Phys.* **2006**, *124* (6), 064902.

(35) Oh, H.; Green, P. F., Polymer chain dynamics and glass transition in athermal polymer/nanoparticle mixtures. *Nat. Mater.* **2009**, *8* (2), 139-143.

(36) Halperin, A., Polymeric micelles - a star model. *Macromolecules.* **1987**, *20* (11), 2943-2946.

(37) Viduna, D.; Limpouchova, Z.; Prochazka, K., Monte carlo simulation of polymer brushes in narrow pores. *J. Chem. Phys.* **2001**, *115* (15), 7309-7318.

(38) Binder, K.; Milchev, A., Polymer brushes on flat and curved surfaces: How computer simulations can help to test theories and to interpret experiments. *J. Polym. Sci. Pt. B-Polym. Phys.* **2012**, *50* (22), 1515-1555.

(39) Dimitrov, D. I.; Milchev, A.; Binder, K., Polymer brushes in cylindrical pores: Simulation versus scaling theory. *J. Chem. Phys.* **2006**, *125* (3), 034905.

(40) Dimitrov, D. I.; Milchev, A.; Binder, K.; Heermann, D. W., Structure of polymer brushes in cylindrical tubes: A molecular dynamics simulation. *Macromol. Theory Simul.* **2006**, *15* (7), 573-583.

(41) Koutsioubas, A. G.; Spiliopoulos, N.; Anastassopoulos, D. L.; Vradis, A. A.; Toprakcioglu, C., Formation of polymer brushes inside cylindrical pores: A computer simulation study. *J. Chem. Phys.* **2009**, *131* (4), 044901.

(42) Kruk, M.; Dufour, B.; Celer, E. B.; Kowalewski, T.; Jaroniec, M.; Matyjaszewski, K., Grafting monodisperse polymer chains from concave surfaces of ordered mesoporous silicas. *Macromolecules.* **2008**, *41* (22), 8584-8591.

(43) Petychakis, L.; Floudas, G.; Fleischer, G., Chain dynamics of polyisoprene confined in porous media. A dielectric spectroscopy study. *Europhys. Lett.* **1997**, *40* (6), 685-690.

(44) Prochazka, K., Monte-carlo study of tethered chains in spherical volumes. *J. Phys. Chem.* **1995**, *99* (38), 14108-14116.

(45) Cerda, J. J.; Sintes, T.; Toral, R., Spherical brushes within spherical cavities: A self-consistent field and monte carlo study. *J. Chem. Phys.* **2009**, *131* (13), 134901.

(46) Abetz, V.; Simon, P. F. W., Phase behaviour and morphologies of block copolymers. In *Block copolymers i*, Abetz, V., Ed. Springer-Verlag Berlin: Berlin, 2005; Vol. 189, pp 125-212.

(47) Bates, F. S.; Fredrickson, G. H., Block copolymer thermodynamics - theory and experiment. *Annu. Rev. Phys. Chem.* **1990**, *41*, 525-557.

(48) Lorthioir, C.; Alegria, A.; Colmenero, J.; Deloche, B., Heterogeneity of the segmental dynamics of poly(dimethylsiloxane) in a diblock lamellar mesophase: Dielectric relaxation investigations. *Macromolecules.* **2004**, *37* (20), 7808-7817.

(49) del Valle-Carrandi, L.; Alegria, A.; Colmenero, J., Pdms behaviour under confinement in strongly segregated mesophases of ps-pdms diblock copolymers. *Eur. Phys. J.-Spec. Top.* **2010**, *189* (1), 257-261.

(50) Adachi, K.; Kotaka, T., Influence of entanglement on the dielectric normal mode process of cis-polyisoprene. *Macromolecules.* **1984**, *17* (1), 120-122.

(51) Adachi, K.; Hirano, H., Slow dielectric relaxation of cis-polyisoprene near the glass transition temperature. *Macromolecules.* **1998**, *31* (12), 3958-3962.

(52) Boese, D.; Kremer, F., Molecular-dynamics in bulk cis-polyisoprene as studied by dielectric-spectroscopy. *Macromolecules.* **1990**, *23* (3), 829-835.

(53) Serghei, A.; Kremer, F., Confinement-induced relaxation process in thin films of cis-polyisoprene. *Phys. Rev. Lett.* **2003**, *91* (16), 165702.

(54) Santangelo, P. G.; Roland, C. M., Temperature dependence of mechanical and dielectric relaxation in cis-1,4-polyisoprene. *Macromolecules.* **1998**, *31* (11), 3715-3719.

(55) Roland, C. M.; Paluch, M.; Casalini, R., Effects of the volume and temperature on the global and segmental dynamics in poly(propylene glycol) and 1,4-polyisoprene. *J. Polym. Sci. Pt. B-Polym. Phys.* **2004**, *42* (23), 4313-4319.

(56) Fragiadakis, D.; Casalini, R.; Bogoslovov, R. B.; Robertson, C. G.; Roland, C. M., Dynamic heterogeneity and density scaling in 1,4-polyisoprene. *Macromolecules.* **2011**, *44* (5), 1149-1155.

(57) Watanabe, H., Viscoelasticity and dynamics of entangled polymers. *Prog. Polym. Sci.* **1999**, *24* (9), 1253-1403.

(58) Watanabe, H., Dielectric relaxation of type-a polymers in melts and solutions. *Macromol. Rapid Commun.* **2001**, *22* (3), 127-175.

(59) Alegria, A.; Colmenero, J.; Ngai, K. L.; Roland, C. M., Observation of the component dynamics in a miscible polymer blend by dielectric and mechanical spectroscopies. *Macromolecules.* **1994**, *27* (16), 4486-4492.

(60) Arbe, A.; Alegria, A.; Colmenero, J.; Hoffmann, S.; Willner, L.; Richter, D., Segmental dynamics in poly(vinylethylene)/polyisoprene miscible blends revisited. A neutron scattering and broad-band dielectric spectroscopy investigation. *Macromolecules.* **1999**, *32* (22), 7572-7581.

(61) Wang, J.; Roland, C. M., Heterogeneous networks of polyisoprene/polyvinylethylene. *Polymer.* **2005**, *46* (12), 4160-4165.

(62) Watanabe, H., Slow dielectric-relaxation of a styrene-isoprene-styrene triblock copolymer with dipole inversion in the middle block - a challenge to a loop-bridge problem. *Macromolecules.* **1995**, *28* (14), 5006-5011.

(63) Rizos, A. K.; Fytas, G.; Semenov, A. N., Concentration fluctuation effects on chain orientation dynamics of polymer blends in the critical region. *J. Chem. Phys.* **1995**, *102* (17), 6931-6940.

(64) Gotze, W.; Sjogren, L., Relaxation processes in supercooled liquids. *Rep. Prog. Phys.* **1992**, *55* (3), 241-376.

(65) Slimani, M. Z.; Moreno, A. J.; Colmenero, J., Heterogeneity of the segmental dynamics in lamellar phases of diblock copolymers. *Macromolecules.* **2011**, *44* (17), 6952-6961.

(66) Helfand, E.; Tagami, Y., Theory of interface between immiscible polymers .2. *J. Chem. Phys.* **1972**, *56* (7), 3592.

(67) Koizumi, S.; Hasegawa, H.; Hashimoto, T., Ordered structures of block copolymer/homopolymer mixtures .5. Interplay of macrophase and microphase transitions. *Macromolecules.* **1994**, *27* (22), 6532-6540.

(68) Chen, X. C.; Yang, H. X.; Green, P. F., Micellar formation and organization in thin film polymer blends. *Macromolecules.* **2012**, *45* (9), 3993-4000.

(69) Mayes, A. M.; Delacruz, M. O., Cylindrical versus spherical micelle formation in block copolymer homopolymer blends. *Macromolecules.* **1988**, *21* (8), 2543-2547.

(70) Fukao, K.; Miyamoto, Y., Slow dynamics near glass transitions in thin polymer films. *Phys. Rev. E.* **2001**, *64* (1), 011803.

(71) Baschnagel, J.; Varnik, F., Computer simulations of supercooled polymer melts in the bulk and in-confined geometry. *J. Phys.-Condes. Matter.* **2005**, *17* (32), R851-R953.

(72) Forrest, J. A.; DalnokiVeress, K.; Dutcher, J. R., Interface and chain confinement effects on the glass transition temperature of thin polymer films. *Phys. Rev. E.* **1997**, *56* (5), 5705-5716.

(73) Kalakkunnath, S.; Kalika, D. S.; Lin, H. Q.; Freeman, B. D., Segmental relaxation characteristics of cross-linked poly(ethylene oxide) copolymer networks. *Macromolecules.* **2005**, *38* (23), 9679-9687.

(74) Koh, Y. P.; Simon, S. L., Structural relaxation of stacked ultrathin polystyrene films. *J. Polym. Sci. Pt. B-Polym. Phys.* **2008**, *46* (24), 2741-2753.

(75) Choi, U. H.; Lee, M.; Wang, S. R.; Liu, W. J.; Winey, K. I.; Gibson, H. W.; Colby, R. H., Ionic conduction and dielectric response of poly(imidazolium acrylate) ionomers. *Macromolecules.* **2012**, *45* (9), 3974-3985.

(76) Agapov, A. L.; Sokolov, A. P., Decoupling ionic conductivity from structural relaxation: A way to solid polymer electrolytes? *Macromolecules.* **2011**, *44* (11), 4410-4414.

(77) Starr, F. W.; Douglas, J. F., Modifying fragility and collective motion in polymer melts with nanoparticles. *Phys. Rev. Lett.* **2011**, *106* (11), 115702.

(78) Riggleman, R. A.; Douglas, J. F.; de Pablo, J. J., Tuning polymer melt fragility with antiplasticizer additives. *J. Chem. Phys.* **2007**, *126* (23), 234903.

(79) Urakawa, O.; Fuse, Y.; Hori, H.; Tran-Cong, Q.; Yano, O., A dielectric study on the local dynamics of miscible polymer blends: Poly(2-chlorostyrene)/poly(vinyl methyl ether). *Polymer.* **2001**, *42* (2), 765-773.

(80) Priestley, R. D.; Rittigstein, P.; Broadbelt, L. J.; Fukao, K.; Torkelson, J. M., Evidence for the molecular-scale origin of the suppression of physical ageing in confined polymer: Fluorescence and dielectric spectroscopy studies of polymer-silica nanocomposites. *J. Phys.-Condes. Matter.* **2007**, *19* (20), 205120.

(81) Colmenero, J.; Arbe, A., Segmental dynamics in miscible polymer blends: Recent results and open questions. *Soft Matter.* **2007**, *3* (12), 1474-1485.

(82) Takeno, H.; Kobayashi, M.; Aikawa, T., Localized cooperative molecular motion in miscible polymer mixtures with large difference in glass-transition temperatures. *Macromolecules.* **2006**, *39* (6), 2183-2190.

(83) Green, P. F.; Adolf, D. B.; Gilliom, L. R., Dynamics of polystyrene poly(vinyl methyl-ether) blends. *Macromolecules.* **1991**, *24* (11), 3377-3382.

(84) Colby, R. H.; Lipson, J. E. G., Modeling the segmental relaxation time distribution of miscible polymer blends: Polyisoprene/poly(vinylethylene). *Macromolecules.* **2005**, *38* (11), 4919-4928.

(85) Wang, D.; Ishida, H., Surface micro-scale semi-heterogeneous structures in compatible polystyrene and poly(vinyl methyl ether) blend thin films investigated by lateral-force microscopy. *Macromol. Chem. Phys.* **2007**, *208* (19-20), 2222-2228.

(86) Dionisio, M.; Fernandes, A. C.; Mano, J. F.; Correia, N. T.; Sousa, R. C., Relaxation studies in peo/pmma blends. *Macromolecules.* **2000**, *33* (3), 1002-1011.

(87) Alvarez, F.; Alegria, A.; Colmenero, J., Study of the two-component segmental dynamics of poly(vinylethylene)/polyisoprene miscible blends. *Macromolecules.* **1997**, *30* (3), 597-604.

(88) Hoffmann, S.; Willner, L.; Richter, D.; Arbe, A.; Colmenero, J.; Farago, B., Origin of dynamic heterogeneities in miscible polymer blends: A quasielastic neutron scattering study. *Phys. Rev. Lett.* **2000**, *85* (4), 772-775.

(89) Kumar, S. K.; Colby, R. H.; Anastasiadis, S. H.; Fytas, G., Concentration fluctuation induced dynamic heterogeneities in polymer blends. *J. Chem. Phys.* **1996**, *105* (9), 3777-3788.

(90) Lodge, T. P.; McLeish, T. C. B., Self-concentrations and effective glass transition temperatures in polymer blends. *Macromolecules.* **2000**, *33* (14), 5278-5284.

(91) He, Y. Y.; Lutz, T. R.; Ediger, M. D., Segmental and terminal dynamics in miscible polymer mixtures: Tests of the lodge-mcleish model. *J. Chem. Phys.* **2003**, *119* (18), 9956-9965.

(92) Kim, E.; Kramer, E. J.; Osby, J. O., Tracer diffusion in the blends of polystyrene and tetramethylbisphenol-a polycarbonate. *Macromolecules.* **1995**, *28* (6), 1979-1989.

(93) Doi, M.; Edwards, S. F., *The theory of polymer dynamics*. Oxford University Press: Oxford, U.K., 1986.

(94) Schwartz, G. A.; Colmenero, J.; Alegria, A., Single component dynamics in miscible poly(vinyl methyl ether)/polystyrene blends under hydrostatic pressure. *Macromolecules.* **2007**, *40* (9), 3246-3255.

(95) Kremer, F.; Huwe, A.; Arndt, M.; Behrens, P.; Schwieger, W., How many molecules form a liquid? *J. Phys.-Condes. Matter.* **1999**, *11* (10A), A175-A188.

(96) Frieberg, B.; Kim, J.; Narayanan, S.; Green, P. F., Surface layer dynamics in miscible polymer blends. *ACS Macro Lett.* **2013**, *2* (5), 388-392.

(97) Ubrich, J. M.; Larbi, F. B.; Halary, J. L.; Monnerie, L.; Bauer, B. J.; Han, C. C., Molecular-weight effects on the phase-diagram of polystyrene polyvinyl methyl-ether) blends. *Macromolecules.* **1986**, *19* (3), 810-815.

(98) Nishi, T.; Kwei, T. K., Cloud point curves for polyvinyl methyl-ether) and monodisperse polystyrene mixtures. *Polymer.* **1975**, *16* (4), 285-290.

(99) Serghei, A.; Kremer, F., Unexpected preparative effects on the properties of thin polymer films. *Prog Coll Pol Sci S.* **2006**, *132*, 33-40.

(100) Brandrup, J.; Immergut, E. H., *Polymer handbook*. 3rd ed.; Wiley: New York, 1989.

(101) Bhatia, Q. S.; Pan, D. H.; Koberstein, J. T., Preferential surface-adsorption in miscible blends of polystyrene and polyvinyl methyl-ether). *Macromolecules*. **1988**, *21* (7), 2166-2175.

(102) Thomas, K. R.; Clarke, N.; Poetes, R.; Morariu, M.; Steiner, U., Wetting induced instabilities in miscible polymer blends. *Soft Matter*. **2010**, *6* (15), 3517-3523.

(103) Facchetti, A.; Yoon, M. H.; Marks, T. J., Gate dielectrics for organic field-effect transistors: New opportunities for organic electronics. *Adv. Mater.* **2005**, *17* (14), 1705-1725.

(104) Forrest, S. R., The path to ubiquitous and low-cost organic electronic appliances on plastic. *Nature*. **2004**, *428* (6986), 911-918.

(105) Chang, J. F.; Sun, B. Q.; Breiby, D. W.; Nielsen, M. M.; Solling, T. I.; Giles, M.; McCulloch, I.; Sirringhaus, H., Enhanced mobility of poly(3-hexylthiophene) transistors by spin-coating from high-boiling-point solvents. *Chem. Mat.* **2004**, *16* (23), 4772-4776.

(106) Kim, Y.; Cook, S.; Tuladhar, S. M.; Choulis, S. A.; Nelson, J.; Durrant, J. R.; Bradley, D. D. C.; Giles, M.; McCulloch, I.; Ha, C. S.; Ree, M., A strong regioregularity effect in self-organizing conjugated polymer films and high-efficiency polythiophene: Fullerene solar cells. *Nat. Mater.* **2006**, *5* (3), 197-203.

(107) Mihailetchi, V. D.; Xie, H. X.; de Boer, B.; Koster, L. J. A.; Blom, P. W. M., Charge transport and photocurrent generation in poly (3-hexylthiophene): Methanofullerene bulk-heterojunction solar cells. *Adv. Funct. Mater.* **2006**, *16* (5), 699-708.

(108) Salleo, A.; Kline, R. J.; DeLongchamp, D. M.; Chabinyc, M. L., Microstructural characterization and charge transport in thin films of conjugated polymers. *Adv. Mater.* **2010**, *22* (34), 3812-3838.

(109) Blom, P. W. M.; deJong, M. J. M.; vanMunster, M. G., Electric-field and temperature dependence of the hole mobility in poly(p-phenylene vinylene). *Phys. Rev. B.* **1997**, *55* (2), R656-R659.

(110) Huang, J. S.; Li, G.; Yang, Y., Influence of composition and heat-treatment on the charge transport properties of poly(3-hexylthiophene) and 6,6 -phenyl c-61-butyric acid methyl ester blends. *Appl. Phys. Lett.* **2005**, *87* (11), 112105.

(111) Redecker, M.; Bradley, D. D. C.; Inbasekaran, M.; Woo, E. P., Nondispersive hole transport in an electroluminescent polyfluorene. *Appl. Phys. Lett.* **1998**, *73* (11), 1565-1567.

(112) Chiguvare, Z.; Dyakonov, V., Trap-limited hole mobility in semiconducting poly(3-hexylthiophene). *Phys. Rev. B.* **2004**, *70* (23), 235207.

(113) Chirvase, D.; Chiguvare, Z.; Knipper, M.; Parisi, J.; Dyakonov, V.; Hummelen, J. C., Temperature dependent characteristics of poly(3 hexylthiophene)-fullerene based heterojunction organic solar cells. *J. Appl. Phys.* **2003**, *93* (6), 3376-3383.

(114) Rose, A., Space-charge-limited currents in solids. *Physical Review.* **1955**, *97* (6), 1538-1544.

(115) Tanase, C.; Meijer, E. J.; Blom, P. W. M.; de Leeuw, D. M., Unification of the hole transport in polymeric field-effect transistors and light-emitting diodes. *Phys. Rev. Lett.* **2003**, *91* (21), 216601.

(116) Juska, G.; Arlauskas, K.; Viliunas, M.; Genevicius, K.; Osterbacka, R.; Stubb, H., Charge transport in pi-conjugated polymers from extraction current transients. *Phys. Rev. B.* **2000**, *62* (24), R16235-R16238.

(117) Juska, G.; Arlauskas, K.; Viliunas, M.; Kocka, J., Extraction current transients: New method of study of charge transport in microcrystalline silicon. *Phys. Rev. Lett.* **2000**, *84* (21), 4946-4949.

(118) Kumar, A.; Liao, H. H.; Yang, Y., Hole mobility in optimized organic photovoltaic blend films obtained using extraction current transients. *Org. Electron.* **2009**, *10* (8), 1615-1620.

(119) Sandberg, H. G. O.; Frey, G. L.; Shkunov, M. N.; Sirringhaus, H.; Friend, R. H.; Nielsen, M. M.; Kumpf, C., Ultrathin regioregular poly(3-hexyl thiophene) field-effect transistors. *Langmuir.* **2002**, *18* (26), 10176-10182.

(120) Gburek, B.; Wagner, V., Influence of the semiconductor thickness on the charge carrier mobility in p3ht organic field-effect transistors in top-gate architecture on flexible substrates. *Org. Electron.* **2010**, *11* (5), 814-819.

(121) Resendiz, L.; Estrada, M.; Cerdeira, A.; Iniguez, B.; Deen, M. J., Effect of active layer thickness on the electrical characteristics of polymer thin film transistors. *Org. Electron.* **2010**, *11* (12), 1920-1927.

(122) Klein, R. J.; Zhang, S. H.; Dou, S.; Jones, B. H.; Colby, R. H.; Runt, J., Modeling electrode polarization in dielectric spectroscopy: Ion mobility and mobile ion concentration of single-ion polymer electrolytes. *J. Chem. Phys.* **2006**, *124* (14), 144903.

(123) Sangoro, J. R.; Serghei, A.; Naumov, S.; Galvosas, P.; Karger, J.; Wespe, C.; Bordusa, F.; Kremer, F., Charge transport and mass transport in imidazolium-based ionic liquids. *Phys. Rev. E.* **2008**, *77* (5), 051202.

(124) Serghei, A.; Tress, M.; Sangoro, J. R.; Kremer, F., Electrode polarization and charge transport at solid interfaces. *Phys. Rev. B.* **2009**, *80* (18), 184301.

(125) Huang, B. Y.; Glynos, E.; Frieberg, B.; Yang, H. X.; Green, P. F., Effect of thickness-dependent microstructure on the out-of-plane hole mobility in poly(3-hexylthiophene) films. *ACS Appl. Mater. Interfaces.* **2012**, *4* (10), 5204-5210.

(126) Jonscher, A. K., Dielectric relaxation in solids. *J. Phys. D-Appl. Phys.* **1999**, *32* (14), R57-R70.

(127) Dyre, J. C., The random free-energy barrier model for ac conduction in disordered solids. *J. Appl. Phys.* **1988**, *64* (5), 2456-2468.

(128) Dyre, J. C.; Schroder, T. B., Universality of ac conduction in disordered solids. *Rev. Mod. Phys.* **2000**, *72* (3), 873-892.

(129) Klein, R. J.; Runt, J., Plasticized single-ion polymer conductors: Conductivity, local and segmental dynamics, and interaction parameters. *J. Phys. Chem. B.* **2007**, *111* (46), 13188-13193.

(130) Roling, B.; Martiny, C.; Murugavel, S., Ionic conduction in glass: New information on the interrelation between the "jonscher behavior" and the "nearly constant-loss behavior" from broadband conductivity spectra. *Phys. Rev. Lett.* **2001**, *87* (8), 085901.

(131) Mozer, A. J.; Sariciftci, N. S.; Pivrikas, A.; Osterbacka, R.; Juska, G.; Brassat, L.; Bassler, H., Charge carrier mobility in regioregular poly(3-hexylthiophene) probed by transient conductivity techniques: A comparative study. *Phys. Rev. B.* **2005**, *71* (3), 035214.

(132) Bisquert, J.; Garcia-Belmonte, G.; Bueno, P.; Longo, E.; Bulhoes, L. O. S., Impedance of constant phase element (cpe)-blocked diffusion in film electrodes. *J. Electroanal. Chem.* **1998**, *452* (2), 229-234.

(133) Conings, B.; Baeten, L.; Boyen, H. G.; Spoltore, D.; D'Haen, J.; Grieten, L.; Wagner, P.; Van Bael, M. K.; Manca, J. V., Influence of interface morphology onto the photovoltaic properties of nanopatterned zno/poly(3-hexylthiophene) hybrid solar cells. An impedance spectroscopy study. *J. Phys. Chem. C.* **2011**, *115* (33), 16695-16700.

(134) Kang, C. M.; Kim, S.; Hong, Y.; Lee, C., Frequency analysis on poly(3-hexylthiopene) rectifier using impedance spectroscopy. *Thin Solid Films.* **2009**, *518* (2), 889-892.

(135) LEVM and its manual is available online for download on J. Ross Macdonald's website at http://www.jrossmacdonald.com/levminfo.html.

(136) Macdonald, J. R.; Potter, L. D., A flexible procedure for analyzing impedance spectroscopy results - description and illustrations. *Solid State Ion.* **1987**, *24* (1), 61-79.

(137) Pitarch, A.; Bisquert, J.; Garcia-Belmonte, G., Mobile cation concentration in ionically conducting glasses calculated by means of mott-schottky capacitance-voltage characteristics. *J. Non-Cryst. Solids.* **2003**, *324* (1-2), 196-200.

(138) Schutt, H. J.; Gerdes, E., Space-charge relaxation in ionicly conducting oxide glasses .1. Model and frequency-response. *J. Non-Cryst. Solids.* **1992**, *144* (1), 1-13.

(139) Schutt, H. J.; Gerdes, E., Space-charge relaxation in ionicly conducting glasses .2. Free carrier concentration and mobility. *J. Non-Cryst. Solids.* **1992**, *144* (1), 14-20.

(140) Kim, J. S.; Park, Y.; Lee, D. Y.; Lee, J. H.; Park, J. H.; Kim, J. K.; Cho, K., Poly(3-hexylthiophene) nanorods with aligned chain orientation for organic photovoltaics. *Adv. Funct. Mater.* **2010**, *20* (4), 540-545.

(141) Shimomura, T.; Takahashi, T.; Ichimura, Y.; Nakagawa, S.; Noguchi, K.; Heike, S.; Hashizume, T., Relationship between structural coherence and intrinsic carrier transport in an isolated poly(3-hexylthiophene) nanofiber. *Phys. Rev. B.* **2011**, *83* (11), 115314.

(142) Ihn, K. J.; Moulton, J.; Smith, P., Whiskers of poly(3-alkylthiophene)s. *J. Polym. Sci. Pt. B-Polym. Phys.* **1993**, *31* (6), 735-742.

(143) Abdou, M. S. A.; Orfino, F. P.; Son, Y.; Holdcroft, S., Interaction of oxygen with conjugated polymers: Charge transfer complex formation with poly(3-alkylthiophenes). *J. Am. Chem. Soc.* **1997**, *119* (19), 4518-4524.

(144) Choulis, S. A.; Kim, Y.; Nelson, J.; Bradley, D. D. C.; Giles, M.; Shkunov, M.; McCulloch, I., High ambipolar and balanced carrier mobility in regioregular poly(3-hexylthiophene). *Appl. Phys. Lett.* **2004**, *85* (17), 3890-3892.

(145) Jimison, L. H.; Toney, M. F.; McCulloch, I.; Heeney, M.; Salleo, A., Charge-transport anisotropy due to grain boundaries in directionally crystallized thin films of regioregular poly(3-hexylthiophene). *Adv. Mater.* **2009**, *21* (16), 1568-1572.

(146) Merlo, J. A.; Frisbie, C. D., Field effect conductance of conducting polymer nanofibers. *J. Polym. Sci. Pt. B-Polym. Phys.* **2003**, *41* (21), 2674-2680.

(147) Newbloom, G. M.; Kim, F. S.; Jenekhe, S. A.; Pozzo, D. C., Mesoscale morphology and charge transport in colloidal networks of poly(3-hexylthiophene). *Macromolecules.* **2011**, *44* (10), 3801-3809.

(148) Newbloom, G. M.; Weigandt, K. M.; Pozzo, D. C., Electrical, mechanical, and structural characterization of self-assembly in poly(3-hexylthiophene) organogel networks. *Macromolecules.* **2012**, *45* (8), 3452-3462.

(149) Coffey, D. C.; Reid, O. G.; Rodovsky, D. B.; Bartholomew, G. P.; Ginger, D. S., Mapping local photocurrents in polymer/fullerene solar cells with photoconductive atomic force microscopy. *Nano Lett.* **2007**, *7* (3), 738-744.

(150) Dante, M.; Peet, J.; Nguyen, T. Q., Nanoscale charge transport and internal structure of bulk heterojunction conjugated polymer/fullerene solar cells by scanning probe microscopy. *J. Phys. Chem. C.* **2008**, *112* (18), 7241-7249.

(151) Reid, O. G.; Munechika, K.; Ginger, D. S., Space charge limited current measurements on conjugated polymer films using conductive atomic force microscopy. *Nano Lett.* **2008**, *8* (6), 1602-1609.

(152) Duong, D. T.; Toney, M. F.; Salleo, A., Role of confinement and aggregation in charge transport in semicrystalline polythiophene thin films. *Phys. Rev. B.* **2012**, *86* (20), 205205.